Sauts quantiques de phase dans des chaînes de jonctions Josephson
Ioan Mihai Pop

▶ **To cite this version:**

Ioan Mihai Pop. Sauts quantiques de phase dans des chaînes de jonctions Josephson. Autre [cond-mat.other]. Université de Grenoble, 2011. Français. NNT : 2011GRENY014 . tel-00586075

HAL Id: tel-00586075
https://theses.hal.science/tel-00586075

Submitted on 14 Apr 2011

UNIVERSITÉ DE GRENOBLE

THÈSE

Pour obtenir le grade de

DOCTEUR DE L'UNIVERSITÉ DE GRENOBLE

Spécialité : **Physique/Nanophysique**

Arrêté ministériel : 7 août 2006

Présentée par

Ioan Mihai POP

Thèse dirigée par **Wiebke GUICHARD** et
codirigée par **Bernard PANNETIER**

préparée au sein du **Laboratoire CNRS / Institut Néel**
dans **l'École Doctorale de Physique**

Sauts quantiques de phase dans des réseaux de jonctions Josephson

Thèse soutenue publiquement le **14 Février 2011**,
devant le jury composé de :

Prof. David HAVILAND
KTH Stockholm, Rapporteur
Prof. Alexey USTINOV
KIT Karlsruhe, Rapporteur
Prof. Joël CHEVRIER
UJF/CNRS Grenoble, Président
Prof. Yuli NAZAROV
TU Delft, Membre
Dr. Bernard PANNETIER
CNRS Grenoble, Membre
Prof. Wiebke GUICHARD
UJF/CNRS Grenoble, Membre
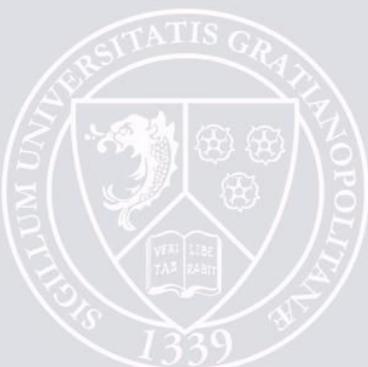
Acknowledgments

During the 4 years at Institut Néel, I have received important and often crucial help from many different people. In the following I would like to thank them. I also hope that in the future I will have the chance to return some of their favors.

Surely I am a lucky guy: I had the opportunity to work and learn in an experimental group led by three extraordinary researchers and outstanding personalities: Wiebke Guichard, Bernard Pannetier and Olivier Buisson. They succeeded in implementing the true meaning of the word "encadrement". They gently steered me in the right direction and, in the same time, they gave me a lot of freedom to explore around. I would like to especially thank Wiebke, who was always by my side, actively pushing the research forward. Incredibly, she managed to keep her focus and determination at the laboratory, even during some very difficult periods of her life. She has earned my deepest and most sincere admiration.

I want to thank the three reviewers of my manuscript: Michel Devoret, David Haviland and Alexey Ustinov, for their extensive analysis of the text and for their useful suggestions. I want to thank the president of the jury, Jöel Chevrier, who was also an excellent teacher during my Master 2, always outlining the spectacular side of physics equations. I thank Yuli Nazarov for his active participation in the jury.

In my search for the correct understanding of phase-slips, I benefited from fruitful discussions with many theoreticians. Closest to our experimental room, I would like to thank Frank Hekking and the people in his group, Gianluca Rastelli and Christoph Schenke, for the regular seminars and discussions, which I found essential for my PhD education and for the interpretation of the measured data. I benefited every year from the visits of Ivan Protopopov. He was a patient teacher during the first year of my PhD and a brilliant collaborator all along. Our group was also enriched from the regular visits of Benoit Douçot and Lev Ioffe. I would like to thank them for their interest in our research and their help with the numerical calculations.

I gratefully acknowledge the work of my predecessors, PhD students and post-docs, in the laboratory. When I arrived, I found an excellent working experimental setup, almost completely automated, which allowed me to focus more on the physics and less on the instrumentation. I thank the members of the *Quantum Coherence* team, whom I met every week during the team seminar. They provided a stimulating environment and a perfect trial public for my scientific presentations. I would like to mention the special cheerful atmosphere in the *Josephson junctions*

group and thank my colleagues: Florent, Iulian and Thomas for their professionalism.

I express my gratitude to the essential services of Institut Néel, which can make a researcher's life much easier: nanofab, electronics, cryogénie, liquéfacteur and administration.

Multumiri speciale for Olivier Isnard, who accompanied me during all my Grenoble years.

A warm thank you goes to the young community of PhD students and post-docs with which I shared intriguing physics (and not only) conversations and many great outdoor moments. Coffee time at the 2nd floor of bâtiment E will remain a landmark of my thesis years. I think I can only underestimate the real impact of all the cafeteria conversations I have had over the years. I would also raise a glass of *ţuică* for *the Romanian experience group* who made the trip to the wild part of Europe: Laetitia, Danny, David, Germain, Thomas and Loren. Thank you Oana for being the ideal colleague and friend all these university years. Thanks Sukumar for altruistically sharing the experimental room with me for a while and for all the joy you brought to the lab.

A special thank you to Mihai Miron for his AFM support and for being an entertaining companion during the long night hours spent in the clean-room. The Romanian community of students in Grenoble helped me a lot, especially during my Master year. I would like to acknowledge their precious advices and tips for a better understanding of the French system.

I thank my parents for investing their most precious resources in my education and for always providing the support and the advice I needed.

My most tender thank you goes to my muse, Cristina, who patiently supported and encouraged me all these years in Cluj and Grenoble. She is the best! As I was saying in the introduction, I am a lucky guy.

Summary

In this thesis we present detailed measurements of quantum phase-slips in Josephson junction chains. The probability amplitude of the phase-slips is controlled by the ratio between the Josephson energy, E_J, and the charging energy of each junction, E_C. We have measured complex superconducting networks containing tens of Josephson junctions.

The central result of this thesis is the measurement of the effect of quantum phase-slips on the ground state of Josephson junction networks (Pop et al., PRB 2008 and Nature Physics 2010). We have also observed the quantum interference of phase slips, the Aharonov-Casher effect, which is the electromagnetic dual of the well known Aharonov-Bohm effect. Our experimental results can be fitted in very good agreement by considering a simple tight-binding model for quantum phase-slips (Matveev et al. PRL 2002). We have shown that under phase-bias, a chain of Josephson junctions can behave in a collective way, very similar to a single macroscopic quantum object. These results open the way for possible use of quantum phase-slips for the design of novel Josephson junction circuits, such as topologically protected qubits or frequency-to-current conversion devices.

Résumé

Nous avons étudié la dynamique des sauts quantiques de phase (quantum phase-slips) dans différents types de réseaux de jonctions Josephson. Les sauts de phase sont contrôlés par le rapport entre l'énergie Josephson, E_J, et l'énergie de charge de chaque jonction, E_C. Nous avons étudié des réseaux qui contiennent jusqu'à quelques dizaines de jonctions.

Le résultat central de la thèse est la mesure de l'effet des sauts de phase sur l'état fondamental des réseaux de jonctions (POP et al., PRB 2008 et Nature Physics 2010). Nous avons aussi observé l'interférence quantique de sauts de phase, l'effet Aharonov-Casher, qui est le dual électromagnétique de l'effet Aharonov-Bohm. Les résultats de nos mesures sont en très bon accord avec les prédictions théoriques de Matveev et al. (PRL 2002). Nous avons montré qu'une chaîne de jonctions Josephson polarisée en phase, présente un comportement collectif, similaire à un objet quantique macroscopique. Les résultats de cette thèse ouvrent la voie pour la conception de nouveaux circuits Josephson, comme par exemple un qubit topologiquement protégé ou un dispositif quantique pour la conversion fréquence-courant.

Contents

List of Abbreviations

AC	alternating current
AFM	atomic force microscopy
DC	direct current
HF	high frequency (GHz)
IPA	Isopropanol
IV	current-voltage
JJ	Josephson junction
MIBK	Methylisobutylketone
MLG	Matveev-Larkin-Glazman (theoretical model)
MQT	macroscopic quantum tunneling
NMP	N-Methyl-2-pyrrolidone
PC	personal computer
PMMA	Polymethyl Methacrylate
QPS	quantum phase-slip
RCSJ	resistively and capacitively shunted junction
RIE	reactive ion etching
SEM	scanning electron microscope
SQUID	superconducting quantum interference device
TA	thermal activated
UHV	ultra high vacuum
UPD	underdamped phase diffusion
FFT	fast Fourier transform

Chapter 1

Introduction

Gordon Moore predicted in 1965 that the number of transistors on a chip will double every two years [1]. Originally intended as a rule of thumb, that prediction has become a principle for the industry in delivering ever-more-powerful semiconductor chips. In 2011 it is expected that transistors with a gate width of only 22 nm will be part of commercial products. For comparison, the inter-atomic distance in Aluminum is 0.4 nm, so the gate is a few tens of atoms wide. The rapid evolution of the microelectronics industry toward faster and smaller processing units and memories has pushed the physics of these devices close to the quantum regime. The resulting structures are in the middle (in Greek: *meso*) between the quantum universe of atoms and the classical macroscopic world. The physics at *mesoscopic* scale takes into account the laws of quantum mechanics, but it still uses semiclassical models.

From the race to build smaller and smaller objects, sophisticated techniques emerged that enable the fabrication of novel devices with size of the order of a few hundred nanometers. In Fig. 1 we show an electron microscope image of a *mesoscopic* electrical circuit based on $Al/AlO_x/Al$ junctions (the square shaped objects in the figure). In order to observe quantum behavior, we have to cool down these circuits to very low temperatures. At the

Fig. 1: electron microscope image of submicrometer aluminum structures

100 nm

typical working temperature $T \simeq 50\,\mathrm{mK}$, the circuit is superconducting.

Superconductivity, the property of some materials to have zero electrical resistance at sufficiently low temperature, was first observed by Heike Kamerlingh Onnes in 1911 [2]. The zero electrical resistance is a consequence of the fact that inside a superconductor, the conduction electrons are all locked in the same state, described by the same wave function. This more general phenomenon of particles "rushing" to behave identically is a quantum effect, called Bose-Einstein condensation [3] and it only occurs for certain types of particles, called bosons. Electrons are fermions, but under certain conditions, at low temperatures, two electrons can join to form a bound state called a Cooper pair [4]. The two spins 1/2 of the electrons

1

inside the Cooper pair align in a singlet state of total spin zero. At sufficiently low temperatures, Cooper pairs condensate to form the superconducting state [5].

Since the prediction of the Josephson effect, in 1962 [6], the field of superconducting electronics advanced very rapidly. In 1964 the first superconducting quantum interference device (SQUID) was measured [7,8]. SQUIDs are widely used now in applications such as: highly sensitive magnetometers, low noise and large bandwidth amplifiers or detectors for transition-edge bolometers [9].

The development of superconducting electronics provided the means for experiments testing the foundations of quantum mechanics at the mesoscopic scale. Among these experiments, the measurement of macroscopic quantum tunneling [10], the preparation of a quantum superposition state of electrical currents [11] or mechanical modes of a resonator [12], the measurement of Bell inequalities [13] or the entanglement of quantum states between different superconducting devices [14–18], represent remarkable confirmations of the quantum theory at the scale of large ensembles of atoms and molecules.

"Quantum Tunneling" © Charles Addams
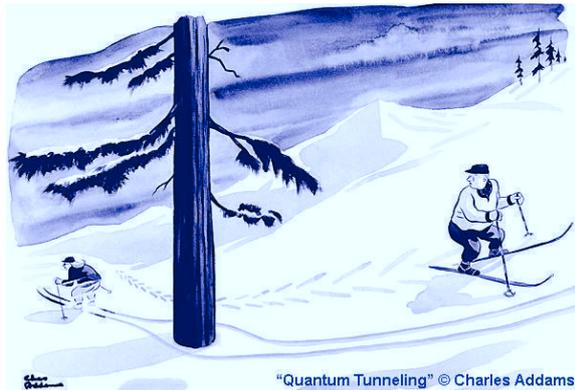
The circuits we study are made of Josephson junctions which consist of two aluminum electrodes, separated by a thin insulating layer. The electrical transport through such a junction is based on tunneling of Cooper pairs. The strength of the tunnel coupling between the electrodes is described by the Josephson energy E_J of the junction. Junctions with large E_J are very transparent for Cooper pairs, and therefore have a large supercurrent. On the other hand, the energy needed to charge the capacitance of the junction with a single electron is given by the charging energy E_C. If E_C is large, the conduction of Cooper pairs, which implies the successive charging and discharging of the junction capacitance with charge $2e$, has a high energy cost. Therefore the tunneling is progressively suppressed. The competition between the two energy scales E_J and E_C reflects the fact that charge Q on the junction capacitance and phase difference φ between the superconducting electrodes are conjugated variables [19]. Thus they respect the Heisenberg uncertainty principle: $\Delta Q \cdot \Delta \varphi \gtrsim h$. If the charge is well defined, the superconducting phase fluctuates and vice versa. A jump of 2π of the superconducting phase is called a *phase-slip* and it can occur due to the quantum fluctuations of the phase. As charge and phase are conjugate variables, the phase-slip is the dual effect to the tunneling of one Cooper pair. Phase-slips have initially been studied in nanowires, in the context of the superconducting to insulator transition [20–22]. However, the experimental control of the phase-slip amplitude in nanowires is very difficult. Josephson junction chains provide much more flexible and designable systems, where the relevant parameters E_J and E_C can be accurately tuned.

This thesis presents an experimental study of quantum phase-slips (QPS)

in Josephson junctions circuits. Our research has been motivated by two possible applications of QPS. The first one is the fabrication of a **_topologically protected quantum bit_** and the second one is the possible definition of a new current standard, based on a quantum phase-slip **_frequency-to-current conversion device_**. In the following I will present a brief overview of these two devices based on phase-slips.

The topologically protected qubit A qubit is a quantum two level system which constitutes the basic computational element in the architecture of a quantum processor [23]. At the moment, superconducting circuits are among the most promising candidates for the physical realization of a qubit [24, 25]. There are several classes of superconducting qubits, depending on the physical nature of the $|0\rangle$ and $|1\rangle$ states. Charge qubits [26] use the two lowest charge states of a small superconducting island to define the logical states. In flux qubits the states are defined by the direction of circular electrical currents [11] while in phase qubits [27] the first two energy levels, associated to the phase dynamics of a Josephson junction, define the $|0\rangle$ and $|1\rangle$ state. In the last few years, an impressive number of basic few qubit manipulations have been demonstrated: high fidelity single shot readout [28] and quantum non demolition measurement for single qubits [29, 30], microwave-induced cooling of a superconducting qubit [31], two-qubit coupling and quantum algorithms [16, 32] or three-qubit entanglement [17, 18]. However, the main drawback in all these devices is the short coherence time, compared to the time needed for a fault-free operation. The short coherence time is a direct consequence of the fact that the qubit is coupled either to microscopic fluctuators [33, 34] or to the macroscopic electrical environment. Current research seeks to enhance the coherence time of superconducting qubits either by improving the materials or by proposing various decoupling schemes. Even though the typical coherence time of superconducting qubits increased significantly in the last years [35, 36], it is still too short for quantum error correction codes to converge.

Recently, a new qubit design composed of 2D rhombi networks, has been theoretically proposed [37–39]. Its building block, the rhombus, is a flux qubit consisting of a superconducting loop, threaded by magnetic flux, containing four identical Josephson junctions. A chain of N rhombi is characterized by complex $N-body$ quantum states. When the flux threading the rhombus is $\Phi_0/2$ (where Φ_0 is the flux quantum), the levels in the low energy spectrum become highly degenerated and we only get two macroscopically different states. These states are separated from the high energy spectrum by a gap G. It has been theoretically shown that at $\Phi_0/2$, the levels are protected from a local noise M up to order $(M/G)^N$.

The first experimental study of a topologically protected rhombi qubit was done by S. Gladchenko et al. [40]. The simplest protected qubit is a chain of two rhombi, connected to a superconducting island (Fig. 2a). The two degenerate quasi-classical phase states for the island are $|\varphi = 0\rangle$ and $|\varphi = \pi\rangle$. A finite probability of phase tunneling between the states (phase-slip) removes the degeneracy and results in a small energy splitting ξ between the energy states of the qubit: $1/\sqrt{2} \, (|0\rangle \pm |\pi\rangle)$. The qubit energy splitting ξ depends on the parameters of the superconducting circuit: the number of rhombi N in the chain, the ratio E_J/E_C and the ground coupling C_0 of the middle island. In order to measure the qubit, we add a second,

identical chain of rhombi on the right side of the island and thus, close the electrical circuit (Fig. 2b).
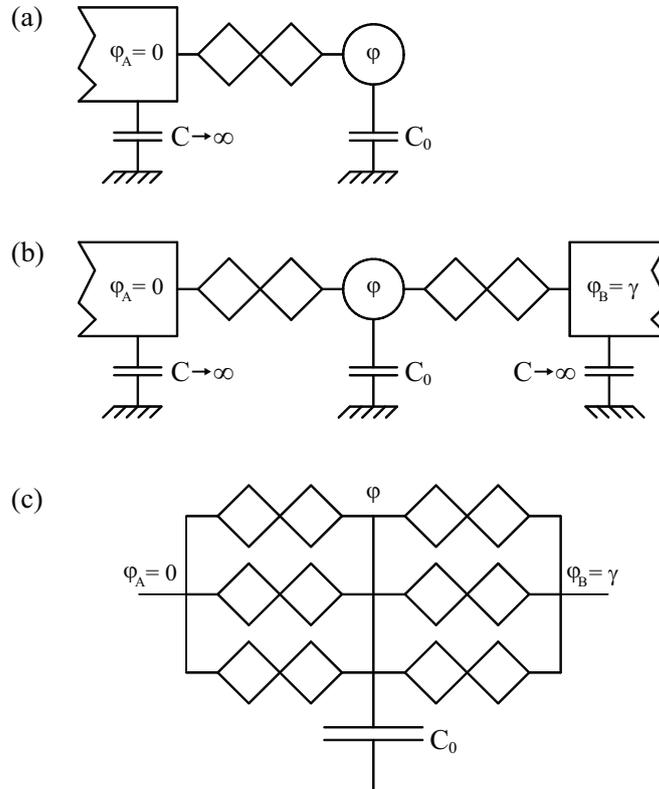
Fig. 2: The rhombi qubit design

Numerical simulations show that the qubit protection can be optimized by using several rhombi chains in parallel to connect the central island to the leads [40], as shown in Fig. 2c. In chapter 4 of this thesis we have studied both the 2D rhombi network and the linear rhombi chain in the regime of strong and weak phase-slips.

Frequency-to-current conversion device Another possible application of QPS is a frequency-to-current conversion device, that could be used to redefine the electrical current unity, the Ampere, with better metrological accuracy. Single charge effects in micrometer sized circuits have been measured since the begining of the 90's [41–43]. In the last years significant progress has been made in the measurement of current by counting single electrons [44–47]. The main problem with these techniques for applications in metrology is the low value of the resulting electrical current. A fundamentally alternative route is to exploit the duality between current and voltage in a so called *phase-slip junction*. A phase-slip junction is a device where instead of tunneling of Cooper pairs, tunneling of the superconducting phase (quantum phase-slip) is dominant. Theoretically, by irradiating a phase-slip junction in the insulating state with microwave radiation at frequency f in the range of GHz, we expect to measure current steps in the IV characteristic, at values up to a few nA. Despite numerous efforts [48, 49], a clear step at $I = 2ef$ has not yet been measured. One of the reasons is that in order to keep quantum charge fluctuations

small, the junction needs to be embedded in a high impedance environment, with a typical value larger than the quantum resistance $R_Q = h/(2e)^2 \simeq 6.5\,\mathrm{k\Omega}$. The practical realization of such a high impedance is very challenging. Recently, superconducting nanowires [50] or Josephson junctions chains [51] have been proposed for the implementation of a phase-slip junction.

In this thesis we study in detail QPS in Josephson junction chains of different sizes (chapter 5). We have measured the quantum phase-slip rate in a chain of 6 junctions in the regime $E_J \geq E_C$, while tuning the parameter E_J, and found the results to be in good agreement with the theoretical expectations [52]. We have demonstrated the quantum nature of the phase-slips in a 6 junction chain by measuring Aharonov-Casher interference [53,54] of phase-slips occurring on different junctions of the chain. We induced polarization charges on the islands of the chain and we observed complex interference patterns which we could fit using the basic tight-binding model of K. Matveev et al. [52].

We have also measured a long, 400 Josephson junction chain (section 5.6 and 5.7). We found that for long chains, the stray capacitance C_0 of the chain islands to the ground plays an important role and limits in our case the quantum phase-slip rate. Also, the ground coupling C_0 lowers the characteristic frequency of the plasma modes in the Josephson junction chain. For the 400 junction chain we measured the resonance frequency of the three lowest standing-wave modes.

Structure of the manuscript

In chapter 2 we start with a detailed description of the mesoscopic device fabrication and the measurement set-up. In the last sections of this chapter we discuss the junctions' stability in time and the variance of the characteristic parameters for identically fabricated junctions.

Chapter 3 is a theoretical introduction to the phase dynamics of a current biased Josephson junction. We discuss the technical details of using a read-out Josephson junction to measure the current-phase relation of a superconducting circuit. In the last section of the chapter we briefly present the theoretical methods we used for the quantitative analysis of the measured current-phase relations.

In chapter 4 we study the ground state of several rhombi circuits. We measure the ground state of an 8 rhombi chain, both in the classical $E_J \gg E_C$ and in the quantum limit $E_J \geq E_C$. We also measure the ground state of a 2D rhombi network, which was designed to realize a topologically protected qubit.

We present a detailed study of QPS in Josephson junction chains in chapter 5. We have measured the effect of QPS on the ground state of a 6 junction chain. We have also measured Aharonov-Casher interference of phase-slips. In the last sections of the chapter we discuss phase-slips in long ($N = 400$) Josephson junction chains.

Chapter 6 is devoted to a detailed study of the macroscopic quantum tunneling (MQT) of phase from an arbitrary shaped potential well. We present detailed escape probability measurements which we compare with two theoretical models: the numerical model of section 3.3 which takes into account the exact shape of the

potential and an effective rectangular potential approximation which gives almost accurate analytical solutions. In this chapter we also show that the accuracy of the current-phase measurement is altered if the read-out junction is in the underdamped phase diffusion (UPD) regime.

Chapter 2

Device fabrication and measurement set-up

In this chapter we will present the experimental techniques we have used for the fabrication of the studied superconducting circuits. The central elements of our circuits are $Al/AlO_x/Al$ Josephson junctions. In section 2.1 and 2.2 we explain the different steps of the sample fabrication. In the following sections we present the sample wiring (section 2.3) and the measurement set-up (section 2.4). In section 2.5 we aim to answer the following question: how identical are identically fabricated junctions? In section 2.6 we will present measurements that prove the extraordinary time stability of the junctions parameters. We also discuss the essential fabrication steps that allow us to obtain stable junctions.

The samples were fabricated at the *Nanofab* platform, in the *Neel Institute*, CNRS Grenoble. The support of the technical team was essential in maintaining a steady fabrication rythm. The key fabrication machines were the Leo 1530 SEM equipped with a RAITH Elphy e-beam lithography system and the home built ultra high vacuum (UHV) e-beam deposition chamber. During my thesis I have spent a total of $\sim 30\,\%$ of my time fabricating the samples.

2.1 Fabrication of Josephson junctions

All samples were fabricated in one lithography step, using standard bilayer techniques. During the thesis we have also developed multiple lithography step processes, which up to now have not been used for the fabrication of a working sample, and therefore we will not discuss them. The main fabrication steps are represented in Fig. 2.1 and we will describe them in detail in the following.

Resist deposition We start with a clean Si/SiO_2 wafer. The SiO_2 thickness is 500 nm. In order to be sure that the wafer is absolutely clean, we introduce it for 1 minute in an oxygen plasma in the chamber of a Reactive Ion Etching (RIE) machine. The first resist of the bilayer, the PMMA/MAA (ref. ARP 617.09) is deposited on the Si/SiO_2 wafer, using a spinner. The thickness of the resist layer depends on the rotation speed of the spinner and is typically between $0.5\,\mu$m and $1\,\mu$m. The wafer is then baked for 5 minutes at 200^oC on a hot plate. We then
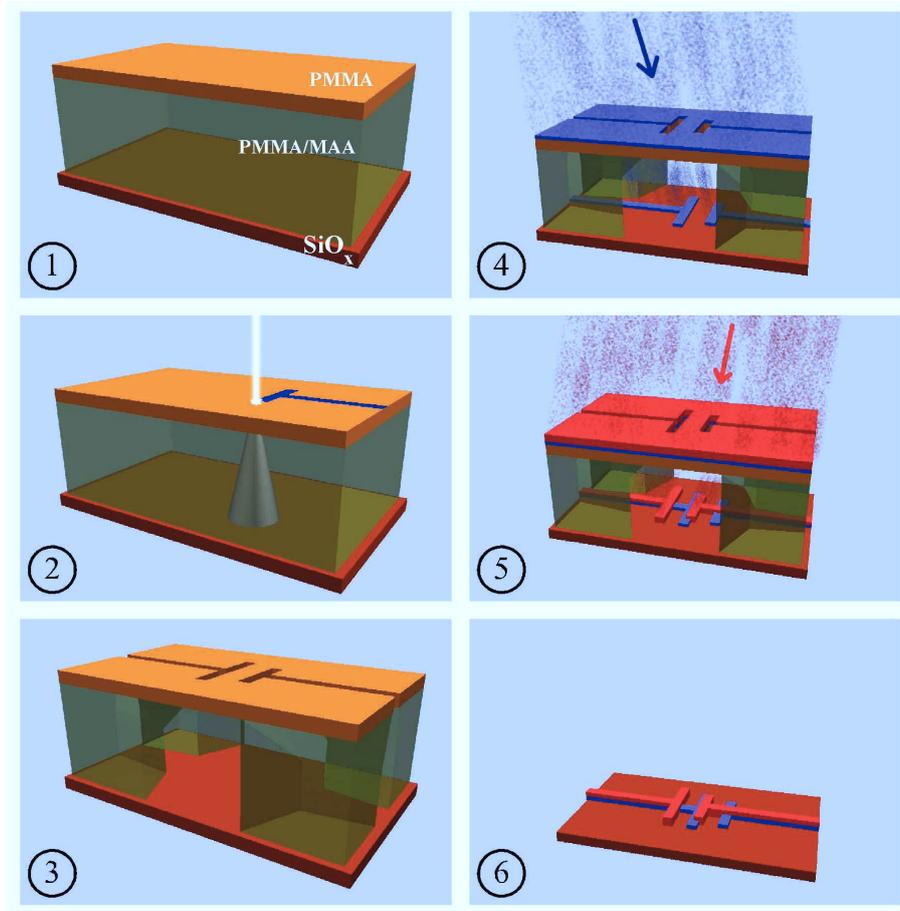
Figure 2.1: Representation of the main steps of the junction fabrication.
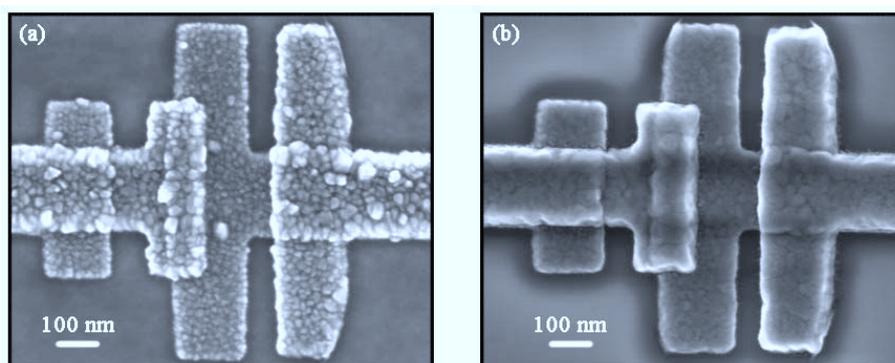
Figure 2.2: SEM images of $Al/AlO_x/Al$ Josephson junctions. The JJ in (a) was deposited at low evaporation speed: $0.05\,nm/s$ and the one in (b) at high speed: $1\,nm/s$. Notice the difference in roughness between the two aluminum films in (a) and (b).

deposit the second resist of the bilayer, the PMMA (ref. ARP 679.04). The typical thickness of this layer is 100 nm. We bake the wafer for 1 hour at 180ºC to ensure that the resists are solid and they will not bend during the next fabrication steps. The complete recipe for the resist deposition is presented in the first part of Table 2.1. A graphic representation of the wafer after the deposition of the two resist layers is shown in Fig. 2.1(1). The first resist layer is represented transparent for pedagogical purposes, in order to facilitate the visualization of the 3D structures.

E-beam lithography   The Si/SiO_2 wafer with the two resist layers is patterned by exposing it to a beam of electrons accelerated to 20 kV. For the e-beam exposure we have used a LEO 1530 Field Emission Scanning Electron Microscope (FESEM) piloted by a RAITH Elphy plus system. The e-beam lithography is used to write both the fine structure of the pattern, that will define the Josephson junction circuit within a write field of $100 \times 100 \, \mu m^2$, and the large features like the connecting wires and bonding pads, for which we use a write field of $1.6 \times 1.6 \, \mathrm{m}m^2$. For the exposure of patterns larger than the write fields, the system is equipped with a stage that moves using a step motor with an accuracy of $\pm 5 \, \mu$m. The typical parameters of the e-beam exposure are presented in Table 2.1. The e-beam patterning of the resists is represented in Fig. 2.1(2). Notice that the electron beam is scattered inside the bottom resist layer and it exposes a larger volume than inside the top layer, where the beam is still well focused.

Development and wafer cleaning   After the e-beam exposure, the resists are developed in chemicals which only dissolve the exposed areas. The development is realized in three steps. We first drop the wafer in a mix with volume ratio 1/3 of MIBK (Methyl isobutyl ketone) and IPA (Isopropanol), for 30 seconds. The exposed inferior resist layer is three times more sensitive to the solvent than the superior layer. Thus, an undercut is obtained, as represented in Fig. 2.1(3). In the central areas of Fig. 2.1(3), where the bottom resist was completely removed, the top layer forms a suspended bridge of resist. The second step consists in introducing the wafer in a mix with volume ratio 1/x of Ethanol and IPA, for 1 minute. The actual value of x is in the range between 1 and 3 and it needs to be optimized for each mask design. During this step of the development, the Ethanol, which is a stronger solvent than IPA, increases significantly the undercut and it also cleans the wafer of resist residues. We will show in the following section that this step is important for the fabrication of junctions stable in time. During this step, the superior resist is almost unchanged. The last step of the development consists in rinsing the wafer for 1 minute in pure IPA. Finally, after the development, the wafer is cleaned with oxygen plasma using a RIE system, to remove any residues of resist. The plasma is tuned to low power and high pressure to ensure a homogeneous, non directional cleaning of the wafer regions exposed by the undercut. The junctions will be deposited in these regions. The development parameters are synthesized in Table 2.1.

Shadow evaporation   The $Al/AlO_x/Al$ tunnel junctions are deposited on the Si/SiO_2 substrate using the well known shadow evaporation technique [55]. By

evaporating aluminum through the suspended resist mask, the pattern is projected on the substrate. The displacement λ of the projection position on the substrate,
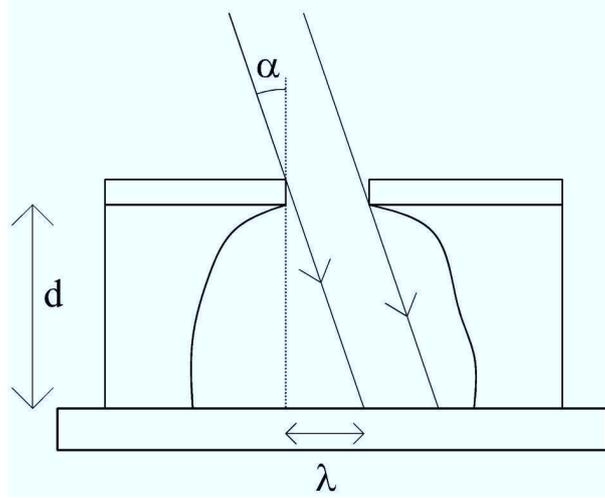

Figure 2.3: Schematic representation of the angle evaporation.

compared to the position of the resist pattern, depends on the tilt angle α of the wafer plane with respect to the evaporation direction and the thickness d of the bottom layer resist, as represented in Fig. 2.3. In a first approximation, the displacement λ reads:

$$\lambda = d \cdot \tan \alpha \qquad (2.1)$$

There are two types of deviations of the value λ from eq. (2.1). The first correction is due to the thickness of the top layer, which shrinks the actual width of the deposited pattern. Typical evaporation angles α are in the range of $\pm 25^o$. Thus, the corrections due to the thickness of the top layer are in the range of a few tens of nanometers. The second correction comes from the fact that during the evaporation, the openings in the top resist shrink due to deposited material on the walls of the pattern. During one evaporation we typically deposit a film with a thickness of $20 - 50 \, \text{nm}$. The corrections due to deposits on the walls of the resist pattern are also in the range of a few tens of nanometers. Depending on the sample design, these two types of deviations might need to be compensated.

When the metal is evaporated from two different angles, by carefully adjusting the geometry, we can obtain an overlap between the two deposits (see Fig. 2.1(4) and (5)). The surface of the overlap gives the surface of the junction. The aluminum films are deposited in a UHV system with a base pressure of $10^{-9} \, \text{mbar}$. The high homogeneity of the aluminum films is essential because the aluminum superconducting gap is very sensitive to impurities [56]. If the purity of the two electrodes is not well controlled, we might expect that different islands of the superconducting circuit might have different gaps. It has been shown in Ref. [57] that islands with different gap values practically form $1e$ quasiparticle traps, which can significantly perturb the expected behavior of the measured superconducting devices.

The speed of the aluminum deposition has an important effect on the roughness of the film. In Fig. 2.2 we present SEM images of two junctions obtained with

wafer cleaning
RIE - oxygen plasma - 1 minute -

resist deposition	
bottom resist	PMMA/MAA (33%) diluted 9% in 1-methoxy-2-propanol (ARP 617.09 from *AllResist*)
spin speed	6000 RPM
spin acceleration	4000 RPM/s
time	30 s
thermal treatment	5 minutes at 200^oC
measured thickness	500 nm
top resist	PMMA diluted 2% in Ethyl-Lactate (ARP 679.04 from *AllResist* diluted 50%)
spin speed	4000 RPM
spin acceleration	2000 RPM/s
time	30 s
thermal treatment	60 minutes at 180^oC
measured thickness	100 nm

e-beam exposure at 20kV	
high resolution	write field: $100 \times 100\,\mu m^2$, pixel size: $4.6\,nm$, aperture diameter: $7.5\,\mu m$, e-beam current: $20\,pA$, dose: $300\,\mu C/cm^2$
low resolution	write field: $1600 \times 1600\,\mu m^2$, pixel size: $60\,nm$, aperture diameter: $120\,\mu m$, e-beam current: $4800\,pA$, dose: $270\,\mu C/cm^2$

development
MIBK/IPA 1/3 during 30 s
Ethanol/IPA $1/x$, $1 \leq x \leq 3$ during 60 s
IPA during 60 s

wafer cleaning
RIE - high pressure, low power oxygen plasma - 20 s -

shadow evaporation	
1st evaporation	$\alpha \simeq 20^o$, deposition speed: $0.2\,nm/s$, thickness $\sim 20\,nm$
oxidation	5 minutes at $5 \cdot 10^{-2}\,mbar$ pure oxygen the tunnel resistance is $100\,\Omega \cdot \mu m^2$
2nd evaporation	$\alpha \simeq -20^o$, deposition speed: $0.2\,nm/s$, thickness $\sim 50\,nm$

Table 2.1: Technical parameters of the circuit fabrication. The exact values of the parameters are slightly different, optimized for each sample design.

very different evaporation speeds. The typical deposition speed that we used for our samples is $0.2\,\mathrm{nm/s}$. We will come back to the influence of the film rugosity on the junction parameters in section 2.5.

Between the first and the second deposition, the sample is moved to the loading lock, which is at a pressure of $10^{-7}\,\mathrm{mbar}$ and pure oxygen is let into the chamber until the pressure reaches values in the range of $10^{-2}\,\mathrm{mbar}$. We then wait for 5-10 minutes in order to allow the oxidation of the electrode and create the barrier of the tunnel junction. The thickness of the tunnel barrier, and implicitly the tunneling resistance of the junction, depends on the pressure during the oxidation.

Resist lift-off Once the second deposition is finished, the electrical circuit fabrication is over. We now need to clean the wafer by removing all the resist and the aluminum deposited on top of it. The chip is plunged in NMP (N-Methyl-2-pyrrolidone), a solvent that removes the resist mask. The resulting junction is schematized in Fig. 2.1(6). In order to speed up the lift-off process, we heat the solvent at 80°C for about one hour and then we apply ultrasound for one minute. The ultrasonic power should be low in order to avoid damaging the aluminum films. In Fig. 2.2 we present e-beam images of two junctions after lift-off.

2.2   Fabrication of SQUIDs and rhombi

In this section we present the masks and the evaporation sequence that we have used to fabricate the SQUIDs and the rhombi. We call rhombi a superconducting loop interrupted by 4 junctions. The steps of the fabrication are presented in detail in the previous section (section 2.1).

In Fig. 2.4a, we represented the top resist mask, after development, which was used for the fabrication of one SQUID. This design was used for the fabrication of the 6 SQUID chain sample discussed in chapter 5. In Fig. 2.4b and c we schematized the resulting aluminum films, after the first and the second angle evaporation. Notice that the bottom electrode is always larger than the top one, in order to be able to define precisely the surface of the junction. In Fig. 2.5 we present the SEM image of the first SQUID in the chain.

In Fig. 2.6a, we represented the top resist mask, after development, which was used for the fabrication of one rhombus. The mask design is optimized to produce identical junctions. It accounts for the fact that there is a small hysteresis in the e-Beam writer lenses, by always repeating the same drawing sequence for the electrodes of the junctions. In Fig. 2.6b and c we schematized the resulting aluminum films, after the first and the second angle evaporation. Notice that the directions of the evaporation, represented by the arrows, are perpendicular to the x-axis of the rhombus, compared to the evaporation axes for the SQUIDs, which were parallel to the x-axis. This design was used for the fabrication of the 8 rhombi chain sample presented in chapter 4. In Fig. 2.7 we plot the SEM image and the AFM profile of one rhombi in the chain.
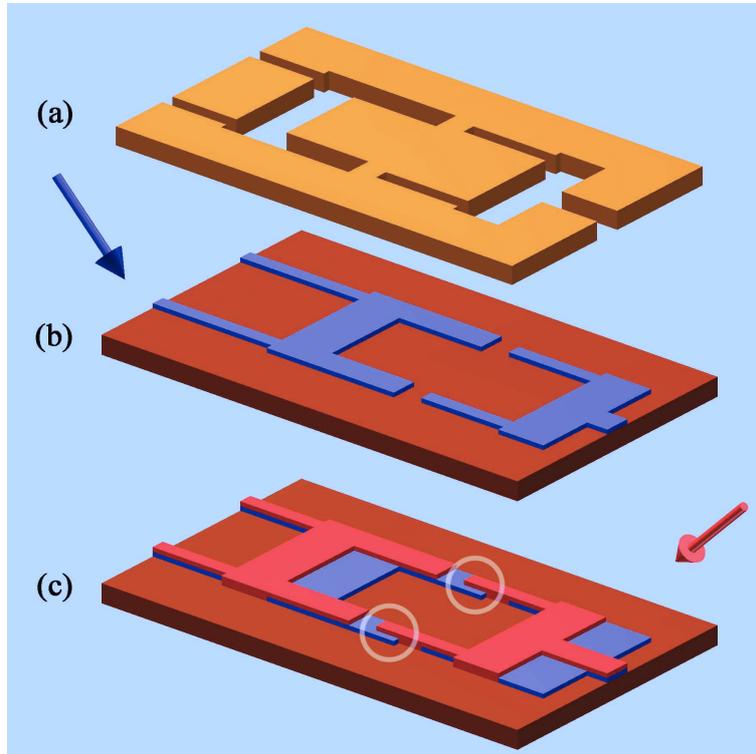
Figure 2.4: Resist mask and evaporation sequence for the fabrication of a SQUID. The two junctions of the SQUID are highlighted by the white circles in (c).

500 nm
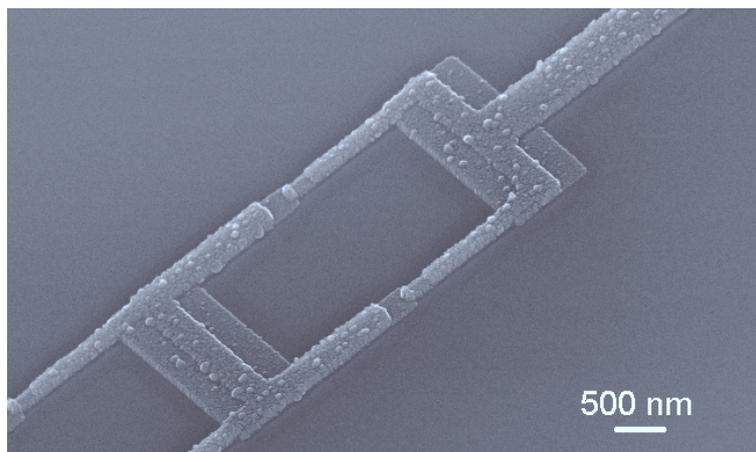
Figure 2.5: e-Beam image of the first SQUID in a chain.
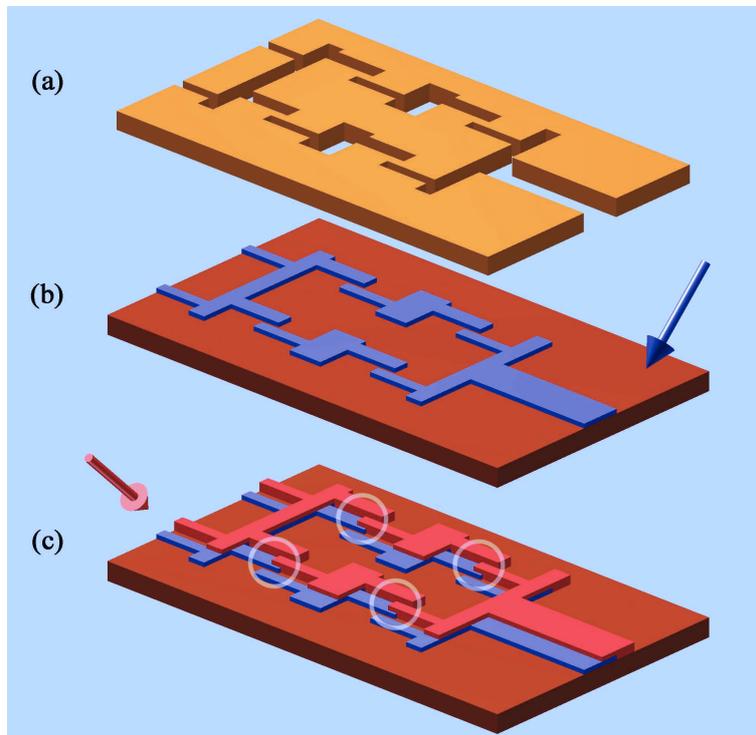
Figure 2.6: Resist mask and evaporation sequence for the fabrication of a rhombus. The four junctions of the rhombus are highlighted by the white circles in (c).
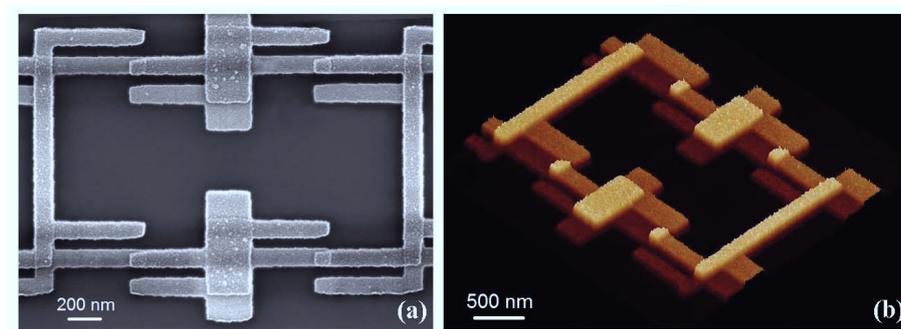
Figure 2.7: e-Beam (a) and AFM profile (b) of a rhombus inside a rhombi chain.

2.3 Design of the on-chip connecting wires and bonding pads

In this section we discuss the technical details of connecting the Josephson junction circuit to the measurement electronics. In Fig. 2.8 we present an e-beam image of the entire sample chip. The image corresponds to the actually measured 6 SQUIDs chain sample (see chapter 5). The aluminum circuit, fabricated using the lithography method detailed in the previous sections, is visible on top of the Si/SiO_2 wafer. The background of the image is given by the conductive carbon adhesive tab, which is used to glue the chip on the SEM sample holder.
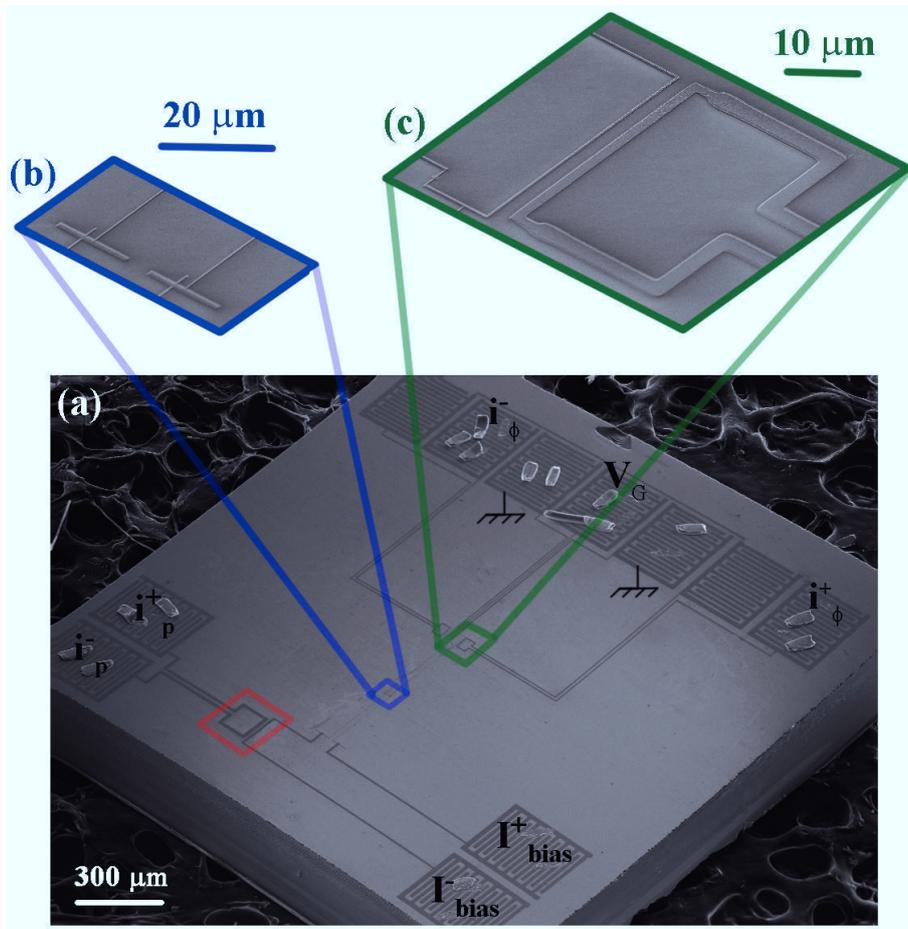
Figure 2.8: SEM image of the entire sample circuit and the Si/SiO_2 chip. The image corresponds to a measured sample: the 6 SQUIDs chain. The traces from the bonding wires are visible on the contact pads. The red line highlightes the mutual inductive coupling region between the DC bias lines and the fast measurement pulse line. In (b) we show a detailed view of the overlaping region between two succesive e-beam write fields. In (c) we present a detailed image of the flux bias current loop.

In Fig. 2.8a we can see all 11 contact pads of the sample. On top of the contact pads we can also see traces of the aluminum wires that were used to contact the circuit. Two of the pads are redundant and they were not used. Notice

the meander shaped pads, which were designed to avoid magnetic flux trapping. In addition, the meanders also constitute a rugged surface, which is ideal for the mechanical bonding of the contact wires.

The sample, which is located in the center of the wafer, is connected to the current bias pads labeled in Fig. 2.8a by I_{bias}^{+} and I_{bias}^{-}. Between the sample and the pads, we have used two types of connecting wires. Close to the pads, we used wide ($2000 \times 50\,\mathrm{n}m^2$) wires, which form a loop inductively coupled to the nanosecond current pulse lines, labeled by i_p^{+} and i_p^{-}. In the red highlighted region in Fig. 2.8a we can observe the fast current loop inductively coupled to the low frequency current bias lines. The mutual inductance M is $\sim 50\,\mathrm{pH}$. The position of the fast current loop is optimized for minimum coupling to the sample loop. Close to the sample we used thin lines ($200 \times 50\,\mathrm{n}m^2$), which provide a significant kinetic inductance $L \simeq 6\,\mathrm{nH}$ and play an important role in decoupling the sample from the noise in the bias lines. These thin lines were e-beam exposed in two successive steps, using a small $300 \times 300\,\mu m^2$ write field. Once the exposure is completed in one write field, the SEM sample holder moves to the new writing position. In order account for the step motor positioning error of $\pm 5\,\mu$m, at the left end of each wire inside a write field, we add a perpendicular line, $10\,\mu$m long. Also, the write fields superpose over $10\,\mu$m. In Fig. 2.8b we present a detailed image of the connecting area between two writing fields.

Close to the sample, which is sensitive to magnetic flux, we added on-chip current lines which we usually call *flux lines*. They allow us to independently tune the overall perpendicular magnetic field and the magnetic flux in one region of the sample. A detailed SEM image of a current loop is presented in Fig. 2.8c. The maximum current that can pass through the lines, without heating the sample, is approximately $100\,\mu$A. This means that for a typical mutual coupling of $10\,\mathrm{pH}$, we can sweep the local flux from $-\Phi_0/2$ to $\Phi_0/2$, which is sufficient if the physics of the studied system is Φ_0 periodic.

As we mentioned before, the exact design we described above corresponds to a particular sample: the chain of 6 SQUIDs. However, for the other samples that we will discuss in this manuscript, even though the design might differ in details, it remains very similar to the one presented in Fig. 2.8.

2.4 Measurement set-up

The majority of the measurements are performed in a dilution fridge at $T = 50\,\mathrm{mK}$. In this chapter we present the electrical set-up from room temperature down to the dilution stage. Some of the measurements (see chapter 4) were performed in a ^3He refrigerator at $T = 300\,\mathrm{mK}$. The electrical scheme inside the ^3He refrigerator is similar to the one of the dilution.

We have implemented two types of biasing schemes. Fig. 2.9 shows the measurement set-up for the current biased samples, while Fig. 2.10 presents the set-up for the voltage bias measurements. In the following we discuss each of these set-ups separately.

Current bias Basically our experiments consist in measuring the switching current of the superconducting sample to the dissipative regime. Figure 2.9 shows the measurement set-up. All instruments are controlled by a *PC* via custom programed *LabVIEW* programs. The current bias is realized by applying a voltage to a $500\,\mathrm{k\Omega}$ resistance in series with the sample, at room temperature. The resulting voltage over the circuit is amplified at the top of the cryostat by a differential amplifier *LI − 75ANF* and measured by a home-made electronic box [58] that compares this voltage to a threshold voltage. This electronic box contains a fast switch that cuts the bias current as soon as the voltage over the sample is larger than a certain threshold voltage. The value of the threshold voltage is typically set to $40\,\mu\mathrm{V}$, which represents $10\,\%$ of the superconducting gap voltage for aluminum. A control card that has been optimized in the laboratory counts the number of times that the voltage over the circuit exceeds the threshold voltage.

The high frequency signals (*HF* 1 and *HF* 2) are guided by $50\,\Omega$ coax lines which are $40\,\mathrm{dB}$ attenuated at low temperature. They have a band width up to 20 GHz. The *DC* lines used for current biasing (*I*+ and *I*−), voltage measurement (*V*+ and *V*−) and gate voltage control (V_G) contain *RLC* filters at the cryostat entrance, at room temperature, with a cut-off frequency of $500\,\mathrm{kHz}$. Under $1.5\,\mathrm{K}$ these lines consist of thermocoaxial cables of a length of $75\,\mathrm{cm}$ that attenuate signals with frequency above $1\,\mathrm{GHz}$. They are followed by two π filters. The whole set-up has an attenuation of $-100\,\mathrm{dB}$ for frequencies above $1\,\mathrm{GHz}$.

The cryostat is magnetically shielded by successive layers of soft magnetic material $\mu - metal$ (a nickel-iron alloy) at room temperature and at $77\,\mathrm{K}$. At $4\,\mathrm{K}$, the calorimeter is surrounded by a superconducting *Pb* layer, which freezes the value of the magnetic flux. Inside the superconducting shield, but outside the calorimeter lies a superconducting coil, which can produce magnetic fields up to $B = 100\,\mathrm{Gauss}$.

The electrical environment close to the sample consists of a low-pass *LC* filter. In Fig. 2.11 we present a photo of the sample holder (a) and the corresponding electrical scheme (b). The inductance of the filter is typically $L_w \simeq 10\,\mathrm{nH}$ that is provided mainly by the kinetic inductance of long and thin superconducting current biasing lines on the sample chip (see Figure 2.8). The sample is bonded in parallel to a homemade [59] $NbTi/Al_2O_3/NbTi$ capacitance, situated on a second chip. The value of this capacitance is $C_p = 270\,\mathrm{pF}$. The resonance frequency of this filter is in the range of $100\,\mathrm{MHz}$.

Voltage bias Our experiments consist in measuring the electrical current *I* as a function of the voltage bias *V*. Figure 2.10 shows the measurement set-up. We use the same electrical lines in the dilution cryostat as explained in the previous paragraph. The current *I* is measured using a *FEMTO-DHPCA-100* variable gain high speed current amplifier. The voltage source *V* and the voltmeter V_{out} which reads the current amplifier output, are situated on a *NI PCI-6281 M Series* data acquisition board, optimized for 18-bit analog input accuracy and controlled by a *PC*. The ground of the *PC* is disconnected from the cryostat ground by a homemade ×1 amplifier. Special care has been taken to shield the sample against spurious electromagnetic radiation and to avoid any *ground loops* which could induce current noise.

18



Figure 2.9: Experimental set-up for the switching current measurements. The sample is current biased. The superconducting coil is at $4\,K$.
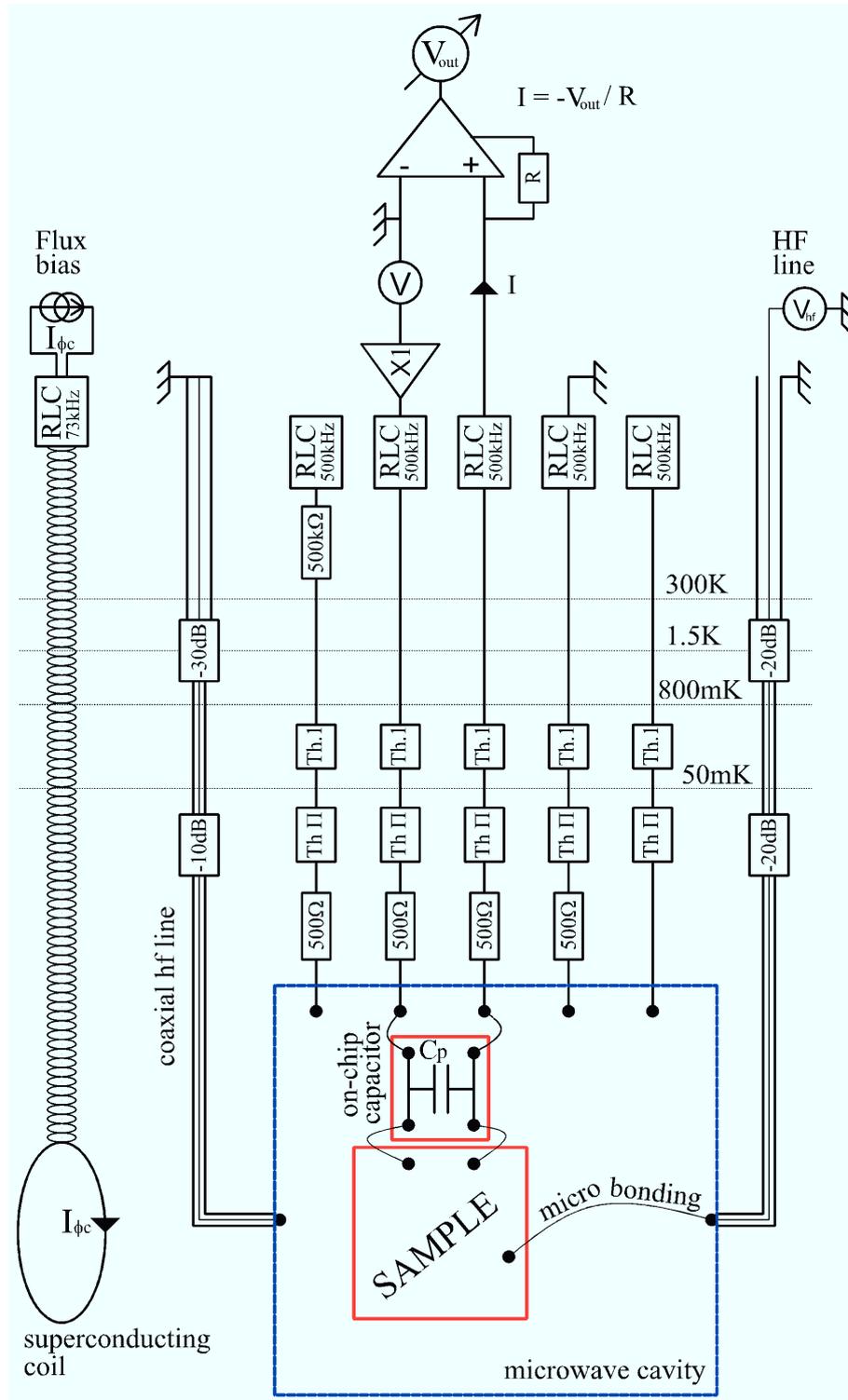
Figure 2.10: Experimental set-up for the voltage biased samples. The superconducting coil is at $4\,K$.
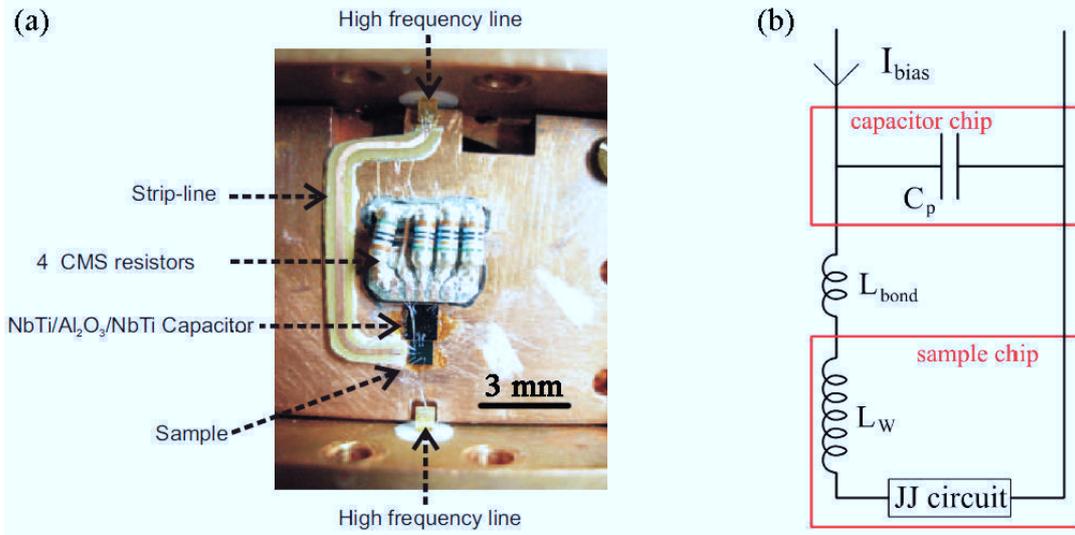
Figure 2.11: Photo of the sample holder (a). The microwave cavity is defined by the copper cap on top of the sample holder, which isolates a volume of approximately $3 \times 3 \times 1 \, mm^3$, around the sample chip. (b) Electrical scheme of the environment near the sample.

2.5 Measurement of the variance for identically fabricated junctions

We will now address the following question: what is the tunnel barrier variance for identically fabricated $Al/AlO_x/Al$ junctions? We have fabricated several sets of ~ 100 junctions that we contact and measure individually at room temperature. The junctions had critical current densities in the range of $500 \, \mathrm{nA}/\mu m^2$. The size of the junctions depends on the sample, ranging from $0.02 \, \mu m^2$ to $0.1 \, \mu m^2$. This class of $Al/AlO_x/Al$ junctions are widely used in superconducting quantum electronics. If we fabricate complex circuits containing many junctions, the question of fabrication reproducibility is crucial.

The sample design is presented in Fig. 2.12. The geometry of the sample was optimized to enable the packing of a large number of junctions in a small area of the wafer, in order to minimize the variations of resist thickness. The junctions are connected individually, by wires of identical resistivity. As we can see in Fig. 2.12c and b, we fabricated sets of 10 junctions, plus a reference wire, which are grouped together within an area of a few mm^2.

In Fig. 2.13 we present a typical measured histogram for the tunnel barrier R at room temperature. For clarity, the $x - axis$ is reported in units of the mean value for the resistance: R_{mean}. The value of R_{mean}, depending on the sample, is of the order of a few kΩ. The distribution is well fitted (see the blue line in Fig. 2.13) by a Gaussian law:

$$N_J(R) = N_{tot} \frac{1}{\sqrt{2\pi\sigma^2}} exp \left[-\frac{(R/R_{mean} - 1)^2}{2\sigma^2} \right] \qquad (2.2)$$

where σ^2 is the variance, in units of R_{mean}^2 and N_{tot} is the total number of measured
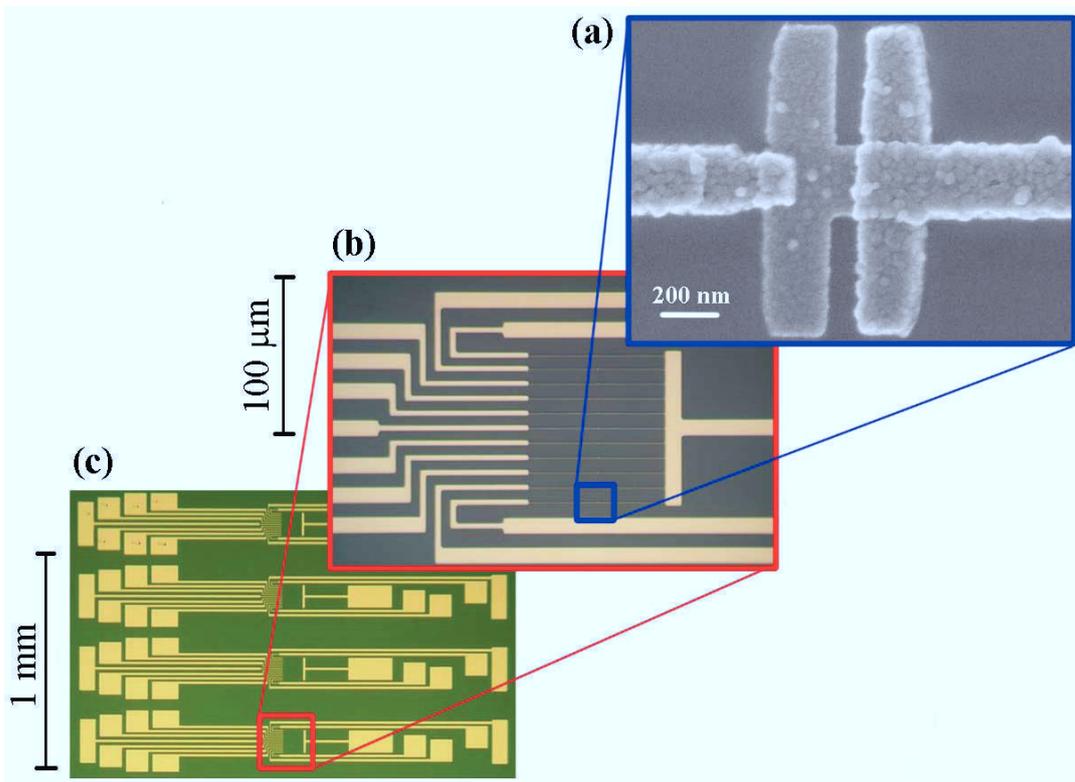
Figure 2.12: Images of the circuit fabricated to measure the junctions tunnel barrier variance and time stability (see also section 2.6). In (a) we present a SEM image of one junction. In (b) and (c) we show optical images of one of the measured samples at different magnifications.
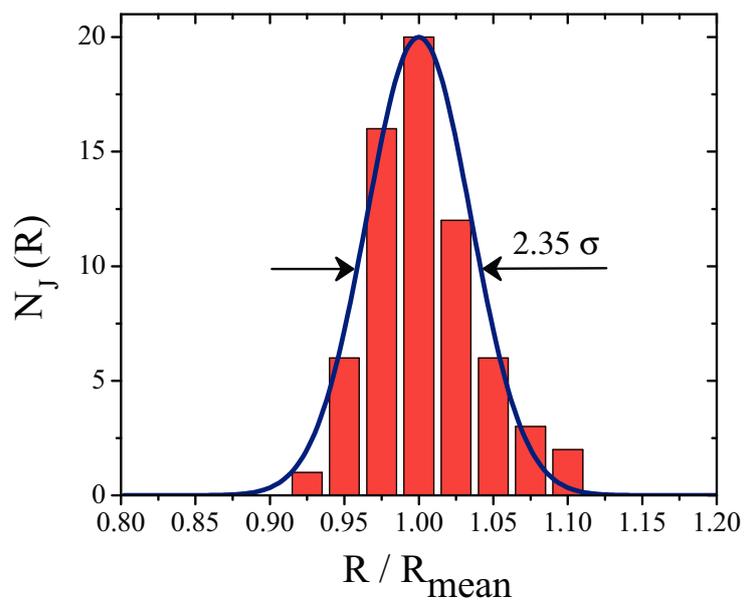

Figure 2.13: Measured histogram of the tunnel barrier resistance. In the figure we also represented the width at half height for the Gaussian fit, which is $\sim 2.35 \cdot \sigma$.

junctions. The measurements in Fig. 2.13 can be well fitted by taking the value $\sigma = 3.5\%$. For a Gaussian distribution 70% of the measured tunnel barrier values are in the interval $[R_{mean} - \sigma, \ R_{mean} + \sigma]$ and 95% of the values are in the interval $[R_{mean} - 2\sigma, \ R_{mean} + 2\sigma]$. Indeed, as we can observe in Fig. 2.13, the majority of the junctions are found in the interval $\pm 3.5\%$ from R_{mean} and practically all junctions are within an interval of $\pm 7\%$.
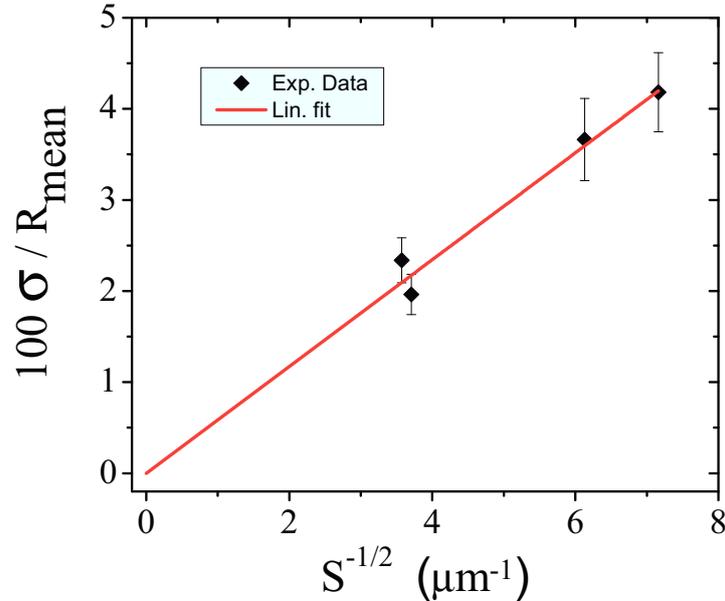
Figure 2.14: The measured tunnel barrier variance as a function of the junction surface. The red line is a linear fit passing through zero.

In the following, we study the dependence of the variance of the tunnel resistance with the size of the junctions. If we consider a model of randomly distributed conduction channels through the barrier of the junction, then we expect to measure smaller junction variance for larger junctions:

$$\sigma^2 = \eta \frac{1}{S} \tag{2.3}$$

Here, the prefactor η depends on the density of conduction channels ρ and it reads: $\eta = 1/2\rho$. The details of this model are presented in Appendix A.

In Fig. 2.14 we present the measured variance for sets of junctions with different surfaces. The values of σ are given by fits with the Gaussian law (2.2). The accuracy of each Gaussian fit is represented in Fig. 2.14 by the error bars associated with each experimental point. The red line in Fig. 2.14 represents a linear fit of the measured values for σ using eq. (2.3). The only fit parameter is the density of conduction channels, for which we obtain $\rho = 9 \cdot 10^3$ channels/μm^2, at room temperature. Using a conceptually different experiment, in Ref. [33] R. Simmonds et al. report the measurement of $5 \cdot 10^3$ channels/μm^2 in a similar type of junction, at a temperature of $50\,\text{mK}$. This agreement suggests the validity of the random conduction channels model.

Finaly we would like to make a comment on the influence of the junction electrodes roughness on the oxidation process. In Fig. 2.2 we show SEM images of two junctions deposited at very different evaporation speeds. The surface of the electrodes deposited at high speed Fig. 2.2b is obviously smoother than the surface of the low speed evaporated electrodes Fig. 2.2a. We would expect to observe significant differences between the measured variance of the two sets of junctions. However, for both sets of junctions, which are oxidized in similar conditions, we measure practically the same variance and mean value of the tunnel resistance. This result suggests that the obvious differences between the two aluminum layers visible in Fig. 2.2, do not play in important role during the oxidation process.

In conclusion, measurements on large ensembles of junctions at room temperature show that the variance of the tunnel barrier height is in the range of a few percents. This spread is considered acceptable for most types of superconducting circuits. We also showed that the size of the junction surface completely determines the variance of the tunnel barrier resistance, which is insensitive to the aluminum deposition speed.

2.6 Junction stability and the effect of annealing

In this section we report the fabrication of stable $Al/AlO_x/Al$ tunnel junctions, which do not age in time. We also investigate the effect of thermal treatments on the junction barrier. This issue is especially important for fabrication processes which involve annealing the junction.

Submicron sized metal-AlO_x-metal tunnel junctions are used in a wide range of applications. However, the time instability of the junctions is a frequently reported drawback. P. Koppinen et al. [60] reported systematic measurements of junction aging and they showed that the tunnel barrier could double its value within a period of a few weeks. A similar aging was observed in Ref. [61] for the capacitance C of the junctions, which significantly reduces its value after only a few days.

The junction aging is usually associated with two types of phenomena. Either (i) the diffusion of oxygen atoms from the oxide barrier to the electrodes or (ii) the change of the chemical composition of the barrier, by absorption or desorption of atoms or molecules other than oxygen. It has been shown that mechanism (i) plays a secondary role, accounting only for the slow drift of the junction parameters at long time scales, and it can can be suppressed by passivising the electrodes [62]. Mechanism (ii) is believed to play the dominant role in the time evolution of the junction parameters [60, 61, 63]. It has been shown that vacuum anneals at temperatures between $350\,^o$C and $450\,^o$C will accelerate the chemical relaxation processes in the barrier. The thermally treated junctions are stable and show improved characteristics [60, 64].

P. Koppinen et al. [60] also reported a significant decrease in the junction aging if the wafer is cleaned with an oxygen plasma just before the aluminum evaporation. As we will show in the following, we found that by aggressively cleaning the Si/SiO_2 substrate before the Al deposition, we could obtain perfectly stable junctions.

As we mentioned in section 2.1, there are two steps in the fabrication process
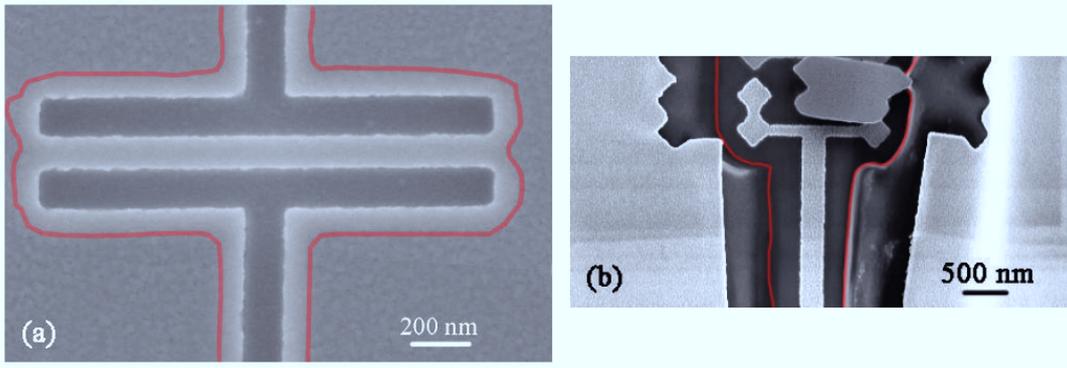
Figure 2.15: Imaging the undercut: SEM images of the wafer with the two resist layers, after a zero angle deposition. The patterned resist layers are well visible. In (a) the undercut can be observed in transparency as a more luminous region, that we highlighted for clarity using the red contour. In (b) we use high voltage, intense e-beam exposure to locally deform the resists and increase the gaps in the top layer. By this method we can directly observe the undercut contour, as highlighted by the red line.

that are essential to eliminate the resist residues on the substrate regions exposed by the undercut. First, during the development process, we plunge the wafer for 1 minute in a mixture of Ethanol and IPA (see Table 2.1). Ethanol is an aggressive solvent and it removes large volumes of resist from the undercut. This development step increases the volume of the undercut approximately four times. The top resist must be sufficiently strong and the pattern design must be adapted to avoid the bending of the top resist. The undercut size was monitored by two methods briefly presented in Fig. 2.15. We could either observe the undercut in transparency Fig. 2.15a, or directly, Fig. 2.15b, after opening larger gaps in the top resist layer.

The second wafer cleaning step is the RIE in oxygen plasma. The plasma parameters were adapted to ensure isotropic etching. This is not obvious because we have to clean a relatively large undercut surface, compared to the small access opening in the top resist. In the same time we do not want to destroy the patterns on the top layer of resist. The RIE process was optimized by the *Nanofab* team under the coordination of T. Fournier.

We tested the tunnel resistance R_N of the junctions at room temperature immediately after the fabrication process $R_N(0)$ and a few weeks later $R_N(t)$. We measured several ensembles of ~ 100 junctions (see Fig. 2.12) for which the fabrication conditions and the storage were identical. The resistance R_N is the average of the individually measured resistances. The results of our observations are presented in Table 2.2. For the junctions of chip A and B we did not observe any aging. For sample C we measured a slight increase in the tunnel barrier, which we attribute to the adsorption of oxygen from the surrounding atmosphere. This adsorption is favored by the high reactivity of the barrier, which was very weakly oxidized. All the measured tunnel barriers are practically stable if compared to the previously reported increases of 100% up to 400% within the first weeks after the fabrication.

One of the junctions from group A was measured at low temperatures, in

chip	oxidation pressure during fabrication	storage	$\frac{R_N(t) - R_N(0)}{R_N(0)}$
A	$5 \cdot 10^{-2}\,mbar$	4 weeks in vacuum	$< 1\%$
B	$4 \cdot 10^{-2}\,mbar$	4 weeks in air at atm. pressure	$< 1\%$
C	$5 \cdot 10^{-3}\,mbar$	6 weeks in air at atm. pressure	$+10\%$

Table 2.2: Measurement of junction stability in time
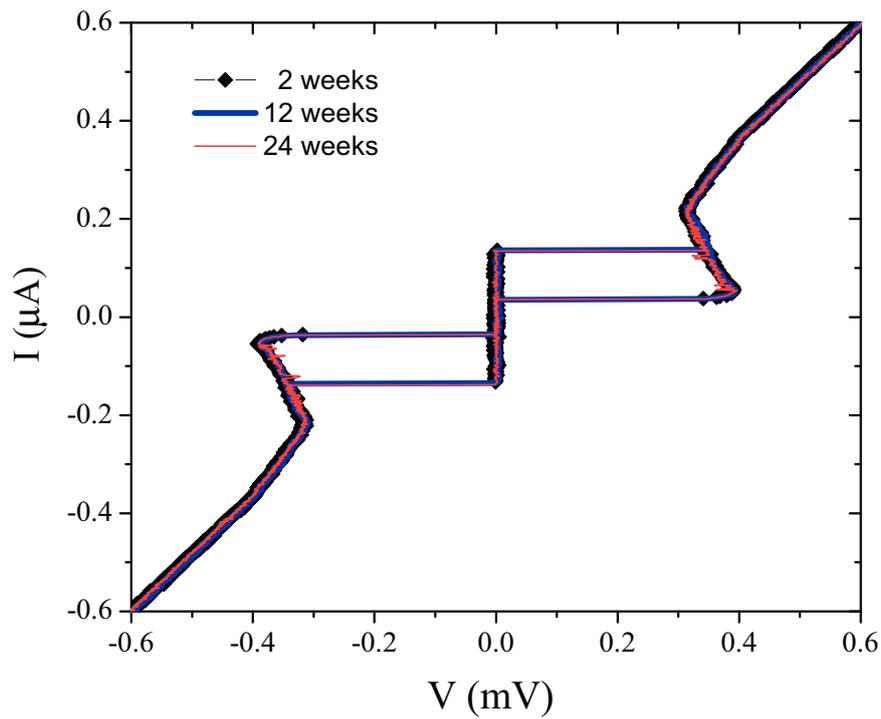
Figure 2.16: Current-voltage curves for the same junction (from group A) measured 2 weeks (in black), 12 weeks (in blue) and 24 weeks (in red) after the fabrication. Between the measurements, the junction was stored at room temperature and atmospheric presure.

the superconducting regime, at 2 weeks, 12 weeks and 24 weeks from the end of the fabrication. The measured IV characteristics are plotted in Fig. 2.16. Notice that the results of the 3 measurements at $T = 50\,\mathrm{mK}$ are practically identical. We did not observe any aging of the the tunnel barrier, the critical current or the retrapping current. Both switching and retrapping currents depend on the junction capacitance C. Thus, we conclude that the capacitance of the junction is also completely stabilized.

We continue our study of the oxide tunnel barrier by measuring the effects of annealing. P. Koppinen et al. [60] show that samples annealed at $200\,^{o}$C, although not completely stabilized, increased their tunnel barrier by $+50\%$. They also report the complete stabilization of the tunnel barriers after annealing at $400\,^{o}$C. The stabilized tunnel barrier is 4 times larger compared to the value measured immediately after the fabrication.

We have measured the effect of thermal cycles on the tunnel barrier of our junctions. The steps of one thermal cycle are the following: 10 minutes heating, 10 minutes regulating the temperature to a constant value and 20 minutes cooling down. In Table 2.3, we report results fundamentally different from Ref. [60], for junctions fabricated using the Ethanol development and the RIE cleaning. For

chip	annealing	$\frac{R_N(t)-R_N(0)}{R_N(0)}$
B	$200\,^{o}C$ in vacuum	$< 1\%$
B	$400\,^{o}C$ in vacuum	-45%
D	$200\,^{o}C$ under $PMMA$ resist	-26%
D	1 week after first anneal	-23%
D	$200\,^{o}C$ under $PMMA$ resist	-28%
D	4 weeks after second anneal	-22%

Table 2.3: Influence of the different annealing on the measured tunnel barrier of the junctions.

sample B, after annealing at $200\,^{o}$C we observe no change in the tunnel barrier resistance. This confirms the stability of our junctions. After annealing at $400\,^{o}$C we observe a decrease of the barrier by almost 50%. This decrease is expected, as the oxygen in the barrier starts to be thermally activated for $T \gtrsim 300\,^{o}$C and it diffuses in the environment [65].

After annealing the junctions of sample D under a $PMMA$ resist layer, we observe a significant decrease of the tunnel barrier (see Table 2.3). This could be explained by the contamination of the junction with hydrates$(-OH)$ from the resist, which combine with the oxide to form hydroxides (for example $Al_2O_3(H_2O)$ or $Al_2O_3 \cdot 3(H_2O)$) and thus decrease the barrier height, as suggested in Ref. [63]. After annealing under the $PMMA$ resist layer, the junctions were unstable and we measured a slow relaxation of the barrier value towards the initial state. In one week, the barrier increased by 3%. After re-annealing the sample covered by the resist in the same conditions, the value of the barrier returns to lower values, as indicated in Table 2.3. After 4 weeks, the barrier relaxes again to a height 6% larger. This reversible annealing-relaxing behavior could be explained by the absorption of

hydrates during the annealing, which would account for the barrier decrease, while the slow desorption of the hydrates would explain the measured relaxation.

We speculate that the aging measured in Ref. [60] can be explained by the slow desorption of hydrates, which can greatly be accelerated by temperature [63]. Indeed, for samples cleaned using the RIE, thus less susceptible to absorb hydrates from the resist, the measured aging in Ref. [60] is two orders of magnitude slower. Moreover, in Ref. [66], similar junctions fabricated without using a resist bilayer, show no aging over one year.

In conclusion, we have fabricated completely stable $Al/AlO_x/Al$ Josephson junctions, which were monitored for as long as 6 months, without observing any changes in the barrier parameters. We believe that the crucial processing step, allowing the fabrication of stable junctions, is the aggressive cleaning of the substrate before the aluminum evaporation. We performed the cleaning in two steps: an Ethanol development step and an optimized, isotropic RIE oxygen-plasma cleaning. We show that the junctions are stable to annealing up to $200\,^oC$. We suggest that the junction aging reported in the literature is associated with the resist contamination in the vicinity of the junction. Our model is sustained by observation of aging on previously stable junctions which have been deliberately contaminated with resist, during annealing under a layer of $PMMA$.

Chapter 3

The phase dynamics of a current biased Josephson junction

In this chapter we will present the general proprieties of the superconducting phase dynamics of a current biased Josephson junction. We will show how to use such a junction as a detector to measure the energy band of an unknown Josephson circuit. Further on, we will describe the measurement protocol and we will discuss the advantages but also the limitations of this detector. Finally, we will present the theoretical methods needed for a quantitative understanding of the measurement results.

3.1   RCSJ model for the Josephson junction

In 1962, Josephson predicted that a zero voltage supercurrent should flow between two superconducting electrodes separated by a thin insulating barrier [6]:

$$I_S = I_C \sin\delta \quad \text{and} \quad \delta = \Delta\varphi - \frac{2\pi}{\Phi_0} \int \overrightarrow{A} \cdot \overrightarrow{dl} \tag{3.1}$$

Here δ is the gauge-invariant superconducting phase difference, which is the sum of two contributions: the difference in the phase of the Ginzburg-Landau wave function in the two electrodes $\Delta\varphi$ and the integral of the vector potential between the electrodes [67]. I_C is the critical current, the maximum supercurrent that the junction can support. The critical current depends on the normal state resistance of the junction R_N, and on the temperature T. This dependence is known as the Ambegaokar-Baratoff relation [68] and for temperatures T much lower than the critical temperature of the superconductor T_C, it reads:

$$I_C = \frac{\pi\Delta}{2e} \frac{1}{R_N} \tag{3.2}$$

We will use the Ambegaokar-Baratoff value given by eq. (3.2) for the critical current of our junctions made of aluminum. All measurements are made at $T = 50\,\text{mK}$, well below $T_C \simeq 1.4\,\text{K}$, therefore the zero temperature limit can be used in good approximation.

The second theoretical prediction of Josephson [6] was the phase evolution for a voltage biased junction:

$$\frac{d\delta}{dt} = \frac{2e}{\hbar}V \tag{3.3}$$

Looking at eq. (3.1) we see that the resulting current for a voltage biased junction is alternating with an amplitude I_C and a frequency $\nu_J = (2e/h)V$. The quantum energy $h\nu_J$ equals the energy needed for a charge $2e$ to cross the junction.

The *DC* and *AC* Josephson effects have been measured in detail since their prediction. Josephson's theoretical work initiated the field of superconducting electronics. By using equations (3.1) and (3.3), we can practically forget about all the complex, microscopic many body phenomena inside the junction. We can design electronic circuits with unique properties using Josephson junctions as a lumped elements with a current-phase relation given by eq. (3.1).

(a)

(b)
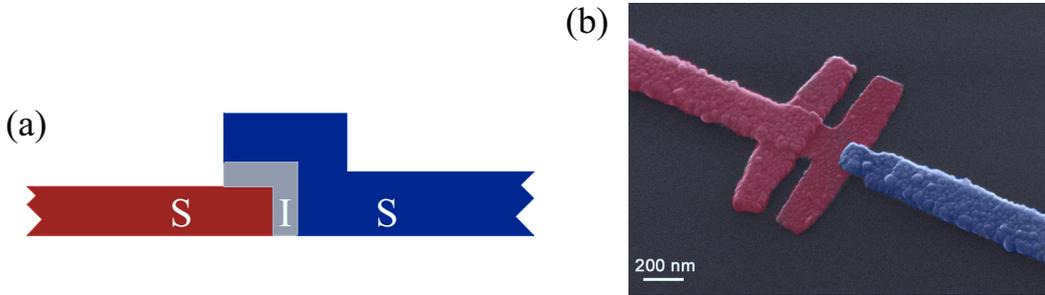
Figure 3.1: (a) Schematic representation of a SIS Josephson junction. (b) e-Beam image of a real $Al/AlO_x/Al$ junction. The two electrodes are highlighted in red and blue for clarity and comparison with (a).

The realisation of a superconductor-insulator-superconductor (SIS) Josephson junction (as schematized in Fig. 3.1), implies a capacitive coupling C between the superconducting electrodes. The characteristic energy asociated to the junction capacitance is the charging energy for one electron: $E_C = \frac{e^2}{2C}$. The effects of the capacitance C are not taken into account in eq. (3.1). Also, the dissipative element R, required for electrical transport at finite voltage, is missing in the simple model described by eq. (3.1). A more complete description of the Josephson junction is required. This is provided by the RCSJ (resistively and capacitively shunted junction) model [67] in which we replace the real junction with an ideal one described by eq. (3.1), shunted by an impedance R and a capacitor C, as represented in Fig. 3.2a. The value of R is given by the impedance at the characteristic frequency of the phase dynamics. For voltages V larger than the value of the superconducting gap or for temperatures close to the critical temperature $T \simeq T_C$, the value of the impedance R is given by the normal state resistance of the junction: $R = R_N$. Experimentally, R_N is determined from the linear part of the measured IV curves, in situ and at low temperatures (see. Fig. 3.3).

Let us analyze in more detail the RCSJ model [69,70]. If we write Kirchhoff's circuit laws for the electrical setup presented in Fig. 3.2a, we obtain the equation of motion for the superconducting phase difference δ :
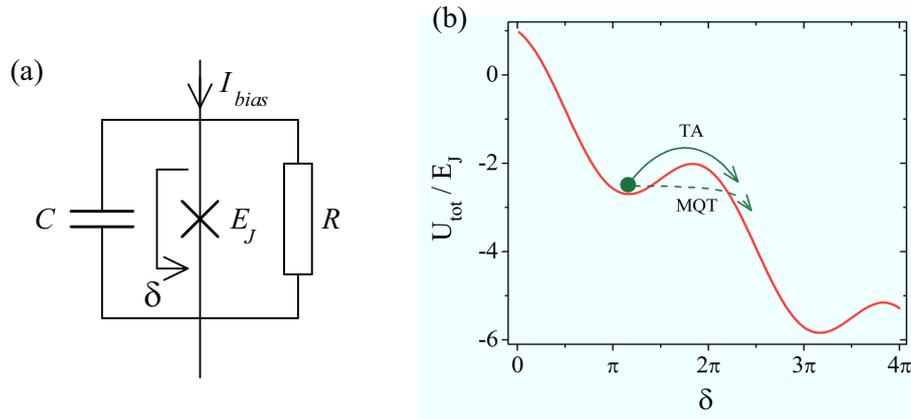
Figure 3.2: RCSJ model for one Josephson junction. (a) Electrical scheme of the RCSJ model. (b) The physics of the system presented in (a) is described by the dynamics of a phase particle in a tilted washboard potential (see eq. 3.5). We usually call this potential the *tilted washboard* potential. The phase particle can escape from the local minimum by thermal activation (TA) or by macroscopic quantum tunneling (MQT).
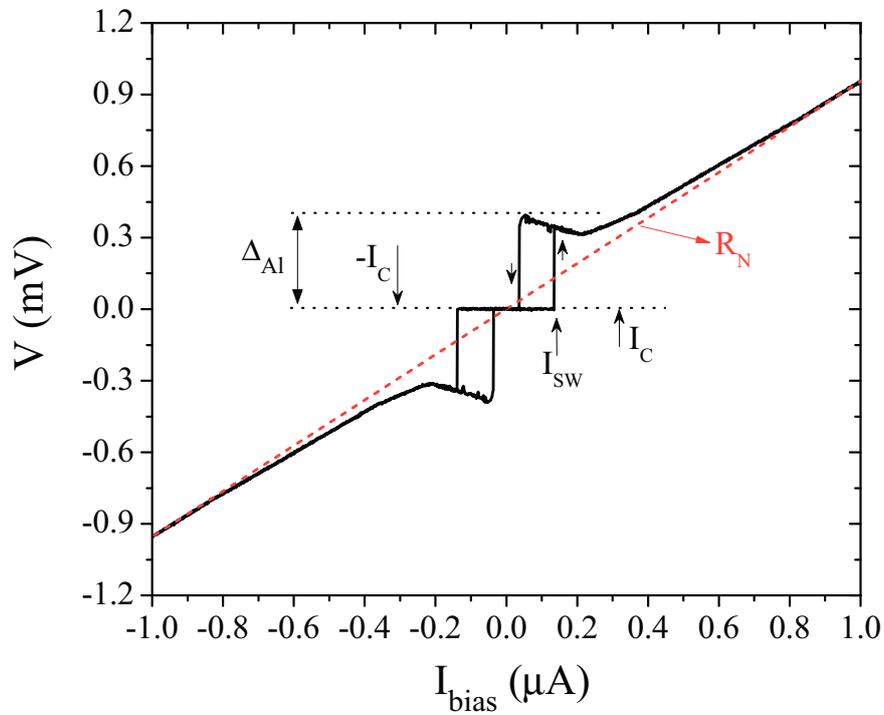
Figure 3.3: Measured current-voltage characteristic for a Josephson junction.

$$C \left(\frac{\phi_0}{2\pi} \right)^2 \ddot{\delta} + \frac{1}{R} \left(\frac{\phi_0}{2\pi} \right)^2 \dot{\delta} + \frac{\partial U_{tot}(\delta)}{\partial \delta} = 0 \tag{3.4}$$

where:

$$U_{tot}(\delta) = -E_J \left(\cos \delta + \frac{I_{bias}}{I_C} \delta \right) \tag{3.5}$$

Here $E_J = \phi_0 I_C / (2\pi)$ is the Josephson energy of the junction. Equation eq. (3.4) describes the motion of a phase particle with mass $C \left(\frac{\phi_0}{2\pi} \right)^2$, in the *tilted washboard* potential $U_{tot}(\delta)$ (see eq. (3.5) and Fig. 3.2b). The damping is given by the viscous force $\frac{1}{R} \left(\frac{\phi_0}{2\pi} \right)^2 \dot{\delta}$. The circuit is in the dissipation-less state ($V = 0$) as long as the phase particle is trapped inside one of the minima of the washboard. As soon as it escapes from the local minima, it will start to roll down the washboard in an accelerated motion. The phase particle will reach a constant speed when the friction force compensates the tilt of the washboard. The running state of the system is characterized by non zero phase dynamics $\dot{\delta} \neq 0$, thus we expect to measure a voltage drop on the circuit, according to the second Josephson relation (3.3).

The frequency of the small superconducting phase oscillations in the vicinity of one local minimum of the washboard potential (3.5) is called the plasma frequency. It reads:

$$\omega_0 = \frac{1}{\hbar} \sqrt{8 E_J E_C} \tag{3.6}$$

The quality factor Q quantifies the energy loss, due to the viscous force in eq. (3.4), during one phase oscillation at the plasma frequency. It reads:

$$Q = \omega_0 R C \tag{3.7}$$

If the viscous force in in eq. (3.4) is small, the junction is under-damped and $Q > 1$. If the viscous dissipation is important, the junction is over-damped and $Q < 1$.

The washboard model for the RCSJ circuit can explain quantitatively the main features of the measured IV curve presented in Fig. 3.3. Close to zero current bias the phase particle is trapped in one of the minima of the washboard and the voltage is zero. If we tilt the washboard sufficiently, by increasing I_{bias}, at a current I_{SW}, the phase particle escapes into the running state and we measure a voltage V. If the friction force is small, the junction is in the under-damped regime ($Q > 1$), and immediately after the escape, the voltage jumps from zero to a value close to the value of the superconducting gap (see Fig. 3.3). Since we get a very non linear response of the junction as a function of the applied current, in the following section (section 3.2) we will show that under-damped JJ can be used as detectors for the measurement of the supercurrent in various junction devices. If we further increase the current, above the value of the gap, we follow a linear IV relation (see dotted line in Fig. 3.3) which gives the value of the normal state resistance of the junction R_N. When we decrease the current, we increase the depth of the local minima and we decrease the slope of the washboard. For $Q > 1$, inertia preserves the running state of the phase particle for currents inferior to the switching current I_{SW}. At a

sufficiently low current I_R the phase particle is re-trapped into the local minima of the washboard and the voltage V drops to zero.

In Fig. 3.3 we represented the critical current I_C and the switching current I_{SW} for the measured junction. Notice that I_{SW} is significantly smaller than I_C. This is because the phase particle can escape from the washboard local minimum, before the minimum vanishes completely at $I_{bias} = I_C$. As represented in Fig. 3.2b, the escape can occur either by thermal activation (TA) over the barrier or by macroscopic quantum tunneling (MQT) through the barrier. In either case, the escape to the running state is a stochastic event. In order to precisely characterize the escape process, we need to measure the statistics of the switching currents as a function of the current bias.
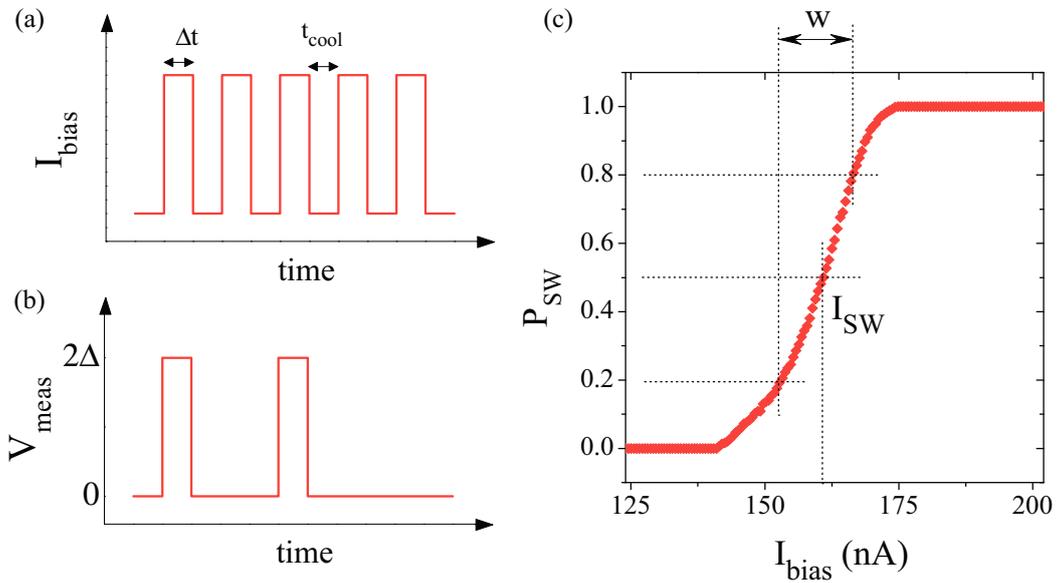
Figure 3.4: Measuring procedure for I_{SW}. (a) We apply current steps of equal amplitude. (b) We count the number of transitions to the voltage state. (c) Measured switching histogram. The measured IV curve for the same junction is presented in Fig. 3.3.

The switching current I_{SW} of the junction is obtained by carrying out the following sequence (see Fig. 3.4). We use a series of M current steps of equal amplitude I_{bias} to bias the junction (Fig. 3.4a). We count the number M_{SW} of transitions to the voltage state (Fig. 3.4b) and thus obtain the value of the switching probability $P_{SW} = M_{SW}/M$ corresponding to the applied I_{bias}. By sweeping the I_{bias} amplitude and repeating the above sequence, we measure a complete switching histogram, P_{SW} versus I_{bias} (Fig. 3.4c). The $P_{SW} = 50\%$ bias current is called the switching current of the circuit, I_{SW}. The current difference between the value at $P_{SW} = 80\%$ and the value at $P_{SW} = 20\%$ is called the histogram width w. Notice that the measured switching histogram is approximately linear between the 20% and 80% values.

3.2 Using a Josephson junction to build a current detector

In this section we discuss theoretically the electrical scheme that we have used to test the energy versus phase relation $E(\gamma)$ of different Josephson junction circuits. The scheme of the readout device is presented in Fig. 3.5. The Josephson junction circuit that we want to measure is inserted in a superconducting loop containing a large read-out JJ. The magnetic flux Φ_C through the loop tunes the phase bias γ (see Fig. 3.5). The critical current of the read-out junction I_C should be much larger than the one of the studied JJ circuit i_C. The condition $I_C \gg i_C$ minimizes the back-action of the detector on the measured signal (see section 3.3).
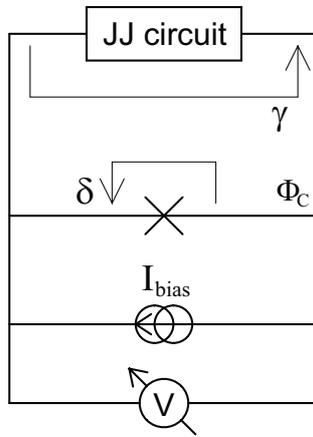
Figure 3.5: Detection scheme for the measurement of the ground state of a Josephson junction (JJ) circuit. We denote the phase over the read-out junction δ and the phase bias for the JJ circuit γ.

We measure the total switching current I_{SW} of the superconducting circuit in Fig. 3.5 using the sequence detailed in the previous section and also presented in Fig. 3.4. The Φ_C dependence of the switching current $I_{SW}(\Phi_C)$ contains the information about the current-phase relation of the studied Josephson junction circuit. In a first order approximation, the oscillations of the switching current $I_{SW}(\Phi_C)$ can be directly associated to the current-phase relation of the studied Josephson junction circuit. However, for an exact quantitative understanding of the measurements, we need to study in detail the escape of the phase particle from the washboard of the total circuit in Fig. 3.5 (read-out junction plus JJ circuit). As we will show in the next section (see chapter 3.3), the corrections to the first order approximation can be significant.

The principle of the read-out scheme was first implemented by D. Vion et al. [26] and has since been used for the measurement of different superconducting circuits: an asymmetric Cooper pair transistor [71], quBits [14, 72], atomic contacts [73] or complex Josephson junction networks [40]. Recently, hysteretic Josephson junctions have also been proposed as detectors for studying phenomena like non-Gaussian noise [74–76].
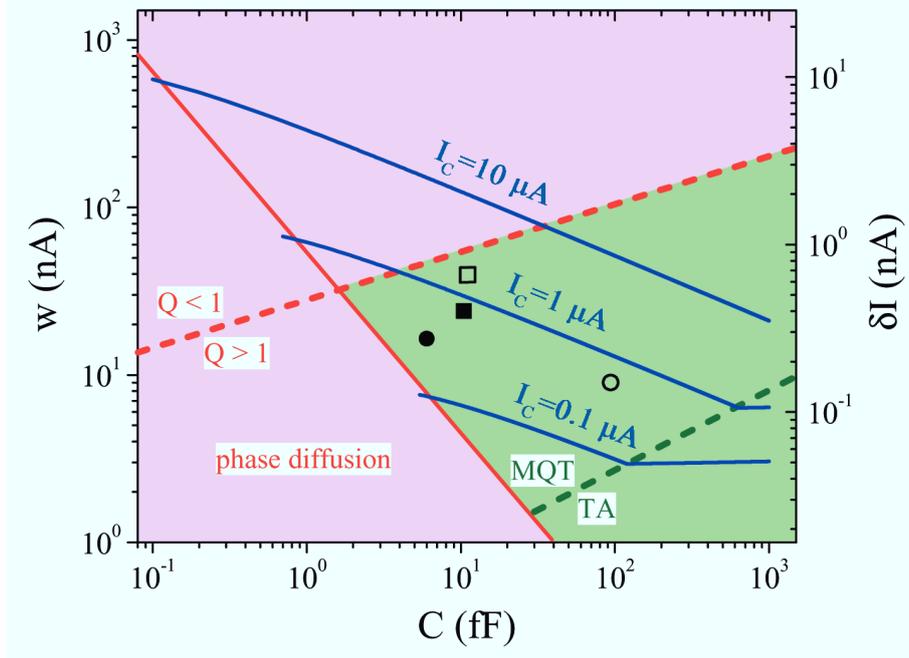
Point Symbol	Measured JJ circuit and its critical current: i_C	Read-out junction: I_C	Ref. Chapter
●	6 junctions chain; $i_C < 35\,nA$	$330\,nA$	5
○	12 rhombi network; $i_C < 150\,nA$	$400\,nA$	4.2.2
■	quantum 8 rhombi chain; $i_C < 5\,nA$	$740\,nA$	4.4
□	classical 8 rhombi chain; $i_C < 40\,nA$	$2100\,nA$	4.2.1

Figure 3.6: (blue lines) Plot of the calculated width w of the histograms as a function of the capacitance of the junction C, for three different critical currents I_C. The regions where the escape occurs via tunnel effect or thermal activation are denoted by MQT and TA respectively. The green regions highlight the parameter space where the junction is efficient as a detector. The four particular points (full and empty black circles and squares) show the actual parameters of the different read-out junctions we have used for the measurements presented in the following chapters. In the above table we show a list of the corresponding critical currents of the read-out junction and of the measured JJ circuit.

Let us now discuss the signal to noise ratio for this type of detector. The noise associated to the escape probability measurement originates from statistical fluctuations of the P_{SW} values, due to the finite number of current bias steps M. The value of the measured P_{SW} is given by the binomial distribution. The variance of the switching probability σ_P is given by: $\sigma_P = \sqrt{\frac{P_{SW}(1-P_{Sw})}{M}}$. The optimal bias point for the junction is around $P_{SW} = 50\%$ as the slope of the histogram is maximal and so is the sensitivity to the bias current. Typically we apply $M = 10^4$ current steps. The corresponding variance for the switching probability is $\sigma_P = 0.5\%$.

The resulting noise δI of the current measurement depends on σ_P but also on the width w of the histograms:

$$\delta I = \frac{w}{60}\,\sigma_P \qquad (3.8)$$

The factor 60 in the δI formula comes from the definition of the histogram width as the difference between the current levels at 80% and 20%.

At the base temperature $T = 50\,\mathrm{mK}$, the read-out junction can switch to the running state either by thermal activation (TA) [77–79] or by tunnel effect (MQT) [10, 80]. In Fig. 3.6 we plot (in blue lines) the calculated width of the histograms w and the resulting statistical current noise δI for the typical value $M = 10^4$, as a function of the capacitance C of the junction, for three different critical currents I_C. The green highlighted areas show the junction parameter space where it can be used efficiently as a current detector. Fig. 3.6 also presents the position of the read-out junctions we have used to perform our measurements. The red highlighted regions mark the over-damped ($Q < 1$) or phase diffusion regimes. Within these regions the junction cannot be used efficiently as a current detector in the electrical scheme of Fig. 3.5. The phase diffusion boundry is represented by the continous red diagonal line in Fig. 3.6 and it is given by the condition $w = I_{SW}$. In other words, in this region the phase δ becomes delocalised, because even at very low bias current, the fluctuations are strong enough to induce the escape of the phase-particle from the local minimum.

Figure 3.6 shows that the current noise due to statistical fluctuations δI decreases with the critical current I_C of the read-out junction. But I_C cannot be arbitrary small. It must remain significantly larger than the critical current i_C of the studied JJ circuit: $I_C \gg i_C$. From figure 3.6 we infer a typical ratio $I_C/\delta I$ between 10^3 and 10^4. Thus, if the ratio $I_C/i_C \gtrsim 10$, the signal to noise ratio $i_C/\delta I$ is in the interval $100 \rightarrow 1000$.

As we can see from Fig. 3.6, all the read-out junctions that we have used in our experiments, are in the MQT escape region. In the following chapter we will analyze in detail the MQT escape from the total washboard potential, given by the read-out junction potential plus the contribution from the measured JJ circuit (see Fig. 3.5). The detailed understanding of the MQT switching to the dissipative state is essential for a quantitative understanding of the measured switching curves $I_{SW}(\Phi_C)$.

3.3 MQT escape from an arbitrary shaped wash-board potential

The measured switching current of the circuit in Fig. 3.5 corresponds to the escape process out of the total potential energy U_{tot} containing the contributions of the read-out junction and the JJ circuit:

$$U_{tot}(\delta, \Phi_C) = E_J \cos(\delta) + E_g(\Phi_C - \delta) - \frac{\hbar}{2e} I_{bias}\delta. \qquad (3.9)$$

Here E_g is the ground state of the studied JJ circuit. As $E_J \gg E_g$, the main component in U_{tot} is the potential of the current-biased read-out junction $E_J \cos(\delta) - \frac{\hbar}{2e} I_{bias}\delta$ (which is the same as eq. (3.5)). In Fig. 3.7 we show for exemplification the calculated escape potentials at constant bias-current for three different flux values Φ_C corresponding to three different biasing phases γ over a chain of 6 Josephson junctions (see the point ● in Fig. 3.6 and also chapter 5). Let us point out that the position of the minimum of the potential U_{tot} is to a good approximation independent of the value of the flux Φ_C. Therefore the bias phase difference γ over the chain depends only on the flux Φ_C and the backaction of the detector on the measured system is neglectable. The three plots in Fig. 3.7 show how the ground state of the JJ circuit, which changes as a function of the phase bias, modulates the shape of the total washboard potential U_{tot}. The MQT switching rate is very sensitive to these changes. As a consequence, the Φ_C dependence of the measured switching current results from the γ dependence of the JJ circuit ground state.

For all our studied circuits, the escape from the total potential (3.9) occurs via macroscopic quantum tunneling (MQT) (Fig. 3.6). Deppending on the shape of the energy-phase relation for the measured JJ circuit, standard MQT calculations [80,81] might not give sufficiently accurate results, if the potential $U_{tot}(\delta)$ can not be well approximated by a polynomial series expansion. The MQT rate for an arbitrary potential was calculated in the thesis of N. Didier [82] in the limit of weak tunneling using the dilute instanton-gas approximation [83]. Within this model, the escape rate Γ out of the washboard potential $U_{tot}(\gamma)$ reads:

$$\Gamma = A \exp\left[-B\right] \qquad (3.10)$$

Where the coeficients A and B are given by:

$$A = \sqrt{\frac{\hbar \omega_p^3}{8\pi E_C}} \sigma\, e^I \quad \text{with} \quad I = \int_0^\sigma \left[\sqrt{\frac{\hbar^2 \omega_p^2}{16 E_C U_{tot}(x)}} - \frac{1}{x}\right] dx \qquad (3.11)$$

and

$$B = 2 \int_0^\sigma \sqrt{\frac{\hbar^2 U_{tot}(x)}{4 E_C}} dx \qquad (3.12)$$

We have denoted by σ the width of the barrier and by x the phase coordinate measured from the minimum of the washboard potential (see Fig. 3.7). The plasma
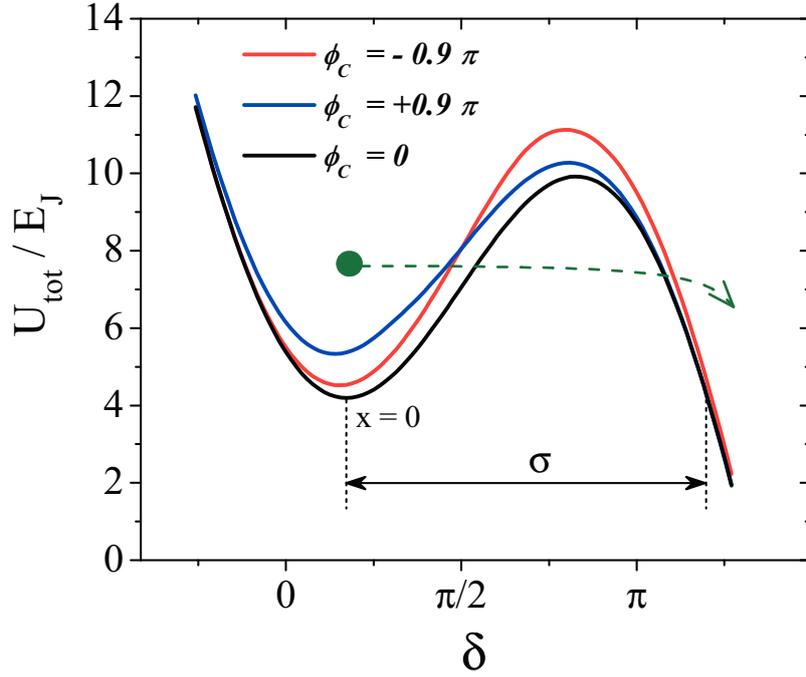
Figure 3.7: Escape potentials for the read-out junction in parallel with the JJ circuit, for three different flux biases Φ_C in the read-out loop (see Fig. 3.5). The ground state of the JJ circuit, which deppends on Φ_C, clearly modifies the shape of the escape potential.

frequency ω_p corresponds to the small phase oscilations arround the local minimum of U_{tot}:

$$\omega_p = \sqrt{\frac{8E_C}{\hbar} \left. \frac{d^2 U_{tot}(x)}{dx^2}\right|_{x=0}} \tag{3.13}$$

where E_C is the charging energy of the read-out junction.

Knowing the escape rate Γ, we can calculate the switching probability as a function of the current bias I_{bias} and the length of the current pulse Δt:

$$P_{SW}(I_{bias}) = 1 - \exp\left[-\Gamma(I_{bias})\Delta t\right] \tag{3.14}$$

Using eq. (3.14) we can numerically calculate the switching curves from the local minimum of an arbitrarely shaped potential. In chapter 6 we present a detailed comparison between these calculations and the measured switching histograms. We otain a good agreement. In chapter. 5 we use this technique to understand quantitatively the measurements of quantum-phase slips in a 6 junction chain.

Chapter 4

Measurement of the ground state of Josephson junction rhombi chains

Arrays of small Josephson junctions are fascinating systems, as they exhibit a wide variety of quantum states controlled by lattice geometry and magnetic frustration [84]. A particularly interesting situation occurs in systems with highly degenerate classical ground states where non trivial quantum states have been proposed in the search for topologically protected qubit states [37]. The building block for such a system is a rhombus with 4 Josephson junctions (fig. 4.1b) and the simplest system is the linear chain of rhombi (fig. 4.1a) as proposed by Douçot and Vidal [85] along the line of the so-called Aharonov-Bohm cages [86]. The main consequence of the existence of the Aharonov-Bohm cages in the rhombi array is the destruction of the $(2e)$-supercurrent when the transverse magnetic flux through one rhombus is exactly half a superconducting flux quantum. This destructive interference is reminiscent of the localization effect predicted for non interacting charges in [86] and observed experimentally in both superconducting [87] and normal networks [88]. Interestingly, in a rhombi chain made of small capacitance junctions, it was predicted that a finite supercurrent carried by correlated pairs of Cooper pairs, carrying a charge of $4e$, will subsist at full frustration ($\Phi_R = \Phi_0/2$) [85], while the ordinary $2e$ supercurrent dissappears.

I. Protopopov and M. Feigelman [89, 90] have studied the equilibrium supercurrent in frustrated rhombi chains. They have made quantitative predictions for the magnitude of both, the $2e$ and the $4e$ supercurrents, as a function of the relevant parameters : magnetic flux, ratio of Josephson to Coulomb energy, chain length and quenched disorder. The ratio between the Josephson energy $E_J = i_c \frac{\hbar}{2e}$ and the charging energy $E_C = \frac{e^2}{2C}$ of the junctions determines whether the chain is in the classical or in the quantum regime.

As we will show in detail further on, we observed the doubling of the current-phase periodicity, which is a signature of coherent transport of pairs of Cooper pairs ($4e$ supercurrents), in two types of small size rhombi arrays. The junctions forming the arrays are in the classical regime ($E_J \gg E_C$) [91]. In parallel, in the Rutgers University experimental group, S. Gladchenko *et al.* observed the transport of pairs
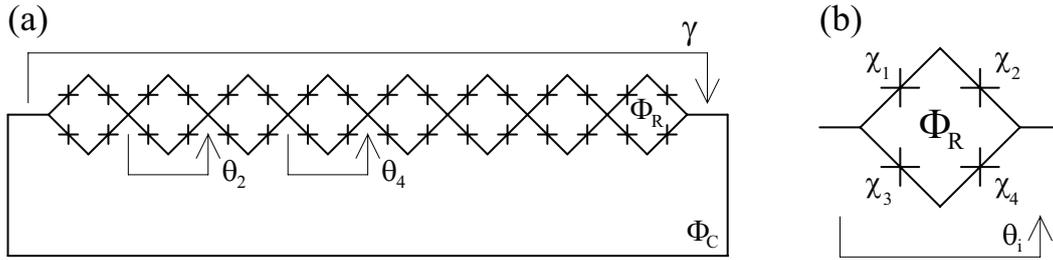
Figure 4.1: The different notations used in the text for the rhombi chain (a) and for one rhombus (b). Each cross represents a Josephson junction. The lines represent superconducting wires and the arrows represent gage invariant phase differences. The magnetic flux Φ_C inside the superconducting ring containing the rhombi chain fixes the phase difference across the chain to $\gamma = 2\pi\Phi_c/\Phi_0$. The phase differences over each of the four junctions in one rhombus are denoted by χ_n where $n = 1, 2, 3, 4$. The gauge-invariant phase θ_i will be referred to as the diagonal phase difference. Φ_R represents the magnetic flux inside one rhombus and the frustration parameter of the rhombus is given by $f = \Phi_R/\Phi_0$.

of Cooper pairs in a rhombi array in the quantum regime ($E_J \gtrsim E_C$) [40]. In the last section of this chapter we present the observation of quantum phase-slips in a rhombi chain [91].

4.1 Classical rhombi chains

In this section we present the theory describing the states and the energy bands for a rhombi chain in the classical phase limit, where the amplitude of the QPS can be neglected ($E_J \gg E_C$). This theory is used later to understand the measurements of the current phase relation of classical chains.

We are interested in the current phase relation $I_S(\gamma)$ of a rhombi chain for different rhombus frustrations $f = \Phi_r/\Phi_0$. Φ_r represents the magnetic flux inside one rhombus and $\Phi_0 = \frac{h}{2e}$ is the superconducting flux quantum. The phase difference γ over the chain is fixed by introducing the rhombi chain into a superconducting loop threaded by a magnetic flux $\Phi_c = \Phi_0\gamma/2\pi$. The Josephson junctions circuit and the notations that we will further refer to are represented in Fig. 4.1.

In the following we discuss the case where charging effects are negligible, and therefore the superconducting phase is a classical variable. The effects of non zero charging energy are discussed in section 4.3. The classical states of one rhombus which depend on the diagonal phase difference θ and on the frustration f are introduced in section 4.1.1. In section 4.1.2 we extend the classical description of the energy states to a chain containing N rhombi. In this case the energy band depends again on the frustration f and the phase difference γ over the whole chain.
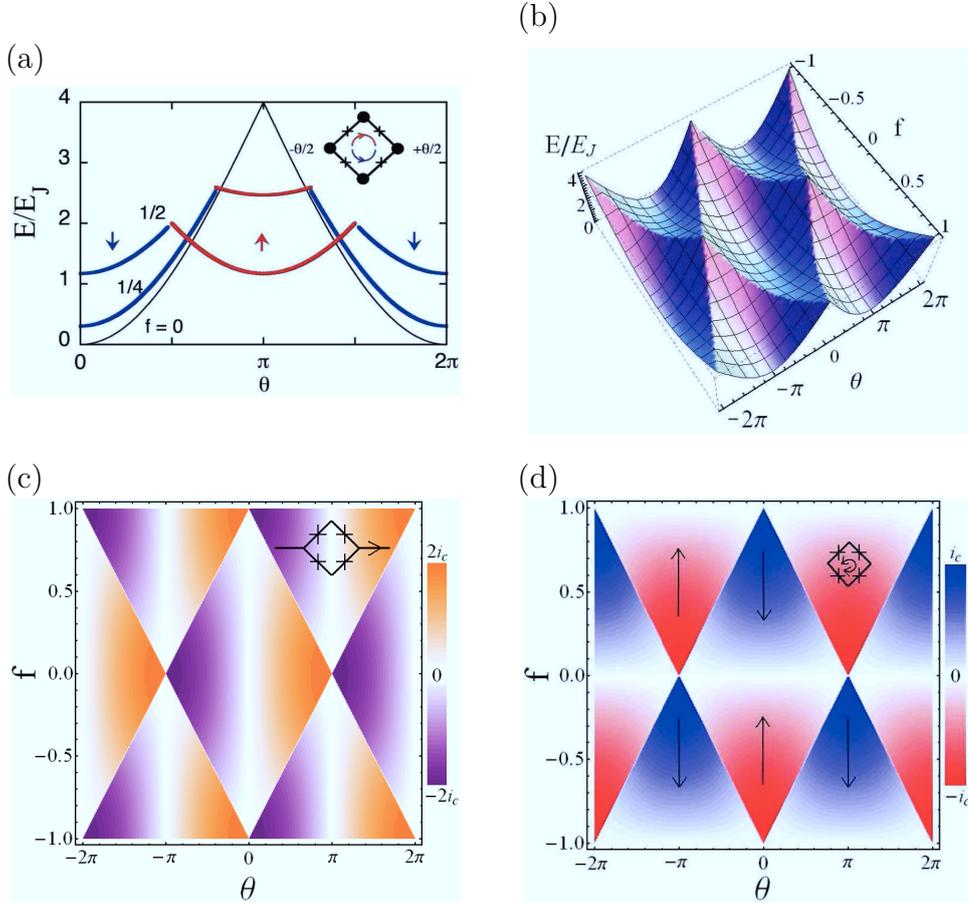
Figure 4.2: Classical states of a single rhombus. a) The ground state energy as a function of the diagonal phase difference θ over the rhombus for three different frustrations $f = 0$, $1/4$ and $1/2$. The inset shows the two possible persistent current states: a clockwise flowing supercurrent (blue lines) and a counterclockwise supercurrent (red line). b) 3D plot showing the lowest energy band as a function of θ and f. c) Two dimensional plot for the supercurrent across one rhombus. The amplitude and sign of the supercurrent is illustrated by the background color: orange (positive values) for currents flowing from left to right and violet (negative values) for currents from right to left. d) Two dimensional plot for the amplitude and the direction of the persistent current around the ring. The clockwise current states, denoted $|\downarrow\rangle$, are represented in blue, the counterclockwise current states, denoted $|\uparrow\rangle$, in red. At full frustration ($f = 0.5$) the ground state is degenerate for $\theta = \pm\pi/2$, and the two eigenstates differ by the sign of the persistent current.

4.1.1 Single Rhombus

We consider a single rhombus made of 4 identical Josephson junctions (Fig. 4.1b). The single junction Josephson energy is E_J and its critical current $i_c = \frac{2e}{\hbar} E_J$. Neglecting additional terms due to wire inductances, the potential energy of one rhombus containing four identical junctions, is simply given by the sum of the Josephson energies of the four junctions:

$$E(\chi_1, \chi_2, \chi_3, \chi_4) = \sum_{n=1}^{4} E_J(1 - \cos \chi_n) \tag{4.1}$$

We can safely neglect wire inductances as the rhombi loops are small, thus the corresponding geometric and kinetic inductances are orders of magnitude smaller than the Josephson inductance of the junctions. The sum of the phases χ_n is fixed by the flux inside the rhombus:

$$\sum \chi_n = 2\pi f \tag{4.2}$$

For simplicity we consider for the moment the ideal case where all junctions are identical and we neglect any coupling of the islands to the ground. The current flowing through each branch of the rhombus induces the same phase difference on both junctions: $\chi_1 = \chi_2$ and $\chi_3 = \chi_4$. Using the notations defined earlier, the ground state energy of one rhombus, in the classical regime ($E_J \gg E_C$), is found by minimizing the energy (4.1) and depends only on the parameters θ and f:

$$E(\theta, f)/E_J = 4 - 2(|\cos(\theta/2 + \pi f/2)| + |\cos(\theta/2 - \pi f/2)|) \tag{4.3}$$

A complete description of the phase diagram for one rhombus is given in Fig. 4.2. The circular current in the superconducting ring is $i_p(\theta, f) = \frac{2e}{\hbar} \frac{\partial E(\theta, f)}{\partial f}$ and it is 2π-periodic in θ and f (Fig. 4.2d). The supercurrent through one rhombus is given by $i_s(\theta, f) = \frac{2e}{\hbar} \frac{\partial E(\theta, f)}{\partial \theta}$ and it is shown in Fig. 4.2c.

The interesting feature about this system is the change from 2π to π periodicity as a function of the bias phase θ over the rhombus when the frustration f changes from 0 to 1/2. This property does not exist in the case of a dc SQUID, as there is no modulation of the energy as a function of θ at full frustration. At $f = 1/2$ the rhombus has two classical ground states, $\theta = 0$, $\pi \pmod{2\pi}$, denoted in analogy to the z-projection of the spin $\frac{1}{2}$ by $|\downarrow\rangle$ and $|\uparrow\rangle$ respectively. These two states have the same energy $E(\theta = 0, f = 0.5) = E(\theta = \pi, f = 0.5) = 2(2 - \sqrt{2})E_J$ but opposite persistent currents (see Fig. 4.2d). In the case of a current biased rhombus, the phase θ is controlled via the current phase relation of a single rhombus $i_s(\theta, f) = \frac{2e}{\hbar} \frac{\partial E(\theta, f)}{\partial \theta}$ by the external current. The critical current of a single rhombus is given by the maximum supercurrent through the rhombus for a given frustration f: $I_c = \max(i_s(\theta))_{f=const} = \max(\frac{2e}{\hbar} \frac{\partial E(\theta, f)}{\partial \theta})_{f=const}$. It is periodic in f and varies from a maximum of $2i_c$ down to i_c. For $-1/2 \leq f \leq 1/2$ it reads :

$$I_c = 2i_c \cos^2 \frac{\pi f}{2} \tag{4.4}$$

Notice that unlike in a SQUID, exactly at full frustration, the critical current is not completely suppressed, but it is equal to the critical current of one junction in the rhombus. This is an essential feature that will enable the formation of the $4e$ superconducting state inside a chain of rhombi.

4.1.2 Rhombi chain
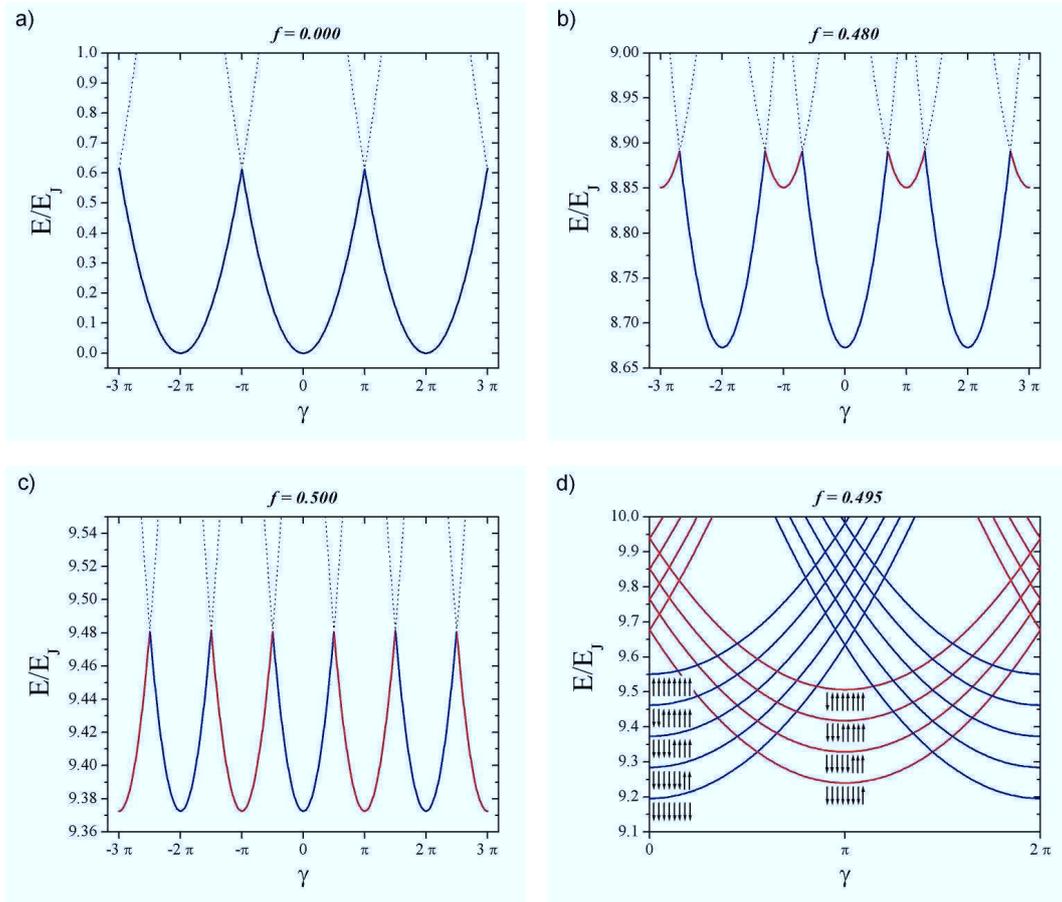
Figure 4.3: a) Ground state energy of a classical 8 rhombi chain as a function of the phase γ, for zero (a), intermediate (b) and full frustration (c). The plot colors correspond to the $|\downarrow\rangle$ state (blue) and $|\uparrow\rangle$ state (red). The supercurrent flowing through the chain is given by the derivative of the energy as a function of γ and consists of a series of unequal sawtooth in the vicinity of $f = 1/2$. d) Identification of the lowest energy states of the chain near full frustration ($f = 0.495$). The up and down arrows indicate the spin states of the 8 rhombi. Note the change in the parity for the number of switched rhombi between successive minima.

In order to understand the classical states of the chain we can start our analysis with the case where each rhombus has a well defined diagonal phase difference across it. For a closed chain of N identical rhombi, the sum of all the diagonal phase differences θ_n is fixed by the magnetic flux Φ_c to a total phase difference γ over the chain (see Fig. 4.1a).

$$\sum_{n=1}^{N} \theta_n = \gamma \tag{4.5}$$

In the region where the frustration, $0 \leq f \ll 1$, is small we obtain by minimizing the total energy that the diagonal phase differences over each rhombus

are identical up to a constant multiple of 2π. The phase difference across the diagonal of the n-th rhombus in the state $|m\rangle$ is given by:

$$\theta_n = \frac{\gamma - 2\pi m}{N} + 2\pi m_n \quad, \quad m = \sum_n m_n \tag{4.6}$$

where m is the number of vortices inside the superconducting loop that contains the rhombi chain, and m_n is an integer corresponding to the number of vortices that crossed the n-th rhombus. Therefore the ground energy of the chain is N times the energy of a single rhombus:

$$\frac{E(\gamma, f)}{E_J} = N \cdot \left[4 - 2 \left(\left| \cos \left(\frac{\gamma - 2\pi m}{2N} + \frac{\pi f}{2} \right) \right| + \left| \cos \left(\frac{\gamma - 2\pi m}{2N} - \frac{\pi f}{2} \right) \right| \right) \right] \tag{4.7}$$

At $f = 0$ and in the limit $N >> 1$ the expression above can be developed around zero. The energies of the low-lying states are given by:

$$E_m(\gamma) = \frac{E_J}{2N} (\gamma - 2\pi m)^2 \tag{4.8}$$

The ground state energy consists of a series of shifted arcs, with period 2π as shown in Fig. 4.3a. In analogy to a single rhombus, at small frustration all rhombi of the chain are in the $|\downarrow\rangle$ state (see Fig. 4.2). The supercurrent through the chain is given by the derivative of the ground state energy with respect to γ, $I_S(\gamma, f) = \frac{2e}{\hbar} \frac{\partial E(\gamma, f)}{\partial \gamma}$. Therefore the current-phase relation of an unfrustrated chain, in the classical regime, is a 2π-periodic sawtooth function as for a single rhombus. But in contrast to a single rhombus the critical current of a chain with large N is approximately N times smaller than the critical current of a single junction. The value for the critical current of the chain $i_c \frac{\pi}{N}$ can be easily calculated from the energy expansion (4.8).

As f approaches $1/2$, the total energy can be reduced by flipping the spin state of one rhombus. The chain with $N-1$ rhombi in the $|\downarrow\rangle$ state and one rhombus in the $|\uparrow\rangle$ state becomes energetically more favorable near $\gamma = \pi \pmod{2\pi}$ as shown in Fig. 4.3a. Thus the energy diagram consists of an alternate sequence of arcs, centered respectively at even and odd multiples of π. At full frustration $f = 1/2$, the period as a function of γ turns to π (see Fig. 4.3a upper trace). Here, the energy modulation $\frac{\pi^2}{8N\sqrt{2}} E_J$ and the maximum supercurrent $I_s = i_c \frac{\pi}{2\sqrt{2}N}$ are significantly weaker than at zero frustration. The crossover point between these two regimes is defined as the minimum frustration that induces at $\gamma = \pi$ a flip from the $|\downarrow\rangle$ state to the $|\uparrow\rangle$ state for one single rhombus in the chain. In Fig. 4.3b we represented the state of the system for f slightly larger than the crossover frustration. For large N the width of the frustration window scales with $1/N$ and can be approximated by the condition :

$$1 - \tan \frac{\pi f}{2} < \frac{\pi^2}{8N} \tag{4.9}$$

Within this window, the supercurrent is expected to show a complex sawtooth variation as a function of the phase γ with unequal current steps. It is interesting to discuss in more details the structure of the chain states in the vicinity of

the full frustration region. In [89] it has been shown that near $f = 0.5$ the energy of the different possible chain states can be approximated by the formula:

$$E_{m,S^z}(\gamma) \approx \frac{E_J\sqrt{2}}{4N}(\gamma + N\pi/2 + \pi S^z - 2\pi m)^2 - \sqrt{2}\delta S^z E_J + const \qquad (4.10)$$

where $\delta = 2\pi f - \pi$. Here $S^z = -\frac{1}{2}\sum \text{sign}(\sin(\theta_n))$ corresponds to the z-projection of the total spin S describing the whole rhombi chain. Figure 4.3d shows the energy diagram for the lowest energy chain states with N=8 in order to highlight the topological distinctions between branches with minimas at even and odd values of γ/π. Near $\gamma = 0$ the ground state is obtained when all the rhombi are in the $|\downarrow\rangle$ state. Near the next minimum, one rhombus has flipped into the $|\uparrow\rangle$ state. For the higher energy levels one can conclude in general that at even values of γ/π, chain states containing an even number of rhombi in the $|\uparrow\rangle$ state (so called even states) show a minimum. At odd values of γ/π chain states with an odd number of rhombi in the $|\uparrow\rangle$ state (so called odd states) show a minimum. At full frustration $f = 1/2$ all chain states with an even and odd number of flipped rhombi become respectively degenerate. Complete degeneracy is achieved at full frustration at $\gamma = \pi/2$: even and odd states have the same energy.

In conclusion, the current phase relation of the rhombi chain in the classical regime should follow a sawtooth like function with a slowly varying amplitude as a function of the frustration except for a small region around $f = 0.5$. Inside this so called frustration window the periodicity of the sawtooth should be half and its amplitude should drop by a factor of $2\sqrt{2}$. In the next section, we present measurements that precisely confirm these predictions.

4.2 Measurement of the current-phase relation of classical rhombi chains

We have experimentally characterized two types of rhombi network designs. The first design is a 1D chain of 8 rhombi. The aim of the experiment was to observe the doubling of the current-phase periodicity around half flux quantum frustration. The second type of device, which was fabricated in the experimental group of Michael Gershenson at Rutgers University, is a network formed of three rhombi chains in parallel, that is supposed to realise a quantum bit (quBit). In the following we will describe in detail the measurement of each of these devices.

4.2.1 Current-phase relation of an 8 rhombi chain

In order to measure the current-phase relation, we introduced the rhombi chain in a closed superconducting loop which contains an additional shunt Josephson junction as shown in Fig.4.4. We have measured the switching current of this circuit. The switching current was obtained from the switching histogram. We fixed the threshold voltage at about one third of the shunt junction gap voltage. The histograms were accumulated at a rate 10 kHz using a fast trigger circuit. The bias current was
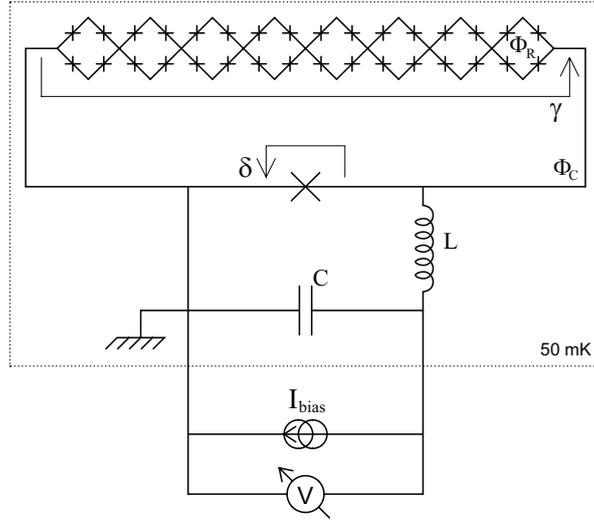
Figure 4.4: Schematic of the circuit for the measurement of the current phase relation in a rhombi chain. The chain is closed by a superconducting line interrupted by an additional Josephson junction referred to as the "read-out junction". An external magnetic field B allows the control of both the rhombi frustration f and the total phase of the closed chain γ.

automatically reset to zero immediately after each switching event. The switching current I_{SW} corresponds, in our definition, to an escape probability of 50%.

The critical current of the shunt read-out junction has a large value $I_0^{RO} = 2.5\mu$A, much larger than the critical current of the chain which is smaller than 50 nA. Near the switching event the phase difference over the read-out junction is close to $\pi/2$. Therefore the flux Φ_c changes only the phase difference γ over the chain. Unlike for the measurement of the SQUID chain (see chapter 5), in this case the measurement is much simpler to analyze, as the switching occurs very close to the maximal phase $\pi/2$ over the readout junction. In a first order approximation we consider that the supercurrent of the chain changes the effective current bias of the read-out junction. As we will see later, this approximation only gives a qualitative understanding. For a quantitative analysis, a more accurate and complex treatment is needed (see section 3.3 and chapter 6). The switching current through the parallel circuit represented in Fig.4.4 can be written as the sum of the partial supercurrents in the two branches:

$$I_{SW}(\gamma) = I_S(\gamma - \frac{\pi}{2}) + I_0^{RO}\sin(\frac{\pi}{2}) \qquad (4.11)$$

Here, $I_S(\gamma)$ is the supercurrent in the rhombi chain and I_0^{RO} is the read-out junction critical current. Since $I_0^{RO} \gg I_S$, the γ dependence of the switching current of the shunted rhombi chain directly reflects the current phase relation of the rhombi chain.

The frustration inside the rhombi and the flux inside the closed chain was controlled by a constant external perpendicular magnetic field. The two parameters γ and f are linked by the area ratio between the rhombus and the ring. Since the rhombus area is ~ 100 times smaller than the ring area, using small variations of

the magnetic field B we can vary the phase γ for an approximately constant value of f.
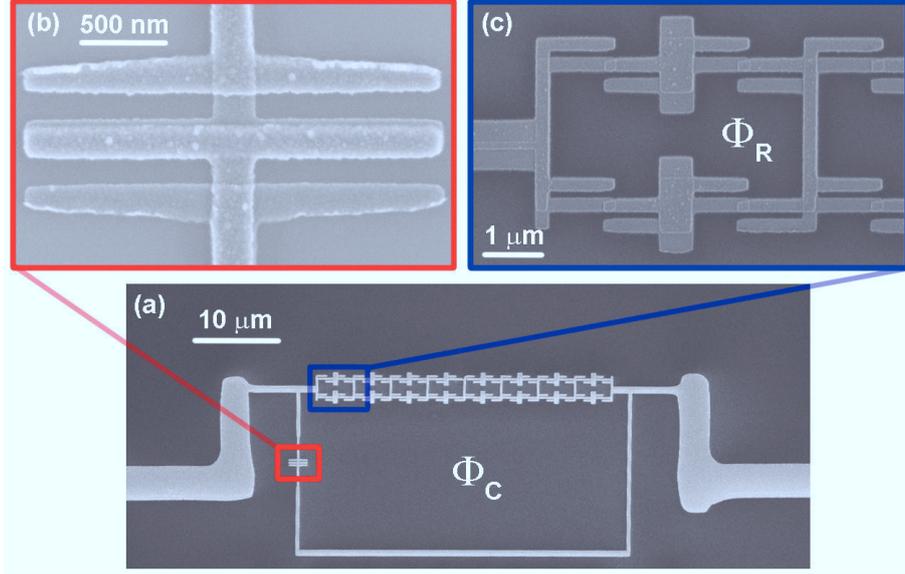

Figure 4.5: a) SEM image of a rhombi chain ($N = 8$) in the closed superconducting circuit. The read-out junction is visible on the left vertical line (b). An enlarged image of one rhombi is also presented (c). For small magnetic field variations, the flux inside the rhombi practically remains constant, while the total phase on the array varies.

The typical elementary junction area is $0.15 \times 0.30\,\mu m^2$. The Josephson energy was inferred from the experimental tunnel resistance of individual junctions and the nominal Coulomb energy was estimated from the junction area using the standard capacitance value of $50\,\mathrm{fF}/\mu m^2$ for aluminum junctions. E_J and E_C as well as the number of rhombi were chosen near the range of the optimum parameters prescribed in Ref. [89]. The Josephson energy for one junction in the rhombus is $E_J = 9\,\mathrm{K}$ and the charging energy $E_C = 0.45\,\mathrm{K}$. So the chain is well in the classical regime, with $E_J/E_C = 20$. The read-out junction has a Josephson energy of about $50\,\mathrm{K}$ and a charging energy in the range of $50\,\mathrm{mK}$, so its phase is very well defined.

The sample was made by standard e-beam lithography and 2 angles shadow evaporation, using an e-beam system and an ultra high vacuum evaporation chamber. The array consists of small $Al/AlO_x/Al$ tunnel junctions deposited on oxidized silicon substrates. The respective thicknesses of the Al layers were 20 and 30 nm. The tunnel barrier oxidation was achieved in pure oxygen at pressures around 10^{-3} mbar during 5 minutes. The fabrication process is explained in detail in chapter 2. The sample was mounted in a closed copper block which was thermally anchored to the cold plate of either a He^3 insert or a dilution fridge. All lines were heavily filtered by thermocoaxial lines and $\pi-$filters integrated in the low temperature copper block. Additional low frequency noise filters were placed at the top of the cryostat. For a detailed description of the measurement setup see chapter 2.4. An electron beam image of a typically measured sample is shown in Fig. 4.5. A SEM image of one rhombus is shown in Fig. 4.5c. The actual design of the resist mask

was optimized to insure the best homogeneity of junction critical currents (section 2.2).

Bernard Pannetier has experimentally studied the classical current-phase relation of a rhombi chain [91]. The observed dependence of the switching current I_{SW} vs the external magnetic flux is shown in Fig. 4.2.1. Both the rhombi frustration f and the phase along the main ring γ are controlled by the magnetic field.
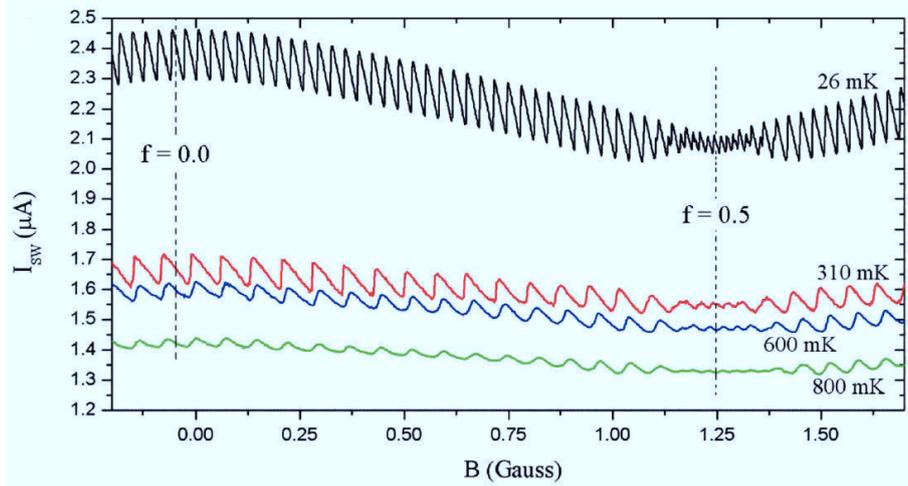

Figure 4.6: Experimental plot of the switching current vs external magnetic field at different temperatures. The higher temperature measurements correspond to a sample with a phase bias loop that has a smaller surface (compared to the sample presented in fig. 4.5), so the observed oscillations vs magnetic field have a bigger periodicity.

We observe a complex dependence of I_{SW} as a function of the magnetic flux with mainly one slow periodic envelop of period 2.57 Gauss that we attribute to the frustration inside the rhombus and one fast sawtooth oscillation that we understand as the modulation of the supercurrent as a function of the phase γ. The number of periods differs for the two measured samples as expected from the difference between the ring areas.

The fast oscillating component of the switching current represented in Fig. 4.2.1 is shown in Fig. 4.2.1. The main features of this experimental result follow the theoretical predictions summarized in Fig. 4.3. Since by changing the magnetic field we vary in the same time the frustration and the phase, we obtain supercurrent oscillations with a modulated amplitude. In Fig. 4.2.1 we have also plotted the theoretical envelop I_{env} (dotted lines) of the supercurrent as calculated for the actual junction parameters in the classical limit. This line is given by the maximum of the supercurrent $I_S(\gamma)$ and except for the two small windows visible near $f = \pm 1/2$ it is given by $I_{env} = i_c \frac{\pi}{N} \cos(f/2)$ (here $N = 8$). Within the frustration window (see eq. (4.9)), I_{env} falls linearly to its minimum value $i_c \frac{\pi}{2\sqrt{2}N}$ at $f = \pm 1/2$, as theoretically expected.

Any single oscillation in Fig. 4.2.1 is practically the current-phase relation for the rhombi chain at a fixed frustration. In fig. 4.8 we present current phase relations at $f = 0$ and in the vicinity of maximum frustration $f \approx 0.5$. We have verified
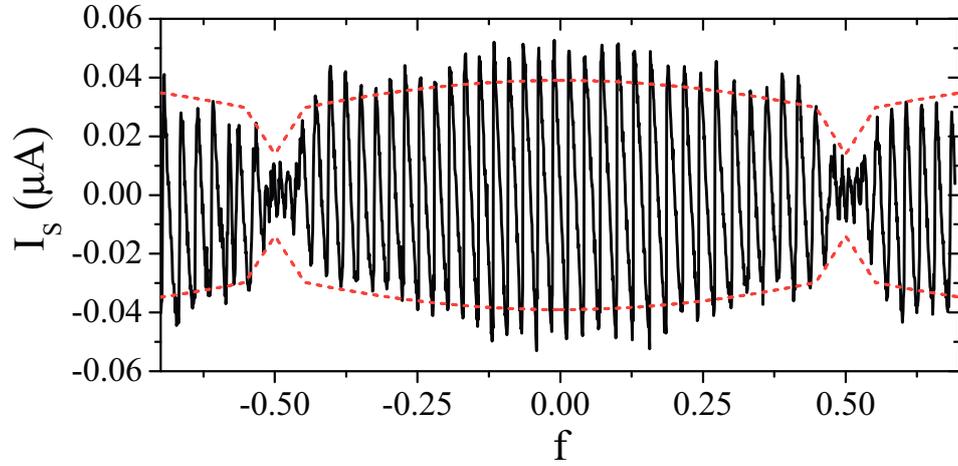
Figure 4.7: The fast oscillation component I_s of the switching current at $T = 310 mK$. The continuous plot represents the measured supercurrent through the chain. The expected amplitude of the supercurrent is shown as red dotted lines.
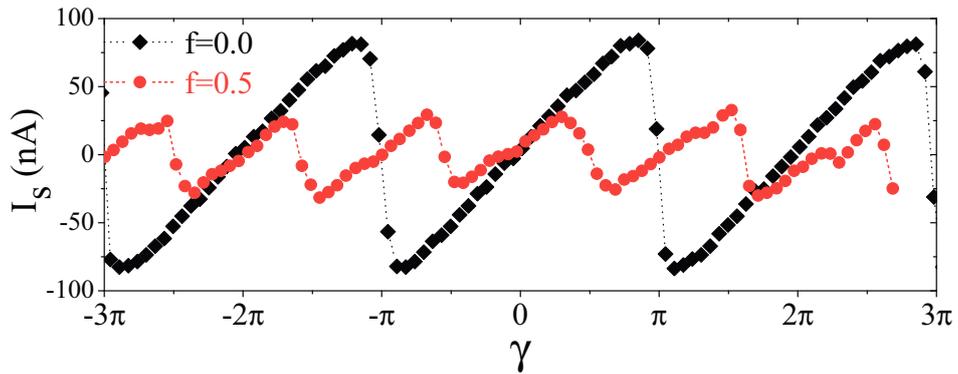
Figure 4.8: Experimental evidence of the doubling of the current-phase relation at half flux quantum frustration. The black diamonds represent the measured current-phase relation for the 8 rhombi chain at zero frustration. The red circles represent the measured current-phase relation at maximum frustration: $f = 0.5$. The halving of the current-phase periodicity is the signature of $4e$ transport.

that the fast modulation is periodic with period $h/2e$ except near $f = 1/2$ where the period is $h/4e$ (see Fig. 4.8). This result confirms precisely what is illustrated in Fig. 4.3 : the chain states undergo a transition from phase periodicity 2π to periodicity π when the rhombi are fully frustrated. Let us notice here that the half periodicity is not actually visible over many periods since the control magnetic flux changes both the frustration and the phase. Instead, we do observe a sequence of saw teeth with unequal amplitudes which become regular only at exactly $f = 1/2$. The doubling of the periodicity of the supercurrent is measured up to a temperature of $T = 800\,\mathrm{mK}$.

In conclusion, we have observed the doubling of the current-phase periodicity at maximal frustration and the measured amplitude of the supercurrent coincides fairly well with the classical value obtained from the nominal critical current of the individual junctions. Considering the large ratio $E_J/E_C = 20$, phase-slips are very small. They only provide the necessary mechanism for the chain to relax in its ground state. Therefore the supercurrent has the expected sawtooth-like shape.

4.2.2 Current-phase relation of a complex rhombi network

The geometry of the measured rhombi network was adapted to correspond to the theoretical proposal for the topologically protected qubit [37–39]. The network consists of three chains of four rhombi in parallel, with the middle islands connected together (see. Fig. 4.9). We have used basically the same readout procedure as described in the previous section. The only notable difference is the introduction of a mutual inductive coupling M in the current bias line, which allows the application of nanosecond current pulses.

The sample was fabricated in the group of M. Gershenson at Rutgers University, using a slightly different lithography procedure, the so called *Manhattan technique.* This technique uses two angle evaporations perpendicular to a cross of deep resist trenches [92]. Its main advantage is that it does not need the fabrication of suspended resist bridges, which are often the most fragile element in the resist mask. However, the main steps of the fabrication are the same as the ones we use and that we described in detail in chapter 2.1. An electron beam image of the measured rhombi network is presented in figure 4.10.

The physics of this type of rhombi networks is similar to the physics of a single chain. The main effect of connecting three chains in parallel is that we increase the critical current of the system. This corresponds to a higher barrier between the states with $\gamma = 0$ and $\gamma = \pi$ (see fig. 4.3) of the network in the vicinity of maximal frustration. Thus, adding chains in parallel is a practical way of increasing the barrier between the states 0 and π without increasing the E_J of the individual junctions.

The Josephson junctions forming the network are classical junctions with $E_J/E_C = 8$. Both the charging and the Josephson energy scales are much bigger than the thermal energy at the base temperature of $50\,\mathrm{mK}$: $E_C = 0.35\,\mathrm{K}$ and $E_J = 2.9\,\mathrm{K}$. The critical current of the read-out junctions is $I_C^{RO} = 650\,\mathrm{nA}$.

The observed dependence of the switching current I_{SW} *vs* the external mag-
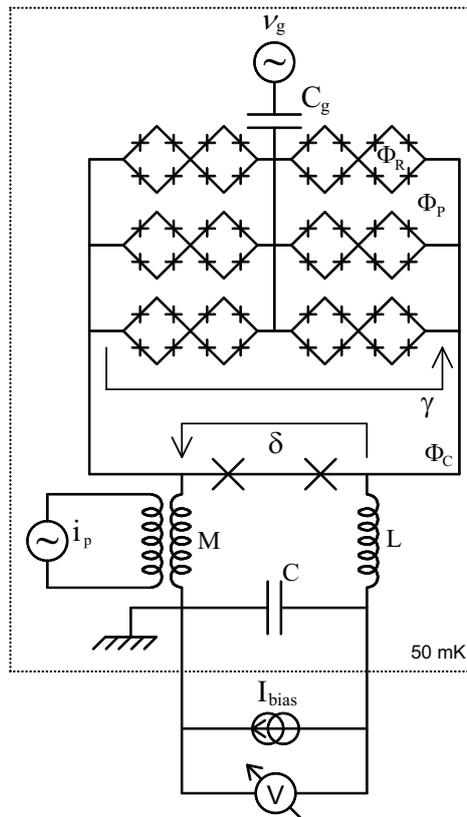
Figure 4.9: Experimental setup for the measurement of the topologically protected rhombi network.
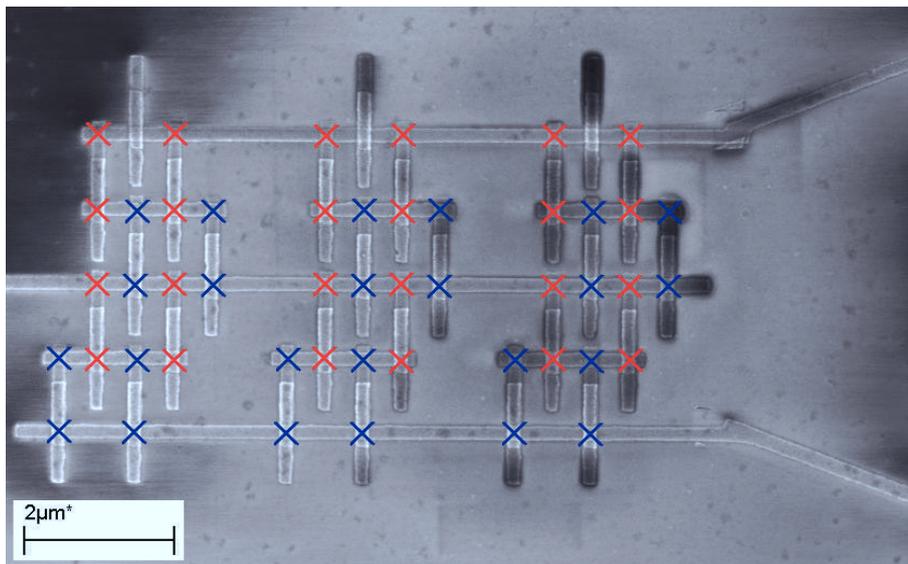

Figure 4.10: e-Beam image of the rhombi network. The neighboring junctions corresponding to the same rhombus have been marked by matching color **X** symbols. The corresponding electrical scheme is shown in fig. 4.9.
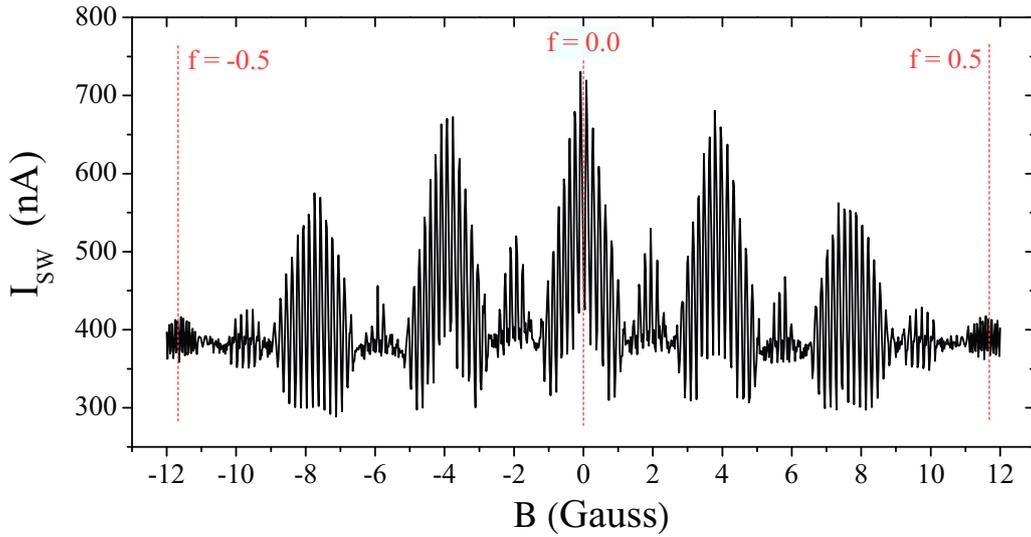
Figure 4.11: Experimental plot of the switching current of the rhombi network *vs* external magnetic field B. The red dotted lines show the positions of the maximal and zero rhombi frustration regions.

netic flux is shown in Fig.4.11. Both the rhombi frustration f and the phase along the main ring γ are controlled by the magnetic field via the fluxes Φ_R and Φ_C respectively. The fast oscillations are given by the rapid growing flux Φ_C with the magnetic field B. The slowest modulation corresponds to the sweeping of the the flux Φ_R inside one rhombus. In addition to these two periodicities, we also observe an intermediate frequency modulation of the envelope of the oscillations. This modulation is given by the flux Φ_P inside the loop in between two neighboring chains (see fig. 4.9).

The measured switching curve shown in fig. 4.11 has a complex structure. Besides the modulations arising from the three characteristic fluxes threading the sample (Φ_R, Φ_C and Φ_P), we also observe an oscillation of the median line, defined as the average position of the switching currents over a complete Φ_C oscillation. Part of the median line evolution with magnetic field B can be explained by junction inhomogeneity in the rhombi network [40]. As we will show in chap. 6.5, additional modulations of the median line are expected if we calculate more exactly the escape process from the total washboard potential: read-out junction plus rhombi network.

In figure 4.12 we present measured current-phase relations for the rhombi network in the ground state. We have used both long current pulses with $\Delta t = 50\,\mu$s and short pulses with $\Delta t = 10\,$ns. As expected, in the region around maximal rhombi frustration $f = 0.5$ (Fig. 4.12b) we observe a halving of the current-phase periodicity. The sample was designed in such a way that at $f = 0.5$, the parasitic flux ϕ_P is an integer number of flux quantum, thus the associated persistent current is zero. As in the case of the simple rhombi chain (see chap. 4.2.1) the change by a factor of two of the switching current periodicity is a clear signature of the $4e$ electrical transport.

The insets of figure 4.12 show the switching histograms at different points of
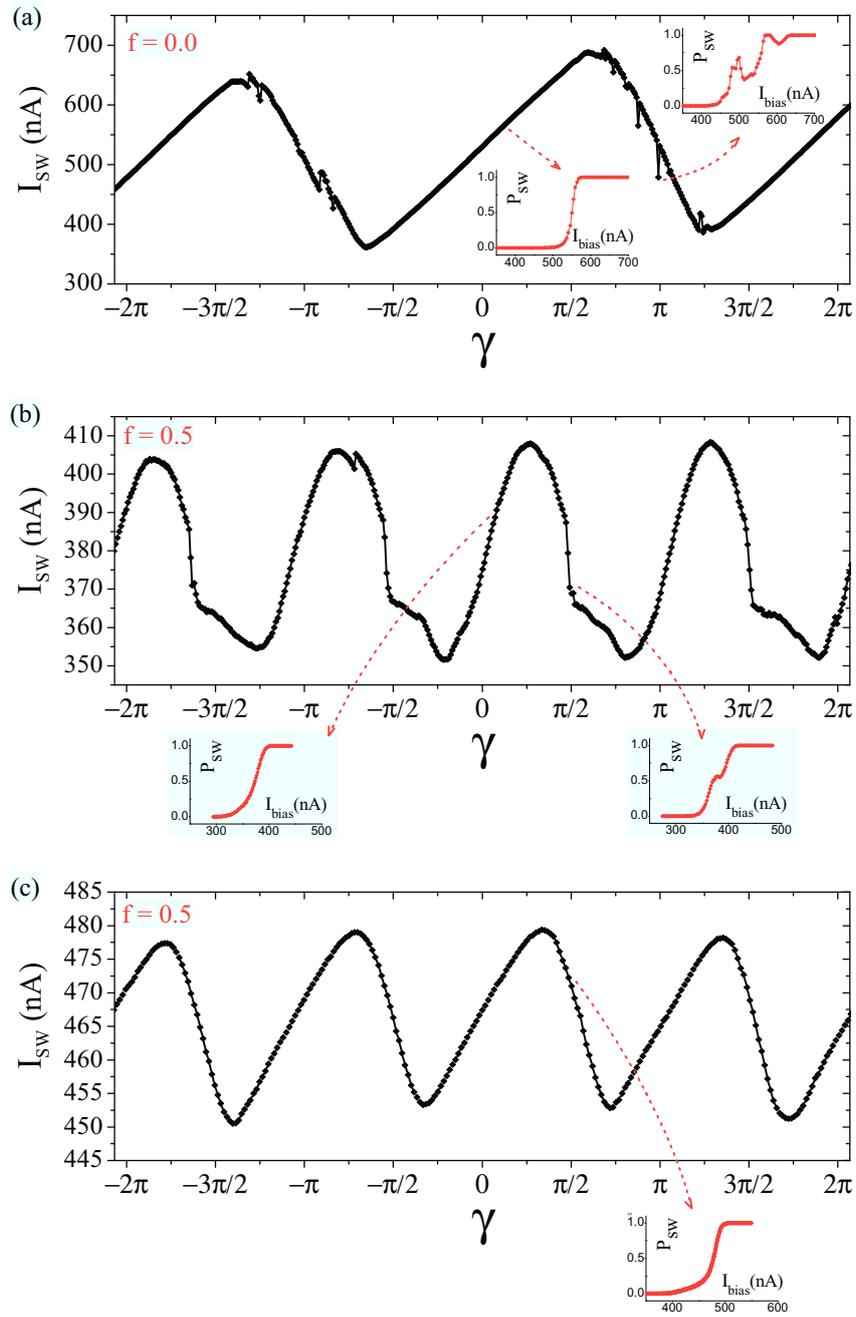
Figure 4.12: Measured current-phase relations for the rhombi network at zero frustration (a) and at maximal frustration (b) and (c). The duration of the measurement pulses for (a) and (b) is $\Delta t = 50 \, \mu s$. The results presented in (c) have been measured using the fast current line, with a duration of the measurement pulse $\Delta t = 10 \, ns$. The insets show the measured switching current histograms at different points in the current-phase relations, indicated by the red arrows.

the current-phase relation. In fig. 4.12a, at $\gamma \simeq 0$ we measure the usual, monotonic "s" shaped curve that we expect considering the standard MQT escape model [10] out of a sinusoidal tilted washboard potential. In contrast, at $\gamma \simeq \pi$, we observe a non monotonic switching histogram. It presents several peaks and its width is considerably larger than at $\gamma \simeq 0$. The switching current of the circuit is defined as the bias current for which we measure an escape probability $P_{SW} = 50\,\%$. Whenever the height of one of the peaks in the histograms is large enough for the peak to cross the $50\,\%$ level, we will observe abrupt variations in the shape of the current-phase relation. It is precisely what can be seen in fig. 4.12a for $\gamma \simeq \pi$. The irregular structure of the histograms originates in the complex escape process from the washboard of the total Josephson circuit composed of the read-out junction and the rhombi network. A detailed analysis of MQT escape process from an arbitrary shaped potential is presented in chapter 6.

At $f = 0.5$, as the critical current of the network is significantly diminished, the washboard potential is closer to the standard tilted sinusoidal and the irregularities in the switching histograms at $\gamma \simeq \pi$ are smoothed. Nevertheless, we can still observe non monotonic intervals in the histograms. They induce a deformation of the current-phase relation shape at $\gamma \simeq \pi$, as shown in fig. 4.12b.

If we use fast measurement pulses, with $\Delta t \sim 10\,\text{ns}$, to induce the escape, we observe smooth histograms, even at $\gamma \simeq \pi$, as shown in the inset of fig. 4.12c. The resulting current-phase relation of the rhombi network is very regular and we no longer observe any jumps or deformations. The details of the method we have used to apply the fast current pulses are presented in the next section (section 2.5).

In conclusion, we have measured the ground state of two types of rhombi networks: a simple 8 rhombi chain and a structure of 3 chains in parallel, each containing 4 rhombi. The Josephson junctions in the chains were in the classical phase regime with $E_J \gg E_C$. Both systems show clear signatures of current transported by correlated pairs of Cooper pairs of charge $4e$, in the vicinity of half flux frustration inside the rhombi loops. Our results are in qualitative agreement with similar measurements performed in Michael Gershenson's group.

4.3   Quantum rhombi chains

In the region where the frustration is small, $0 \leq f \ll 1$, a rhombi chain is very similar to a simple JJ chain. The reason is that around zero frustration, the energy of a single rhombus as a function of the diagonal phase difference has only *one* minimum (see Fig. 4.2a). This implies the coincidence of the classification of the classical states for our system and for the single Josephson junction chain. In this section we present the theory of quantum fluctuations in a non-frustrated rhombi chain which we used to fit the experimental data. In our analysis we assume that the Josephson energy of the junctions is larger than the charging energy and quantum phase fluctuations in *individual* Josephson junctions are small. However, as we will see below, the fluctuations in the whole chain can become strong.

Quantum fluctuations (more precisely quantum phase-slips) lead to the mixing of classical states described above. As we have shown in chapter 4.1.2, at large

(a)

(b)
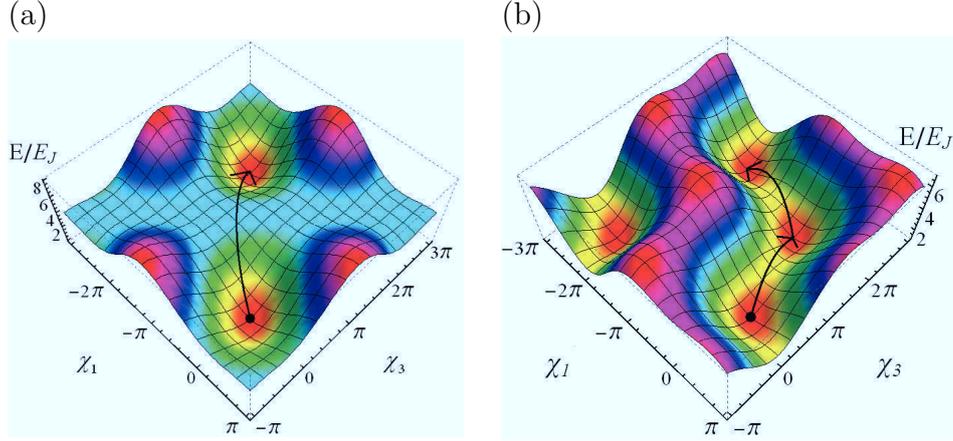
Figure 4.13: The energy landscape for one rhombus at zero frustration ($f = 0$) (a) and at maximal frustration ($f = 0.5$) (b) as a function of the phase differences χ_1 and χ_3 of Josephson junctions in opposite branches of the rhombus. The transition of the chain from state $|m\rangle$ to state $|m+1\rangle$ corresponds to a 2π jump of one of the diagonal rhombus phases θ_i. This transition implies a simultaneous flip of the two phases χ_1 and χ_3 respectively by -2π and 2π. The arrow in the figure represents the corresponding classical trajectory. The phenomenon can also be seen as the process of one vortex crossing the rhombus ring.

E_J/E_C this effect can be described within the tight-binding approximation (cf. [52]). Classical states lie far from each other in the configuration space and are separated by barriers of the order E_J (see Fig. 4.13a). At large E_J/E_C the amplitude of quantum tunneling from state $|m\rangle$ to $|m'\rangle$ is exponentially small and decreases fast with the increase of the distance between $|m\rangle$ and $|m'\rangle$. For a given state $|m\rangle$ the closest states in the configuration space are $|m \pm 1\rangle$. To achieve the state $|m+1\rangle$ one needs to change the phase difference across the diagonal of one rhombus by 2π (at large N, cf. eq. (4.6)). Since we need to maintain the sum of the phase differences around the rhombus (fixed by the zero flux inside it, see eq. (4.2)) we need to change by $\pm 2\pi$ the phase differences over *two* junctions in different branches of the rhombus (see Fig. 4.13). Let us denote the amplitude of such a process by v. In a semi classical approximation this amplitude is determined by the vicinity of the classical trajectory connecting states $|m\rangle$ and $|m+1\rangle$ in imaginary time [91]:

$$v = 4.50 \, (E_J^3 E_C)^{1/4} \exp\left(-S_0\right) \tag{4.12}$$

Here S_0 is the imaginary-time action on the classical trajectory (instanton). As it is easy to see from the preceding discussion, S_0 is just twice the action describing a phase-slip in a single junction. We thus have (cf. equation 7 of the reference [52], note the difference in the definitions of E_C):

$$S_0 = 2\sqrt{\frac{8E_J}{E_C}} \tag{4.13}$$

We can now construct the tight-binding Hamiltonian describing the effect of the phase-slips on the properties of the chain

$$H|m\rangle = E_m|m\rangle + 4Nv|m+1\rangle + 4Nv|m-1\rangle \tag{4.14}$$
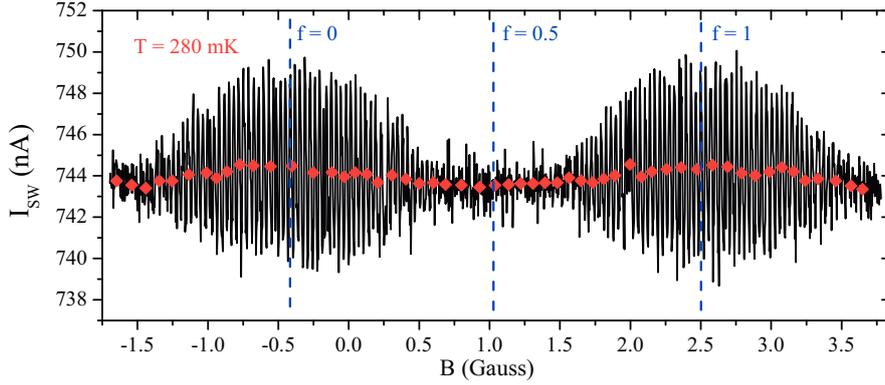
Figure 4.14: Measured switching current *vs* external magnetic field at the temperature $T = 280mK$. Red diamonds: the median component of the switching current.

The coefficient 4 in the total tunneling matrix element is due to the number of possible tunneling paths within one rhombus while N appears here because of the fact that a phase-slip in any rhombus brings the system to the same state.

By solving numerically the Hamiltonian (4.14) and using the general relation $I_S = \frac{2e}{\hbar} dE/d\gamma$ one can find the current-phase relation for the rhombi chain at arbitrary fluctuations strength. This is the exact procedure that we have used in the following section in order to fit the measured current-phase relation for quantum chains. We found a very good agreement between the theoretical predictions and the measured data.

4.4 Measurement of the current-phase relation of a quantum rhombi chain

In order to characterize the regime of quantum fluctuations, we performed experiments on an 8 rhombi chain with a ratio of $E_J/E_C \approx 2$. The circuit electrical scheme is identical to the one presented in Fig.4.4. The fabrication process was practically the same as for the classical rhombi chain (for details on the fabrication, see chapter 2). The relevant energy scales for the rhombi chain are given by $E_J = 1.6\,\mathrm{K}$ and $E_C = 0.8\,\mathrm{K}$. The readout junction of this circuit has a critical current $I_C^{RO} \simeq 1\,\mu\mathrm{A}$.

Fig. 4.14 shows the dependence of the measured switching current as a function of the applied magnetic field. As in the case of the classical chain, the signal can be seen as a superposition of three components. The modulated oscillating component characterizes the dependence of the supercurrent of the chain as a function of both the frustration f and the phase difference γ. The oscillations are periodic with period $h/2e$. As we approach the frustrated regime no oscillations of the supercurrent are measured: in the region $f = 1/2$ the supercurrent of the chain is strongly suppressed and smaller than the $\approx 1\,\mathrm{nA}$ noise level of our experiment.

The median component I_{med}, shown in Fig.4.14, as in the case of the classical chains, shows a periodic evolution as a function of the frustration. We measure an amplitude of about 1 nA for the I_{med} oscillations. As we show in chapter 6 (fig.
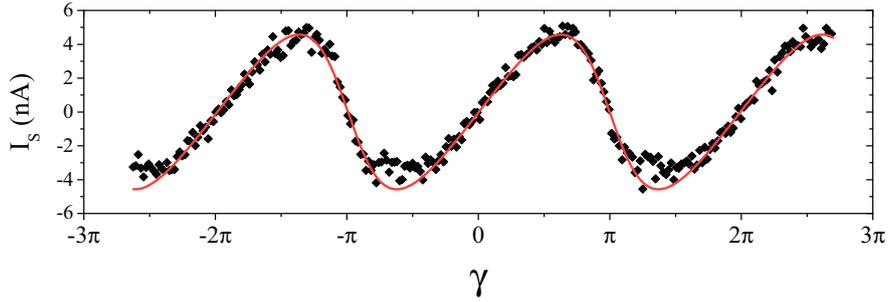
Figure 4.15: Measured switching current (black diamonds) *vs* external magnetic field in the zero frustration region at $T = 280mK$. The line (in red) represents the theoretical fit which gives an effective value for the Josephson energy $E_J^* = 0.5E_J$. For clarity, from the measured switching current we have substracted the constant switching current value of the read-out junction: $I_{med}(f = 0) \simeq 743\,nA$.

6.12 and fig. 6.11), this periodic behavior of I_{med} is an effect of the switching from the total potential of the read-out junction plus the rhombi chain.

We did a detailed quantitative analysis of the current-phase relation at zero flux frustration. Fig.4.15 shows the measured current phase relation in the non frustrated regime that can be perfectly fitted by the theory described in section 4.3. The only fitting parameter is the Josephson energy E_J^* for which we find half of the experimental determined one. The experimental value for E_J has been deduced from the normal state resistance measurement of the large Josephson junction that is in parallel to the rhombi chain (similar to the measurement in Fig. 3.3). Unfortunately the maximal current in the IV characteristic was two small and we did not reach the linear regime. Thus, our estimated value for E_J might be significantly larger than the real value.

This experimental result suggests the validity of the theoretical model initially proposed by Matveev *et al.* [52] for the current-phase relation in simple Josephson junction chains, that we extended here for QPS occuring in the two dimensional potential of the rhombus.

As we increase the applied magnetic field, the frustration inside the rhombi modifies the value of the effective Josephson energy, which becomes $E_J cos(\pi f)$. Using this value, we calculated the evolution of the critical current as a function of the frustration f. Fig.4.16 presents both the results of the calculations and the measured values for the critical current. We can see that the model gives a quantitative description for the measured current amplitude dependence in the non frustrated regime while it can only give a qualitative description in the frustrated region. Indeed, if we compare the phase-slip quasiclassical trajectories at $f = 0$ and close to $f = 0.5$ but outside the frustration window (eq. (4.9)), presented in Fig. 4.13a and b, we see that they are very different.

The width of the histograms at $300\,mK$ is $w \simeq 45\,nA$. At low temperatures, up to $T = 400\,mK$ we observe a saturation of the histogram width w, which is a signature of the MQT escape becoming dominant over the thermal escape [10]. At higher temperatures the switching current decreases and so does the width of the
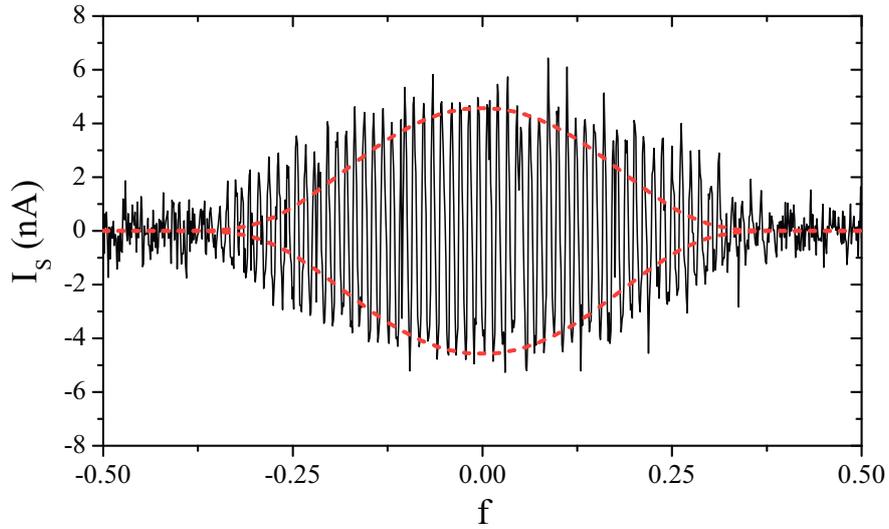
Figure 4.16: In black: the measured switching current oscillations as a function of the frustration f. The red dotted line gives the theoretical prediction for the amplitude of the switching current oscillations by using an effective value $E_J^* = 0.5E_J$. For clarity we have substracted the median component I_{med}.
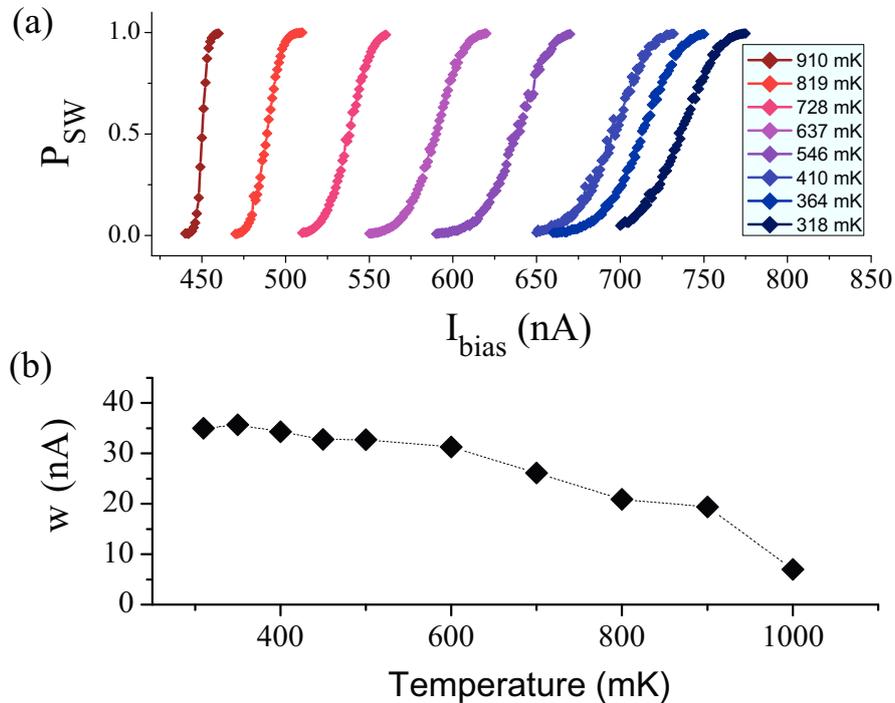
Figure 4.17: Temperature dependence of the switching curves. (a) Measured histograms at different temperatures. (b) The measured histogram width w at different temperatures.

switching curves w (see fig. 4.17). The decrease of w can be explained by the fact that the read-out junction is not strongly under damped, but it is rather in an intermediate regime with a quality factor $Q = 3$. Thus, we can expect more complex switching dynamics, when the phase particle can be retrapped in the next well of the washboard [93].

In conclusion, experiments on the rhombi chain in the quantum regime ($E_J/E_C \approx 2$) show a significant reduction and rounding of the current-phase relation in the non frustrated region and a complete suppression of the supercurrent at maximal frustration. In the non frustrated regime, the QPS model proposed by Matveev *et al.* [52] fits the measured current phase-relation for an eight rhombi quantum chain. These experiments qualitatively suggest the validity of the theoretical model. For an accurate quantitative comparison, in the next chapter (5) we will present detailed measurements performed on Josephson junction chains.

4.5 Measurement of the effect of microwave irradiation on the state of a 2D rhombi network

In this section we present the results of an experiment where we shined microwaves on a 2D rhombi network (see section 4.2.2), in order to attempt the excitation the superior levels in the energy spectrum. Ideally, we would like to observe the transition to the first excited state of the topologically protected rhombi qubit. We start by discussing our experimental setup for the application of measurement pulses with short rise and duration time. These pulses are essential for the detection of physical states which decay rapidly in time. We will then continue with the presentation of the response of the rhombi network to microwave irradiation.

In Fig. 4.18 we show a simplification of the electrical scheme of Fig. 4.9 for the circuit in the harmonic limit. We replaced the Josephson junction circuit by an equivalent inductance L_J. Due to the fact that the inductance of the read-out junctions is significantly smaller than that of the rhombi network, $L_J^{RO} \ll L_{rhombi}$, the total inductance of the Josephson junction circuit is well approximated by $L_J = 2\,L_J^{RO}$. The scheme represented in Fig. 4.18 is composed of two electrical circuits, coupled by the mutual inductance M. The first circuit that we call *primary* is directly connected to a high frequency generator. We denote the current in the primary circuit by i_p. The secondary circuit is a resonant LC circuit with a total inductance $L_{tot} = L_J + L \simeq 50\,\text{nH}$ and a capacitance $C = 270\,\text{pF}$. The value of the mutual coupling is $M = 50\,\text{pH}$.

In Fig. 4.19, we show the resonant response of the LC secondary circuit, to a microwave signal in the primary. At resonance, the switching probability of the Josephson circuit increases and we measure a positive peak. The position of the peak corresponds to the expected frequency: $v_{LC} = 1/\left(2\pi\sqrt{L_{tot}C}\right) \simeq 43\,\text{MHz}$.

I would like to discuss the method we used to apply short measurement pulses. As it can be seen in the electrical scheme in fig. 4.18, we induce the fast pulse from the primary circuit via an inductive mutual coupling M into the secondary circuit, which is equivalent to a LC underdamped oscillator. Any current step in the
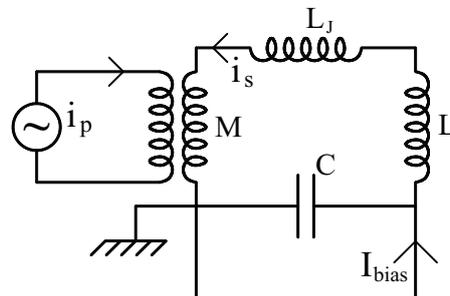
Figure 4.18: Simplified electrical scheme of the sample in Fig. 4.9, in the harmonic limit. The rhombi network in parallel with the read-out junctions is replaced by an equivalent inductance L_J. The arrows represented in the figure, indicate the positive sign convention for the currents I_{bias}, i_p and i_s.
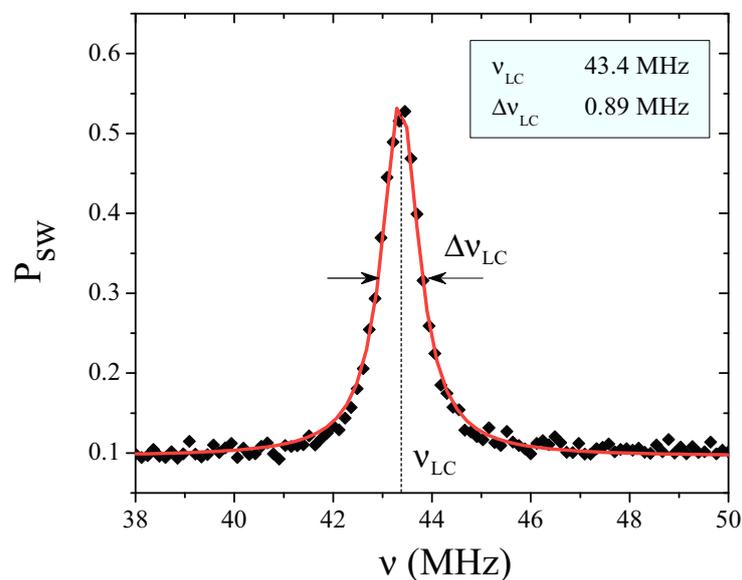
Figure 4.19: Measured resonance of the LC circuit represented in Fig. 4.18. The red line shows a Lorentzian fit of the measured data. The inset shows the fitted values for the frequency of resonance v_{LC} and the width of the peak.
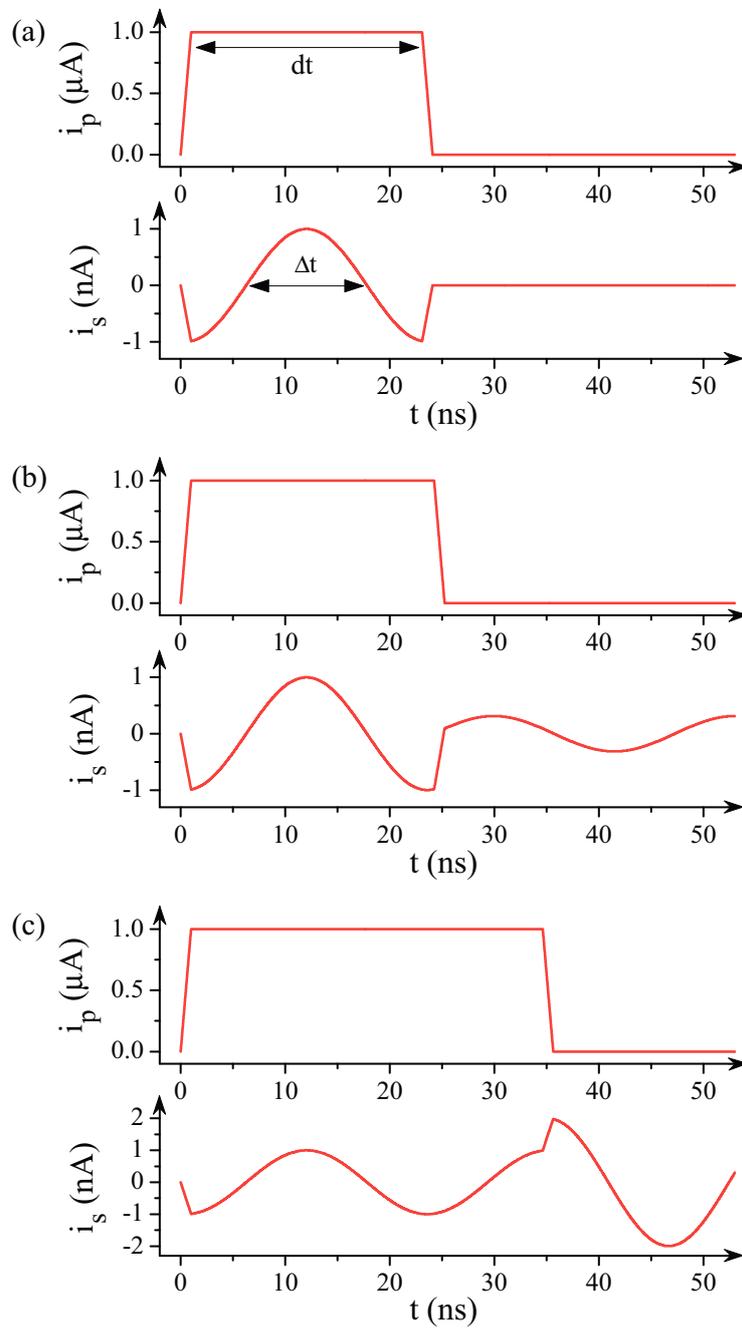
Figure 4.20: Comparison between the electrical current i_p in the primary circuit and the electric response of the current i_s in the secondary circuit, for three different time durations dt of the pulses: (a) $dt = 2\pi\sqrt{L_{tot}C}$, (b) $dt = 1.05 \times 2\pi\sqrt{L_{tot}C}$ and (c) $dt = 1.5 \times 2\pi\sqrt{L_{tot}C}$.

primary circuit will produce oscillations in the secondary circuit. In order to induce a short pulse in the sample circuit, the duration dt of the primary current pulse i_p needs to be carefully calculated and adjusted. Otherwise, current oscillations at the eigenfrequency of the LC oscillator persist in the secondary circuit, long time after the initial pulse in the primary circuit. The optimal value of the primary current pulse duration is $dt = 2\pi\sqrt{L_{tot}C} \simeq 23$ ns. For this value of dt there are no current oscillations in the sample circuit after the end of the pulse in the primary (see Fig. 4.20a).

We calculated the response of the secondary circuit to a current pulse in the primary one using the Laplace formalism. The response function of the secondary circuit, in frequency representation, is given by:

$$Y(s) = \mathcal{L}\{i_s(t), s\} = \frac{M}{Z(s)}\mathcal{L}\{i_p(t), s\} \tag{4.15}$$

where $\mathcal{L}\{i_p(t), s\}$ and $\mathcal{L}\{i_s(t), s\}$ are the Laplace transforms of the primary and secondary current pulses. $M/Z(s)$ is the frequency dependent transfer function to the secondary, where $Z(s)$ is given by:

$$Z(s) = L_{tot} \cdot s + \frac{1}{C \cdot s} \tag{4.16}$$

In order to obtain the current in the secondary we calculate the inverse Laplace transform for the response function $Y(s)$:

$$i_s(t) = \mathcal{L}^{-1}\{Y(s), t\} \tag{4.17}$$

Fig. 4.20 shows the calculated current response $i_s(t)$ of the sample circuit for three different durations dt of the current pulses i_p. In Fig. 4.20a, for the optimal current pulse duration $dt = 23$ ns, we notice that the oscillations of the current i_s are perfectly suppressed at the end of the pulse. We define the duration of the fast pulse in the sample circuit Δt, as the time interval for which the values of the current i_s are positive. For the parameters of our LC circuit, $\Delta t \simeq 10$ ns. Fig. 4.20b shows the situation if the pulse duration is 5% longer than the optimum value. We observe non negligible oscillations in the secondary circuit after the end of the current pulse in the primary. For a current pulse with a duration 50% longer than the optimal value, we observe an amplification of the current oscillations in the sample circuit at the end of the pulse in the primary, as shown in Fig. 4.20c.

In order to measure the response of the rhombi network to microwaves, we have performed the following measurement sequence. We apply microwaves via a HF line that is capacitively coupled to the middle island of the network (as shown in Fig. 4.9). We apply a microwave pulse during $10\,\mu$s, in order to excite the higher levels in the energy spectrum of the rhombi network. The microwave pulse is immediately followed by a fast measurement pulse ($\Delta t = 10$ ns), induced in the sample circuit as we have explained above.

We observe several resonance peaks with resonance frequencies depending on Φ_R. A typical resonance peak is represented in Fig. 4.22. In Fig. 4.21 we represented the position of the peaks as a function of the rhombi frustration $f = \Phi_R/\Phi_0$. The signature of the resonant transition to the excited state of the rhombi
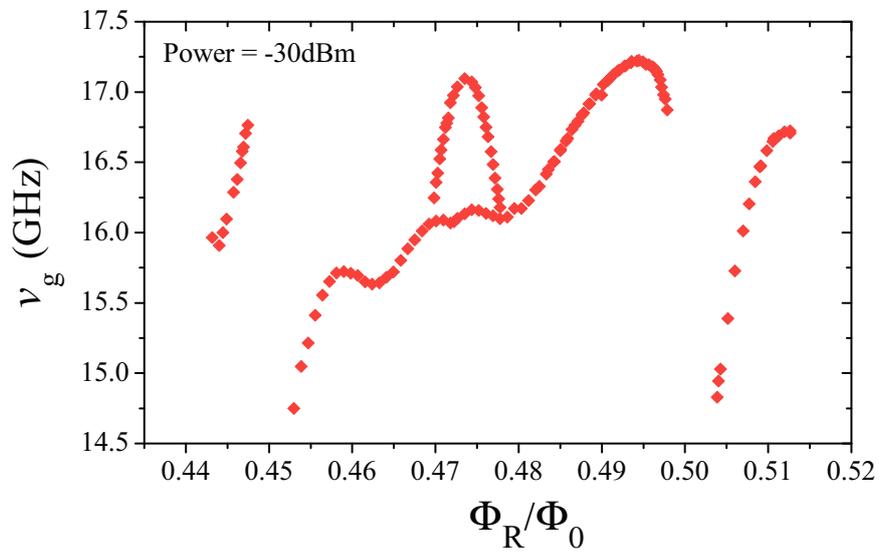
Figure 4.21: The position of the measured peaks as a function of the rhombi frustration $f = \Phi_R/\Phi_0$.
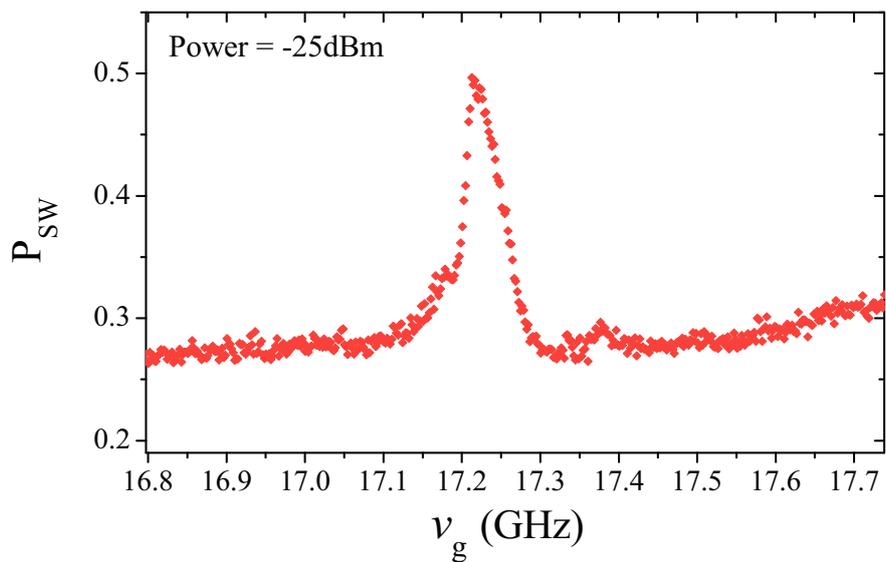
Figure 4.22: Typical rhombi network resonance peak.

network would be a resonance frequency depending periodically on Φ_C, with a period equal to $5 \cdot 10^{-3}\,\Phi_R$. However, despite detailed frequency scans and excitations at high microwave powers, we did not observe any peaks showing Φ_C periodicity. We would like to notice the high power needed for the observation of the resonances of Fig. 4.21. We think that the peaks correspond to transitions to the excited states of a single rhombus in the network. The weak coupling of the rhombus modes to the microwaves in our setup would explain the large power needed for their observation. Similar results have been reported by the experimental group of M. Gershenson at Rutgers University.

In conclusion, we have tried to measure the excited states of a 2D rhombi network, which was designed to realize a topologically protected qubit. The measurements presented in this section suggest that the direct application of microwaves on the middle island of the rhombi network, as depicted in Fig. 4.9 does not provide a sufficiently large coupling to excite the superior levels of the rhombi network. With increasing power, we could only excite local modes of the network instead of the collective 2D qubit modes.

Chapter 5

Measurement of quantum phase-slips in a Josephson junction chain

The interplay between superconductivity and Coulomb interactions has been studied for more than 20 years now [20, 52, 84, 94–103]. In low-dimensional systems, superconductivity degrades in the presence of Coulomb repulsion: interactions tend to suppress fluctuations of charge, thereby increasing fluctuations of phase. This can lead to the occurrence of a superconducting–insulator transition, as has been observed in thin superconducting films [97, 98], wires [20] and also in Josephson junction arrays [84, 99, 101–103] (see Fig. 5.1). The last of these are very attractive
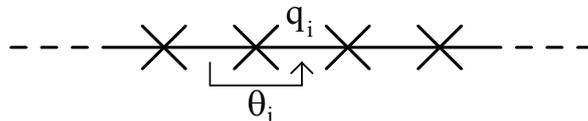
Figure 5.1: Electrical scheme of a chain of Josephson junctions. We denote the polarization charges on the islands q_i and the phase differences between the islands θ_i.

systems, as they enable a relatively easy control of the relevant energies involved in the competition between superconductivity and Coulomb interactions. As we have shown in Chap. 3.1, to each Josephson junction in the chain we can associate two energy scales: the Josephson energy, $E_J = I_c \frac{\hbar}{2e}$, which quantifies the strength of the Cooper pair tunneling through the junction, and the charging energy ,$E_C = \frac{e^2}{2C}$, which quantifies the dual process, the strength of the Cooper pair localization due to the junction capacitance. E_J and E_C can be well controlled by carefully engineering the fabrication process (chap. 2). Moreover, E_J can be tuned in situ, if the junctions are realised in form of SQUIDs, by applying a magnetic flux Φ_S inside the SQUID loop. Josephson junction chains have already been successfully used to create particular electromagnetic environments for the reduction of charge fluctuations [36, 104, 105]. Recently Josephson junction arrays have again attracted interest

as they could provide the basis for the realization of new types of superconducting devices: new types of qubits [36,40], metamaterials, amplifiers [106,107] or quantum current standards [51]. In view of the many possible applications of these systems and the implementation of more complex circuits, it is important to understand quantitatively the ground state properties of Josephson junction chains.

In the following we will present quantitative measurements of QPS in the ground state of a Josephson junction chain [108]. In our experiments, we tune in situ the strength of quantum phase fluctuations, either by tuning E_J or by inducing polarization charges q_i on the superconducting islands of the chain. In both cases, we obtain an excellent agreement with the tight-binding model initially proposed by K. A. Matveev and colleagues [52].

5.1   Theoretical description of QPS in Josephson junction chains without polarization charges

In superconducting circuits, each electrical element such as an inductor, a capacitor or the Josephson element can add a degree of freedom. In the case of small circuits, by applying Devoret's circuit theory [109], a complete analytical description that takes into account all degrees of freedom can be obtained. However, when the circuits contain an increasing number of elements, as for example Josephson junction chains, even numerical solutions of the problem become very cumbersome to obtain when taking into account all degrees of freedom. Nevertheless, our measurements demonstrate that the ground state of a phase-biased Josephson junction chain (see Fig. 5.2a) can be described by a single degree of freedom. Although the chain is a multidimensional object, the effect of QPS can be described by a single variable, m, that counts the number of phase-slips in the chain.

We start by giving a short introduction on the low-energy properties of a Josephson junction chain analyzed in terms of QPS [52]. Let us consider the simplest model for the Josephson junction chain, shown in Fig. 5.2a. The chain contains N junctions and is biased with a phase γ.

Let θ_i be the phase differences over the junctions. Ignoring the charging energy for the moment, in the classical $(E_J \gg E_C)$ ground state the phase bias γ is equally distributed on the N junctions: $\theta_i = \gamma/N$, as illustrated by the solid line in Fig. 5.2b. The resulting Josephson energy hence reads:

$$E_0 = \sum_{i=1}^{N} E_J \left(1 - \cos \theta_i\right) = E_J \frac{\gamma^2}{2N} \tag{5.1}$$

The chain is simply equivalent to a large inductance $N L_J$, which is N times larger than the Josephson inductance of one junction. If a phase-slip occurs on one of the junctions, say the jth junction, then $\theta_j \to \theta_j + 2\pi$. The constraint $\sum_i \theta_i = \gamma$ would be violated after such a phase-slip event if the phases across all other junctions do not adjust. Therefore, the phase difference θ_i over all other junctions changes a little from γ/N to $(\gamma - 2\pi)/N$ to accommodate the bias constraint (see the dashed line in Fig. 5.2b). We notice that a phase-slip on a single junction leads to a collective response of all junctions. Consequently, after m phase-slips, the Josephson energy
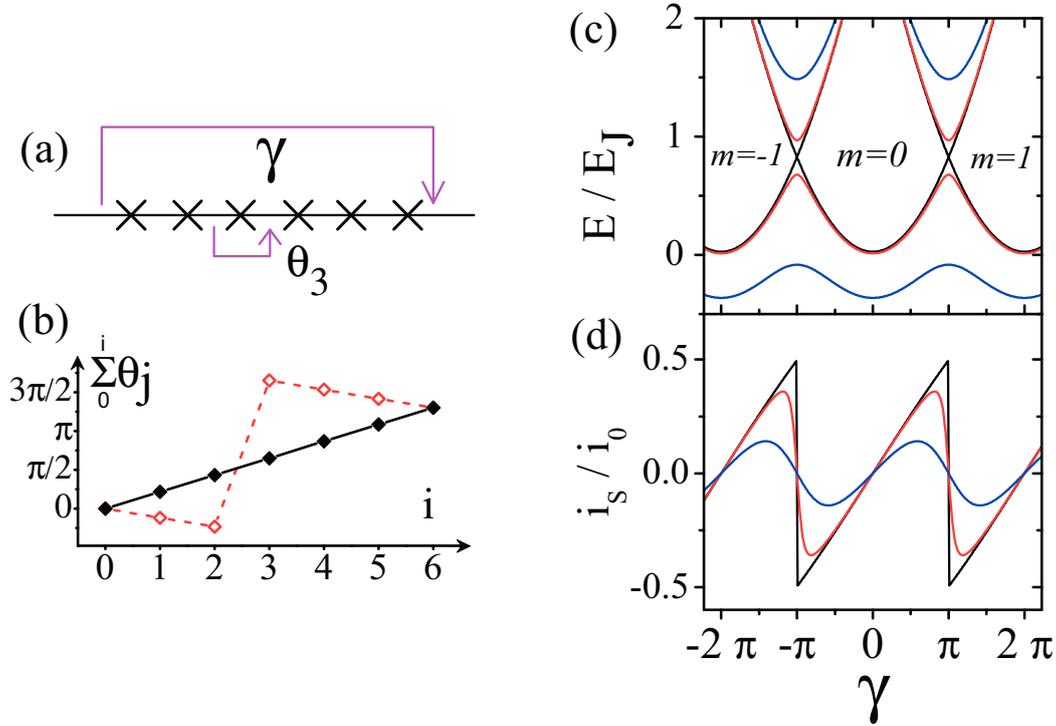
Figure 5.2: Graphic representations describing the effect of QPS in a six-junction chain and the resulting chain's energy and supercurrent. (a) Schematic picture of the phase-biased Josephson junction chain. (b) Representation of a phase-slip in the chain. The filled diamonds show the initial configuration. The open diamonds show the phase configuration after a 2π flip of the phase on the third junction θ_3. (c) Energy levels of a Josephson junction chain with $N = 6$ as a function of bias phase γ for different ratios E_J/E_C. For $E_J/E_C = 20$ (black lines) no splitting is visible at the crossing points. For $E_J/E_C = 3$ (red lines) a gap emerges that increases rapidly with decreasing E_J/E_C. The blue lines show the energy levels for $E_J/E_C = 1.3$. For each E_J/E_C, the two lowest-lying states have been calculated by numerical diagonalization of the Hamiltonian (5.3). (d) Current–phase relation for the ground state $E_g(\gamma)$ for the same E_J/E_C ratios as in (c). The supercurrent is calculated from the derivative of the energy band: $i_s = (2e/\hbar)(\partial E_g(\gamma)/\partial\gamma)$. The chain current is reported in units of the critical current of a single chain junction $i_0 = (2e/\hbar)E_J$.

of the entire chain changes from $E_J \frac{\gamma^2}{2N}$ to $E_J \frac{(\gamma - 2\pi m)^2}{2N}$. The classical ground state energy of the chain consists of shifted parabolas that correspond respectively to a fixed number m of phase-slips (see Fig. 5.2c). For the special values $\gamma = \pi (2m + 1)$, the energies E_m and E_{m+1} are degenerate.

If we now take into account the finite charging energy E_C, QPS mix the neighboring states $|m\rangle$ and $|m \pm 1\rangle$. The effect is most powerful in the vicinity of the points $\gamma = \pi (2m + 1)$, where the degeneracy is lifted and the crossing points become anti crossings (see the difference between the red and black plots in Fig. 5.2c). In the limit of rare phase-slips, that is, $E_J \gg E_C$, the hopping element for the QPS is just the width of the Bloch band for a single junction. Its value can be approximated by [110, 111]:

$$v = 16 \sqrt{\frac{E_J E_C}{\pi}} \left(\frac{E_J}{2E_C} \right)^{0.25} e^{-\sqrt{8\frac{E_J}{E_C}}} \qquad (5.2)$$

As a phase-slip can take place on any of the N junctions, the hopping term between the two states $|m\rangle$ and $|m \pm 1\rangle$ is given by Nv. Therefore, using a tight-binding approximation, the total Hamiltonian for the chain is:

$$H |m\rangle = E_m |m\rangle - Nv \left[|m - 1\rangle + |m + 1\rangle \right] \qquad (5.3)$$

Figure 5.2c shows the numerical calculation of the two lowest eigenenergies of the Hamiltonian (5.3) for three different ratios $E_J/E_C = 20$, 3, and 1.3 in the case of a six-junction chain. Figure 5.2d shows the corresponding current-phase relation of the chain in the ground state. The chain's supercurrent is obtained by the calculation of the derivative of the ground-state energy $E_g (\gamma)$: $i_s = (2e/\hbar) (\partial E_g (\gamma) / \partial \gamma)$.

For large values of E_J/E_C, quantum phase fluctuations are very small ($v \to 0$) and the current-phase relation has a sawtooth-like dependence. The critical current of the chain is given by the maximum slope of the parabola arches, which is at the crossing points $\gamma = \pi (2m + 1)$. The chain's critical current is:

$$i_c = (2e/\hbar) \left[\partial \left(E_J \frac{\gamma^2}{2N} \right) / \partial \gamma \right]_{\gamma = \pi} = \frac{\pi}{N} i_0 \qquad (5.4)$$

where i_0 is the critical current of one junction. So the critical current of the classical chain is approximately N/π times smaller than that of a single junction of the chain. We call this regime "classical" because the phase-slip amplitude is small and the phases θ_i behave as quasi-classical variables.

When E_J/E_C decreases, quantum phase fluctuations increase, the current-phase relation becomes rounded and it tends ultimately to a sinusoidal (see fig. 5.2d). Thus, the critical current becomes exponentially suppressed with increasing N and decreasing E_J/E_C (ref. [52]).

5.2 Phase biasing schemes for the Josephson junction chain

We have seen that in the framework of the MLG theory of QPS it is essential to lock the phase bias γ over the chain. In figure 5.3, I present different practical

implementations of controlled phase bias.
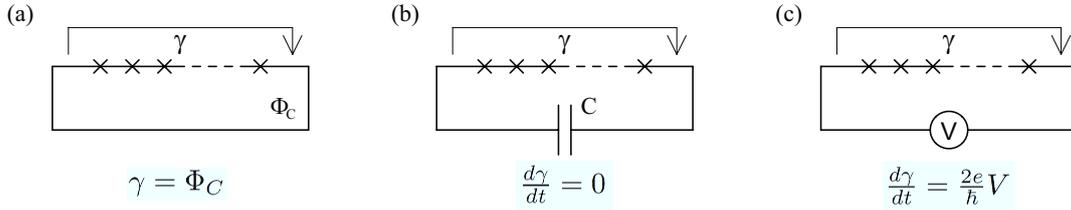
Figure 5.3: Different practical implementations of the phase bias for the Josephson chain.

The first possibility is to lock the the phase γ by inserting the Josephson chain inside a superconducting loop, as depicted in figure 5.3a. γ is locked by the superconducting wire and it is directly tuned by the magnetic flux Φ_C applied on the loop. The advantage of this technique is that it offers direct control of the phase bias. In practice, using this scheme we can sweep γ from 0 to 2π with very good precision, by using either mutual couplings to on chip loops, or by using a coil which induces a perpendicular uniform magnetic field on the plane of the sample. This phase biasing scheme was first implemented by D. Vion et al. [26] to bias a superconducting quBit. It has since been used for the measurement of the ground state of superconducting Josephson circuits [40, 91] and atomic contacts [73].

The second possibility, shown in figure 5.3b, is to lock the phase γ using a large capacitor C in parallel with the chain. In this case we fix the time evolution of the phase to zero. The value of γ will be determined by the energy minimum of the system in a given configuration. If for example we DC current bias the chain, in the dissipation-less regime ($V = 0$) there will be a direct correspondence between the current I and the phase γ. This relation is non other than the current-phase relation, the phase derivative of the ground state energy landscape (for example see fig. 5.2d).

The third option is to voltage bias the junction chain. Following the Josephson equations, the time evolution of the phase will be fixed by the voltage V. This is a particularly interesting biasing scheme in the limit of quantum chains, when phase-slips strongly suppress superconductivity and induce an insulator state. The voltage bias allows us to directly test the critical voltage of the insulator state. It has been recently proposed in ref. [51] that a chain in the insulator regime, under microwave irradiation, would exhibit a current-voltage characteristic with regions of constant current. These current steps are given by a very simple relation $I = 2e\,f$, where f is the frequency of the microwave irradiation. If this prediction is experimentally confirmed, Josephson junction chains are good candidates for the realization of a quantum current standard.

In the following paragraphs I will present measurements performed using these three biasing schemes.

5.3   Measurement of quantum phase-slips

To measure the effect of QPS on the ground state of a Josephson junction chain, we have studied a chain of six junctions. Our measurement set-up and the junction parameters are presented in Fig. 5.4 and Table 5.1. An electron beam image of the measured sample is shown in Fig. 5.5. Each junction in the chain is realized by a superconducting quantum interference device (SQUID) to enable tunable Josephson coupling E_J. In this way we can tune in situ the E_J/E_C ratio by applying a uniform magnetic flux Φ_S through all SQUIDs, and consequently we can control the strength of the QPS amplitude v (see eq. 5.2). We have used the phase biasing scheme presented in figure 5.3a and discussed in the previous section. We placed the chain in a closed superconducting loop, threaded by the flux Φ_C, containing an extra shunt Josephson junction that is used for the read-out of the chain state. The flux Φ_C enables the control of the bias phase $\gamma = \Phi_C - \delta$ over the chain. δ is the phase difference on the read-out junction. Since the Josephson energy E_J^{RO} of the read-out junction is much larger than the one of the chain, the phase difference δ is practically independent on Φ_C. In Fig. 5.5 we can see a gate electrode, capacitively coupled to the middle island of the chain. For the moment we connect this gate to the ground so that $V_G = 0$. The influence of non zero gate voltage will be discussed in the following sections (5.4 and 5.5).
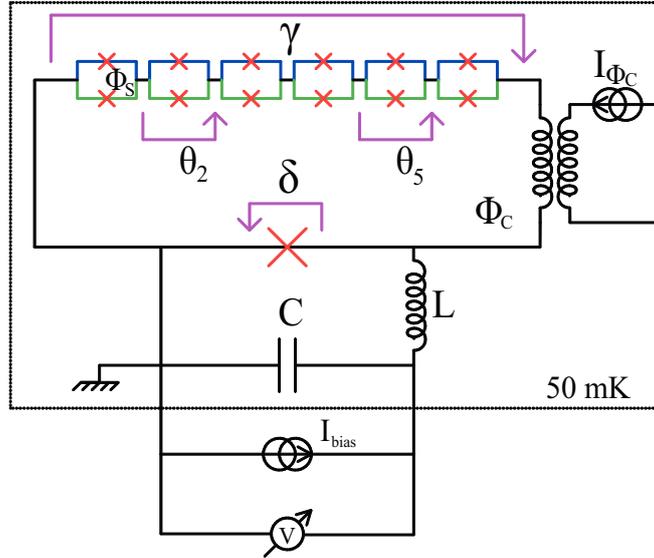
Figure 5.4: Measurement circuit. The 6-SQUID chain is inserted in a superconducting loop. The flux Φ_C created by on-chip coils controls the phase difference over the chain. The flux Φ_S through the SQUIDs can be controlled independently by a second coil. We denote the phase difference over the read-out junction δ.

We have measured the switching current of the entire Josephson junction circuit containing both the chain and the read-out junction. The switching current was determined from the switching probability at 50%. The switching probability as a function of bias current I_{bias} has a width of 20 nA. We apply typically 10^4 bias-current pulses of amplitude I_{bias} and measure the switching probability as the
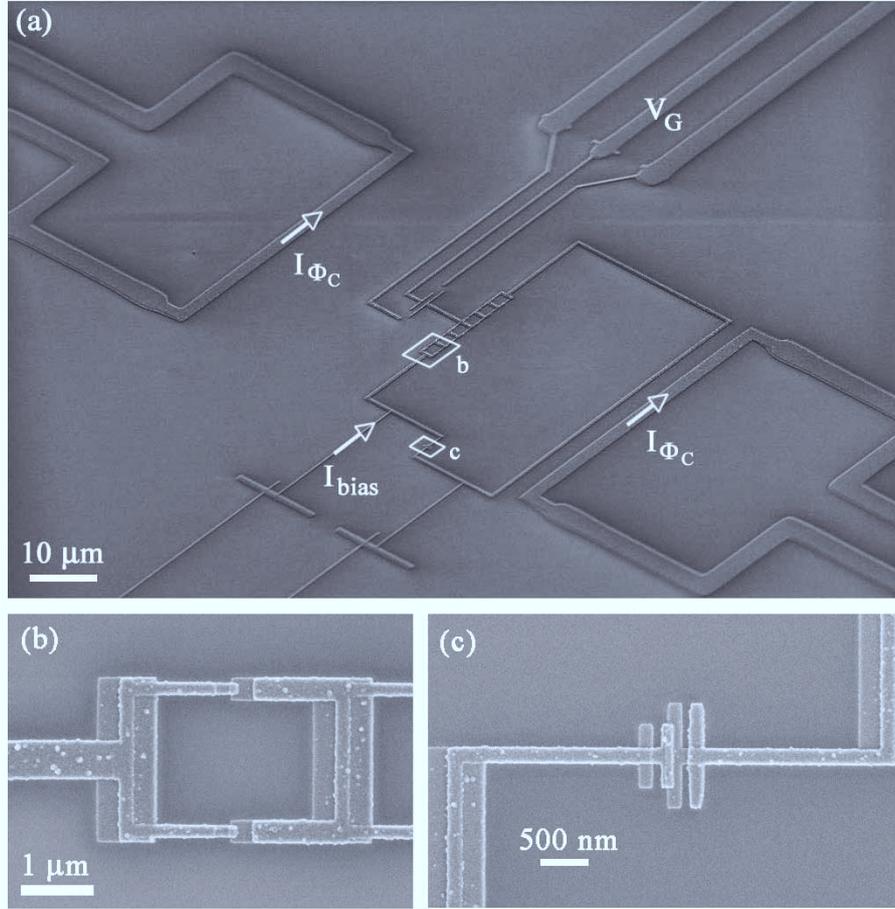
Figure 5.5: e-Beam image of the measured sample. (b) The first SQUID in the chain. (c) The read-out junction

Read-out junction	SQUID at $\Phi_S = 0$
$S^{RO} = (121 \pm 5) \times 10^3 \, nm^2$	$S^{SQ} = (30 \pm 2) \times 10^3 \, nm^2$
$C^{RO} = 5.8 \pm 0.2 \, fF$	$C^{SQ} = 1.4 \pm 0.1 \, fF$
$R_N^{RO} = 968 \pm 5 \, \Omega$	$R_N^{SQ} = 3800 \pm 450 \, \Omega$
$I_C^{RO} = 330 \pm 2 \, nA$	$I_C^{SQ} = 83 \pm 9 \, nA$

Table 5.1: Parameters of the sample: size, capacitance, normal-state resistance and critical current of the read-out junction and a single SQUID of the chain. The critical-current variance for the junctions in the chain is estimated to be smaller than 4% (see Chap. 2.5).

ratio between the number of switching events and the total number of pulses. The current pulses have a rise time of $8\,\mu s$ and a total duration of $20\,\mu s$. A detailed description of the measurement sequence is presented in chapter 3.1 . From the switching-current measurements we deduce the effect of QPS on the ground state of the chain.
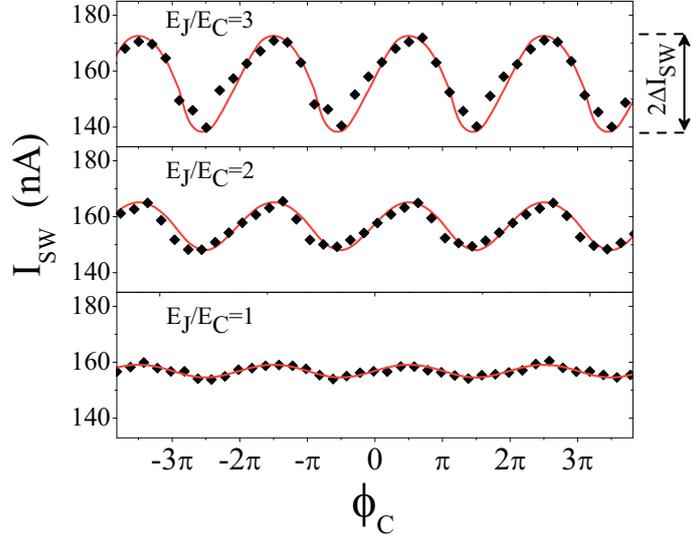
Figure 5.6: Measured switching current (black diamonds) as a function of Φ_C over the chain for three different E_J/E_C ratios. The measurement noise for each point is about $0.2\,nA$. The red lines represent the corresponding theoretical calculations for the switching current.

The measured switching current corresponds to the escape process out of the total potential energy U_{tot} containing the contributions of the read-out junction and the chain:

$$U_{tot}\left(\delta, \Phi_C\right) = E_J^{RO}\cos\delta + E_g\left(\Phi_C - \delta\right) - \frac{\hbar}{2e}I_{bias}\delta \tag{5.5}$$

Where E_g is the ground state of the 6-SQUID chain calculated by solving the Hamiltonian (5.3). The escape from the potential U_{tot} occurs by macroscopic quantum tunneling (MQT). I would like to point out that the total washboard potential (5.5) has an arbitrary shape (especially in the limit of rare phase-slips) so the usual MQT theory [10,80,81], that has been deduced for sinusoidal potentials, does not provide a sufficiently accurate description. In ref. [82] the MQT rate for an arbitrary potential has been calculated in the limit of weak tunneling using the dilute instanton-gas approximation [83]. The MQT model that we have constructed for an arbitrarily shaped potential is discussed in chapter 3.3. Knowing the escape rate, we can calculate the escape probability P_{SW} as a function of I_{bias} and infer the theoretical switching current (at $P_{SW} = 50\%$) for each polarization point Φ_C.

The results of numerical calculations and the experimental data for the 6-SQUID chain are shown in Fig. 5.6. The theory fits very well both in amplitude and shape the oscillations of the measured switching current. Let us point out that
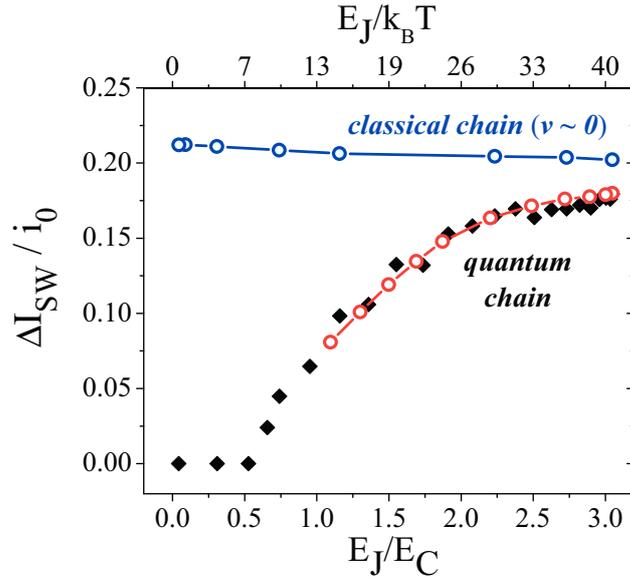
Figure 5.7: Comparison between the measured and the calculated switching-current amplitude as a function of the E_J/E_C ratio. Black diamonds: measured; red open circles: calculated. Note that the switching-current amplitude is divided by the flux-dependent critical current of a single SQUID i_0, to reveal the effect of quantum-phase fluctuations. The top curve (blue open circles) shows the theoretical calculation of the switching-current amplitude in the absence of quantum phase fluctuations. The lines are guides for the eye.

we have used the nominal values for E_J and E_C calculated from the characteristics of the sample indicated in Table 5.1. We evaluate the precision of the determination of E_J and E_C to be in the range of 10%. This error bar on E_J and E_C yields an uncertainty of 15% for the phase-slip amplitude Nv. The eventual presence of junction inhomogeneity or an important effect of background charges would imply a significantly larger decrease of the phase-slip amplitude [52]. The good agreement between theory and experiment confirms the homogeneity of our junctions. It also excludes a significant contribution of background charges in the overall shape of the switching curve and demonstrates the collective nature of the phase-slip events.

From the measurements in Fig. 5.6, we define the switching current amplitude ΔI_{SW} as half of the peak-to-peak variation of the switching current with the flux Φ_C. Figure 5.7 shows the measured ΔI_{SW} and the corresponding theoretical calculations as a function of E_J/E_C. For each measurement, E_J has been calculated using the flux dependence of the SQUID's Josephson coupling: $E_J(\Phi_S) = \frac{\hbar}{2e}i_0(\Phi_S)$ with $i_0(\Phi_S) = I_C^{SQ}\cos(\pi\Phi_S/\Phi_0)$. To distinguish between the suppression of the switching current that is due to quantum phase fluctuations and the one that is simply due to the well-known cancellation of the SQUID's critical current as a function of flux, we plot the switching-current amplitude divided by the critical current of a single SQUID i_0. We see that the measured switching-current amplitude follows very well the predicted theoretical suppression of the switching-current oscillations in the presence of quantum phase fluctuations. From our measurements we can also deduce the strength of the QPS amplitude. With decreasing E_J/E_C ratio from 3 to

1 the QPS amplitude Nv increases from 0.8 to 2.7 GHz. In addition, in Fig. 5.7 we have plotted for comparison the calculation for the switching-current amplitude in the case when quantum phase fluctuations would be negligibly small: $v \sim 0$. As expected, we get a practically flat dependence as a function of E_J/E_C.

Further on, the upper x axis of Fig. 5.7 shows the ratio E_J/k_BT of the Josephson energy with respect to the thermal energy at $T = 50\,\mathrm{mK}$. As $E_J \gg k_BT$, thermal fluctuations are excluded to explain the suppression of the switching current with decreasing E_J/E_C. Further measurements (see fig. 6.7) reveal a constant switching-current amplitude and width of the switching distribution up to a temperature of $T = 100\,\mathrm{mK}$.
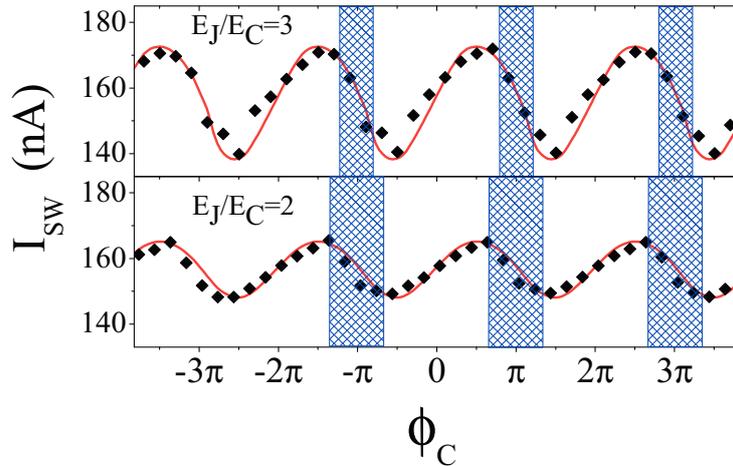

Figure 5.8: Intervals in the current-phase relation where the state of the chain is sensitive to the gate voltage (highlighted blue regions).

In conclusion, we have presented a detailed experimental characterization of the effect of QPS on the ground state of a Josephson junction chain. These phase-slips are the result of quantum phase fluctuations induced by the finite charging energy of each Josephson junction in the chain. The experimental results can be fitted in very good agreement by considering a simple tight-binding model for the phase-slips [52]. The measurements also show that a Josephson junction chain under phase-bias constraint can behave in a collective way very similar to a single macroscopic quantum object.

We can now ask what is the influence of the island's electric charges on the ground state of the chain. Sweeping the voltage V_G on the gate electrode visible in Fig. 5.5 we induce polarization charges on the islands of the chain. In fig. 5.8, the blue highlighted regions mark the phase intervals where we observe a change in the switching current of the circuit as a function of the gate voltage V_G. In the following sections we will discuss in detail the influence of the islands charges on the QPS amplitude.

5.4 Theoretical description of QPS in the presence of polarization charges

In the Matveev-Larkin-Glazman (MLG) theory [52], the main ingredient is the interference of QPS occurring in the different junctions. A direct way to probe this interference is provided by the change in the geometric phase of the QPS induced by the charge frustration of the chain islands, also known as Aharonov-Casher interference [53]. The accumulation of a geometric phase by neutral particles with a magnetic moment circling an electric charge is a physical phenomenon dual to the well known Aharonov-Bohm [112, 113] interference of charged particles circling magnetic field lines. The Aharonov-Casher model has been quantitatively confirmed by experiments using neutron [114] and atomic [115] interferometry. In solid state systems, in quantum well ring structures, conductance measurements [116] have shown fluctuations as a function of the spin-orbit coupling strength. These fluctuations are understood as a direct manifestation of the Aharonov-Casher phase. In Josephson junctions circuits, measurements of the conductivity versus a central gate voltage have shown a signature of the Aharonov-Casher interference for vortex tunneling [117]. However, due to quasiparticle poisoning, no quantitative agreement could be demonstrated.

As we have shown in the previous section, the MLG theory constructs a model for the quantum fluctuations in a Josephson chain, using a tight-binding approximation, which only couples neighboring flux states m:

$$H \left| m \right\rangle = E_m \left| m \right\rangle - v^* \left[\left| m - 1 \right\rangle + \left| m + 1 \right\rangle \right] \tag{5.6}$$

Where $E_m = \frac{E_J}{2N}(\gamma - 2\pi m)^2$ is the energy of the $\left| m \right\rangle$ state of the chain polarized at phase γ. The coupling term v^* depends on the ratio E_J/E_C, the number of junctions N in the chain and, as we will explain in the following, it also depends on the configuration of polarization charges on the islands of the chain.

The complete Hamiltonian of the Josephson chain is the following:

$$H = \frac{1}{2} \sum_{i,j} \left[C^{-1} \right]_{ij} (Q_i - q_i)(Q_j - q_j) + \sum_i E_J \left[1 - \cos \left(\varphi_i - \varphi_{i-1} \right) \right] \tag{5.7}$$

Where Q_i is the charge on the i-th island, q_i is the polarization charge and φ_i is the superconducting phase on the island. C^{-1} is the matrix of inverse capacitance of the chain and E_J is the Josephson coupling. The first sum in the expression (5.7) is the charging energy for the islands of the chain and the second sum represents the total Josephson coupling for all the junctions in the chain.

In our experimental setup (see fig. 5.5a), the charge frustration q_i on the islands is tuned by a capacitive coupled gate electrode. In Fig.5.9a we show an idealized view of a superconducting ring containing 5 islands connected by Josephson junctions. In the vicinity of the ring we find the gate electrode that can induce polarization charges q_i on the chain islands. A gate voltage V_G induces the charge frustration $q_i = C_i^g V_G/(2e)$ on the i-th island. As the couplings to the gate electrode C_i^g are not equivalent for all islands, for a certain gate voltage, we will induce a charge

configuration that will generally be denoted in the following way: $(q_1, q_2, q_3, q_4, q_5)$. The white traces in Fig.5.9a represent the 6 possible paths for a vortex to cross the ring, through one of the 6 Josephson junctions. The mathematical expressions for the corresponding QPS probability amplitudes are also shown for each path. Notice that the amplitudes differ only by the geometric (Aharonov-Casher) phase, which is proportional to the induced charge frustrations q_i on the islands. In the next paragraphs,we will discuss the origin and the physical significance of these geometrical phases.

Here we present the detailed derivation of the hopping term v^* of the MLG model in the charge frustrated chain. Similar calculations have been performed for the Josephson chain [52] and for slightly different Josephson circuits [54, 118]. To calculate the hopping term we need to find the classical trajectories connecting states before and after one phase-slip event. There are N such trajectories, each of them corresponding to the phase-slip occurring on a particular junction in the chain. In a semi classical approximation, the contribution of the phase-slip in the junction i to the hopping term is governed by the imaginary-time action S_i:

$$v_i = A e^{-S_i} \tag{5.8}$$

The prefactor A accounts for the contribution of the non-classical paths close to the classical one that defines S_i.

In order to calculate the actions S_i, we need to derive the complete Lagrangian for the Josephson chain. The electrostatic effects in the Josephson chain are described by the following Hamiltonian:

$$H_C = \frac{1}{2} \sum_{i,j} \left[C^{-1} \right]_{ij} (Q_i - q_i)(Q_j - q_j) \tag{5.9}$$

The polarization charges $q_i = \frac{C_i^g V_g}{2e}$ are controlled by the gate voltage, as depicted in Fig. 5.9b. We would like to mention that in our experimental setup we have added screening lines to the central gate, in order to obtain a coupling to the central island at least 10 times larger than the couplings to the rest of the chain: $C_3^g \simeq 10 * C_4^g, C_2^g \simeq 50 * C_1^g, C_5^g$.

Since the charges Q_i and the phases of the islands φ_i are canonical conjugate variables, the equation of motion for the phase reads:

$$\dot{\varphi}_i = \frac{\partial H_C}{\partial Q_i} = \sum_j \left[C^{-1} \right]_{ij} (Q_j - q_j) \implies Q_i = \sum_j C_{ij} \dot{\varphi}_j + q_i \tag{5.10}$$

Using eq. (5.10) we can rewrite the charging Hamiltonian (5.9) in the phase notation:

$$H_C = \frac{1}{2} \sum_{i,j} C_{ij} \dot{\varphi}_i \dot{\varphi}_j \tag{5.11}$$

The charge part of the Lagrangian for the Josephson junction chain reads:

$$\mathcal{L}_C = \sum_i Q_i \dot{\varphi}_i - H_C \tag{5.12}$$
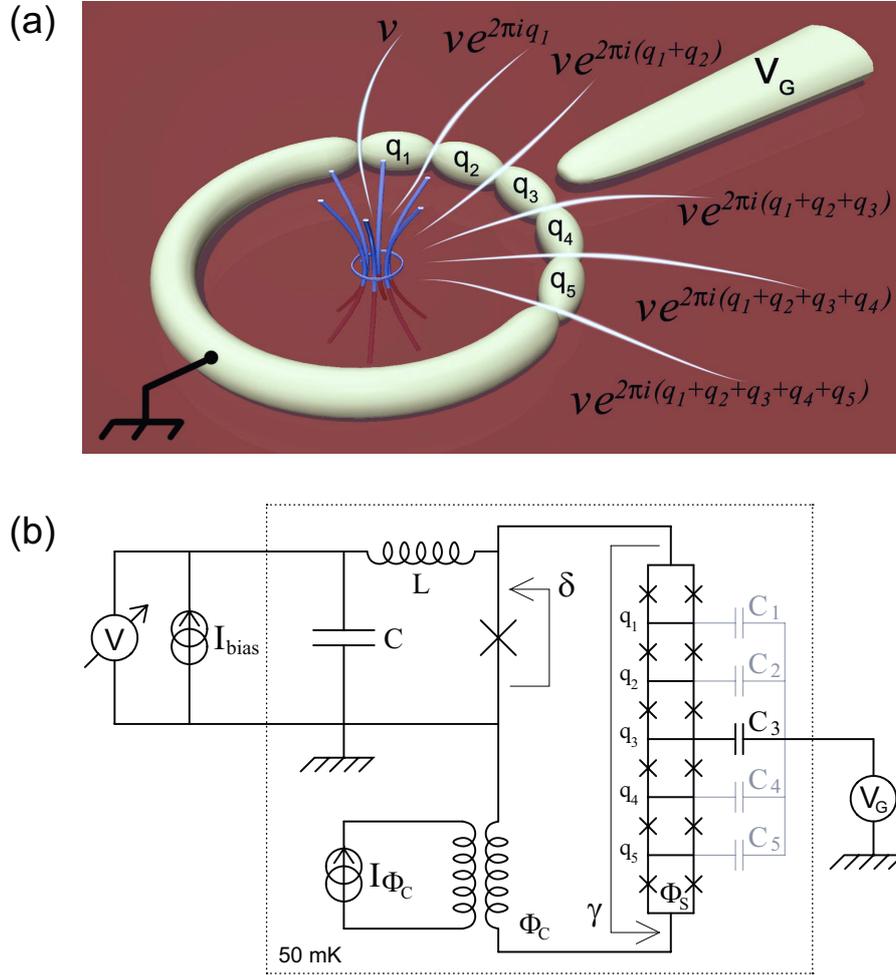
Figure 5.9: Schematic view of the experimental setup used to probe the QPS interference in a chain of 6 Josephson junctions. In (a) we show an idealized view of the experimental design. The chain contains 5 small superconducting islands connected to each other and to the leads by identical Josephson junctions. The islands are coupled to a nearby gate electrode. In (b) we present the electrical scheme of the measurement. The 6-SQUID chain is inserted in a superconducting loop. The flux Φ_C created by on-chip coils controls the phase difference γ over the chain. The independently controlled flux Φ_s through the SQUID loops is used to tune *in situ* the ratio E_J/E_C. The phase difference over the read-out junction is denoted by δ. The gate electrode couples to the charge q_i on island i via the capacitance C_i^g. The coupling to the central island C_3^g is at least 10 times larger than all other capacitances and determines the dominant gate effect at low voltage.

Following formula (5.12) and using the expressions (5.10) and (5.11) we get for the charge Lagrangian the following expression:

$$\mathcal{L}_\mathcal{C} = \sum_{ij} C_{ij} \dot\varphi_i \dot\varphi_j + \sum_i q_i \dot\varphi_i - \frac{1}{2} \sum_{ij} C_{ij} \dot\varphi_i \dot\varphi_j$$

$$\mathcal{L}_\mathcal{C} = \frac{1}{2} \sum_{ij} C_{ij} \dot\varphi_i \dot\varphi_j + \sum_i q_i \dot\varphi_i \tag{5.13}$$

The capacitance matrix C_{ij} contains the values of all coupling between the islands. However, in reality, due to the geometry of the sample, the capacitance between first neighbors is orders of magnitude larger then the stray capacitance between second order neighbors. This means that we can safely work within the so called *nearest neighbor capacitance* approximation, and the matrix C_{ij} only gets non zero contributions for the elements closest to the main diagonal:

$$\begin{pmatrix} 2C & -C & 0 & ... & 0 \\ -C & 2C & -C & ... & 0 \\ 0 & -C & 2C & ... & 0 \\ ... & ... & ... & ... & -C \\ 0 & 0 & 0 & -C & 2C \end{pmatrix} \tag{5.14}$$

Where C is the capacitance of one junction in the chain.

Using the approximation (5.14) the expression of the charge Lagrangian is simplified and it reads:

$$\mathcal{L}_\mathcal{C} = \frac{1}{2} \sum_i C(\dot\varphi_i - \dot\varphi_{i-1})^2 + \sum_i q_i \dot\varphi_i \tag{5.15}$$

Introducing the phase differences on the junctions $\theta_i = \varphi_{i+1} - \varphi_i$ and including the Josephson energy, we derive the complete Lagrangian of the chain:

$$\mathcal{L} = \sum_i \left[\frac{(\dot\theta_i)^2}{16E_C} - E_J \cos\theta_i \right] - \sum_i p_i \dot\theta_i \,, \qquad p_i = \sum_{j=1}^{i-1} q_i \tag{5.16}$$

We can see that the Lagrangian (5.16) has two components which have very different physical consequences. The first sum that we call $\mathcal{L}_0$ is independent on the frustration charges q_i. It gives a contribution to the real part of the phase-slip amplitude v_i, that is given by the Bloch band width (cf. eq. 5.2). For identical junctions in the chain, the real part of v_i is independent on the path chosen by the phase-slip. The second sum of the Lagrangian (5.16), which we call $\delta\mathcal{L}$, has the form of a total time derivative. Hence, this term does not change the classical equations of motion and the real part of the classical action on a single trajectory. However, $\delta\mathcal{L}$ gives the tunneling amplitude along each path its own phase factor. When a phase-slip occurs on junction i, the other phase differences θ_j are changed by:

$$\Delta\theta_j = -\frac{2\pi}{N} + 2\pi\delta_{ij} \tag{5.17}$$

Thus, the contribution to the phase-slip action from the *j-th* junction in the presence of charge frustration reads:

$$\delta S_j = -i \int \delta\mathcal{L}\, dt = -i \sum_k p_k \Delta\theta_k = -2\pi i p_j - \frac{2\pi i}{N} \sum_k p_k \tag{5.18}$$

Since the last term in the expression above does not depend on j, it only adds an overall phase term for the total phase-slip amplitude, thus has no physical effect on the interference pattern and it can be dropped. Replacing this result in the formula (5.8), we get the mathematical expression for the charge frustration dephasing factor in the phase-slip probability amplitude of the *j-th* junction:

$$\delta v_j = e^{i2\pi p_j} \tag{5.19}$$

Combining equations (5.2) and (5.19), the phase-slip probability amplitude on the *j-th* junction v_j reads:

$$v_j = v\,exp\left[i2\pi \sum_{k=1}^{j-1} q_k\right] \tag{5.20}$$

In other words, the absolute value of the probability amplitude for the QPS is the same as in the absence of charge frustration, but the geometric phase difference between the QPS is proportional to the total charge on the islands between the junctions (see Fig. 5.9a). Finally, the full hopping term between the states $|m\rangle$ and $|m+1\rangle$ in the presence of charge frustration is the sum of phase-slip amplitudes v_i in all six junctions:

$$v^* = \sum_{i=1}^{6} v_i \tag{5.21}$$

At zero gate voltage, the expression (5.21) reduces to $v^* = Nv$ that was used in the previous section to solve the Hamiltonian (5.3) and calculate the expected switching current represented in fig. 5.6 and fig. 5.7. Non-zero gate voltage directly affects the interference of QPS by changing the geometrical (Aharonov-Casher) phase difference between phase-slips in different junctions and thus provides a direct test for the quantum nature of the chain's ground state. By introducing the hopping term v^* into the tight binding Hamiltonian (5.6), we can obtain in principle the full theoretical description of the charge frustrated chain, which can be used to compare with the experimental data. However, in a real experiment, the gate voltage V_g is not the only source of charge frustration. We should always expect a significant contribution from random offset charges q_i^0:

$$q_i = \frac{C_i^g V_g}{2e} + q_i^0 \tag{5.22}$$

Static offset charges may significantly change the precise form of the response of the chain to the gate voltage. Dynamical fluctuations of the offset charges which are also expected, complicate the situation even more. If the random dynamics of stray charges would occur on the same timescale with the time needed to acquire one experimental point, then any gate dependence would be washed out. As we will show, the very fact that a significant gate effect is observed means that the random charge dynamics is much slower than the typical time needed for one experimental data point.

# 5.5 Measurement of Aharonov-Casher QPS interference
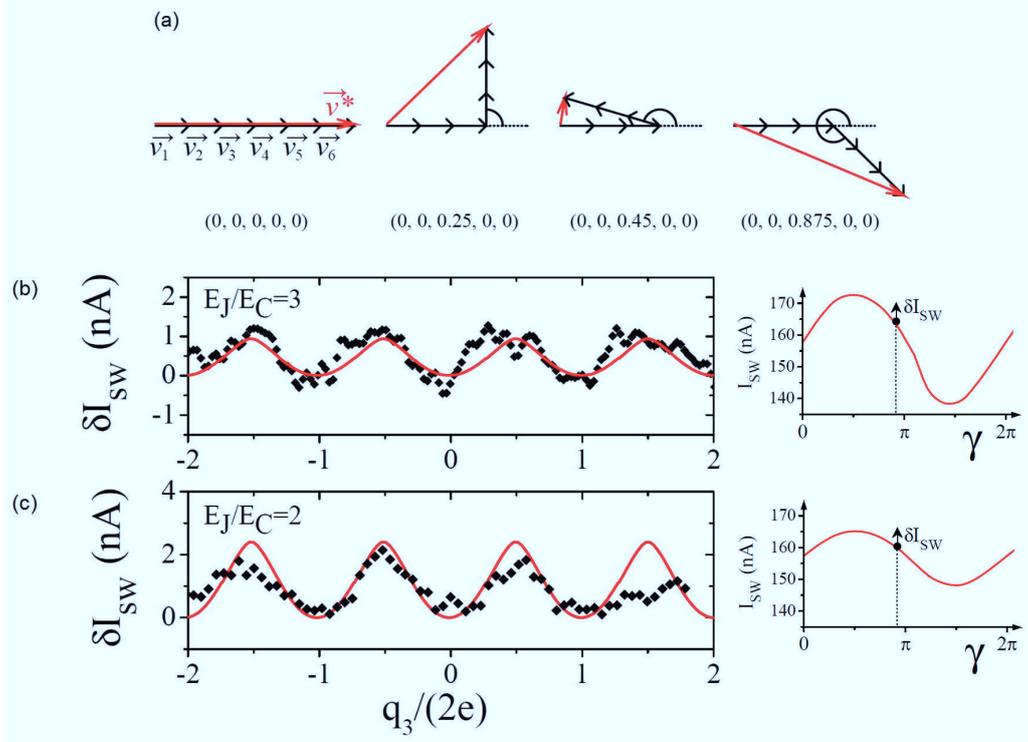
Figure 5.10: QPS interferences controlled by the polarization charge induced on the middle island of a 6 Josephson junction chain. (a) Schematic representations of the 6 phase-slip probability amplitudes v_i (in black) and the total QPS amplitude v^* (in red) as vectors in the complex plane. We show the representations of the phase-slips in the case of four different charge configurations. The corresponding charge configurations (shown in the figure) only differ by the charge on the middle island. (b) (c) The black diamonds represent the measurement of the variation of the switching current as a function of the induced charge on the middle island, in the case of $E_J/E_C = 3$ (b) and $E_J/E_C = 2$ (c). The red lines represent the corresponding theoretical calculations using the MLG model of QPS interference. The chain was phase biased at a constant phase: $\gamma = 0.9\,\pi$. The working points for the measurements presented in (b) and (c) are presented in the insets at the right of each curve. The zero of the y axis corresponds to the switching current of the zero charge configuration $(0, 0, 0, 0, 0)$.

In the following we look in detail at a particularly simple case, where we only induce charges on the middle island, thus obtaining the following charge configuration: $(0, 0, \frac{C_3^g V_g}{2e}, 0, 0)$. In order to work in this this regime, we use the fact that the central coupling C_3^g is ~ 10 times larger than any other coupling and we limit the absolute value of the gate voltage to: $|V_G| \ll 2e/C_4^g$. The charge frustration on the middle island introduces a geometrical dephasing factor $exp\,[i2\pi q_3]$ between the three QPS occurring on the junctions at the left of the middle island and the

three QPS on the junctions at the right of the middle island. This dephasing process is graphically represented for several charge configurations in Fig. 5.10a. The expression (5.21) for the total QPS amplitude as a function of gate voltage when we couple only to the central island can be rewritten in a simplified form:

$$|v*| = 3v\sqrt{2 + 2\cos\left(\frac{\pi C_3^g}{e}V_g\right)} \tag{5.23}$$

Notice that from the expression (5.23), we expect $v^* = 0$ for the charge configuration $(0, 0, 0.5, 0, 0)$ and $v^* = 6v$ for $(0, 0, 0, 0, 0)$. We can now inject the expression (5.23) for v^* in the tight binding Hamiltonian (5.6) and calculate the dependence of the chain's ground state on the charge induced on the middle island. In order to compare the measurements with the theoretical predictions for the switching current, we need to go through one more step. As discussed in section 5.3, we have to calculate the expected switching current of the read-out junction plus the ground state of the chain (see eq. (5.5)), using the MQT equations for the arbitrary shaped washboard potential (chapter 3.3). In Fig. 5.10 b and c, we show the experimental results and the calculated oscillations of the switching current δI_{SW} as a function of the charge induced on the middle island q_3. For simplicity, in the definition of the switching current δI_{SW}, we subtracted the value of the switching current corresponding to the zero charge configuration $(0, 0, 0, 0, 0)$. Around the charge configuration $(0, 0, 0.5, 0, 0)$ we expect a complete suppression of the total phase-slip amplitude v^* (see Fig. 5.10a), hence an increase of the supercurrent through the chain. The expected change in the measured switching current due to the complete suppression of phase-slips is $\sim 1\,\text{nA}$ for $E_J/E_C = 3$. If we increase the strength of QPS by decreasing the ratio $E_J/E_C = 2$, the complete suppression of QPS by maximal charge frustration increases the switching current by almost $3\,\text{nA}$ (see Fig. 5.10c).

In the case of both experimental curves presented in Fig. 5.10c, we have corrected small horizontal shifts of the x-axis in order to compensate for static random offset charges. However, we would like to mention that the corrections are small, in the range of $\sim 0.2\,(2e)$. Also, as it is visible from the shape of the curves, the charge configuration does not change during the measurement. It is important to stress this fact, as each measurement point implies 10^4 repeated switchings into the dissipative state of the junctions. At every switching event, large numbers of quasiparticles are excited in the circuit. The periodic dependence of the measured switching current and the quantitative agreement with the theoretical predictions show that after each switching event (that practically resets the charge configuration) the chain relaxes back into the same charge state as before the switching. Moreover, we have directly measured the frequency of random charge jumps (see fig. 5.13), by repeating the same measurement several times and we observe a typical time of ~ 5 minutes between changes in the island charge configuration. This time interval is sufficient in our case as it enables the measurement of several hundreds of experimental data points. Similar offset charge dynamics has been reported in experiments on Cooper pair pumping [47].

We now go on to discuss more complex interferences of QPS, induced by the charge on the central island and the two neighboring islands: q_2, q_3, $q_4 \neq 0$. We

discuss the following charge configurations:

$$(0, \frac{C_2^g V_g}{2e}, \frac{C_3^g V_g}{2e}, \frac{C_4^g V_g}{2e}, 0) \tag{5.24}$$

This regime is experimentally obtained for gate voltages $|V_G| \gtrsim 2e/C_4^g$. In this range of gate voltage, we induce a polarization charge of about $2e$ on the lateral islands q_2, q_4 and a charge of several tens of Cooper pairs on the central island q_3. In our discussion we will use the fact that the hopping term v^* remains constant upon the change of the islands charge by an integer number n of Cooper pairs: $q_i \to q_i \pm n$. The polarization charges are effectively defined modulo $2e$.
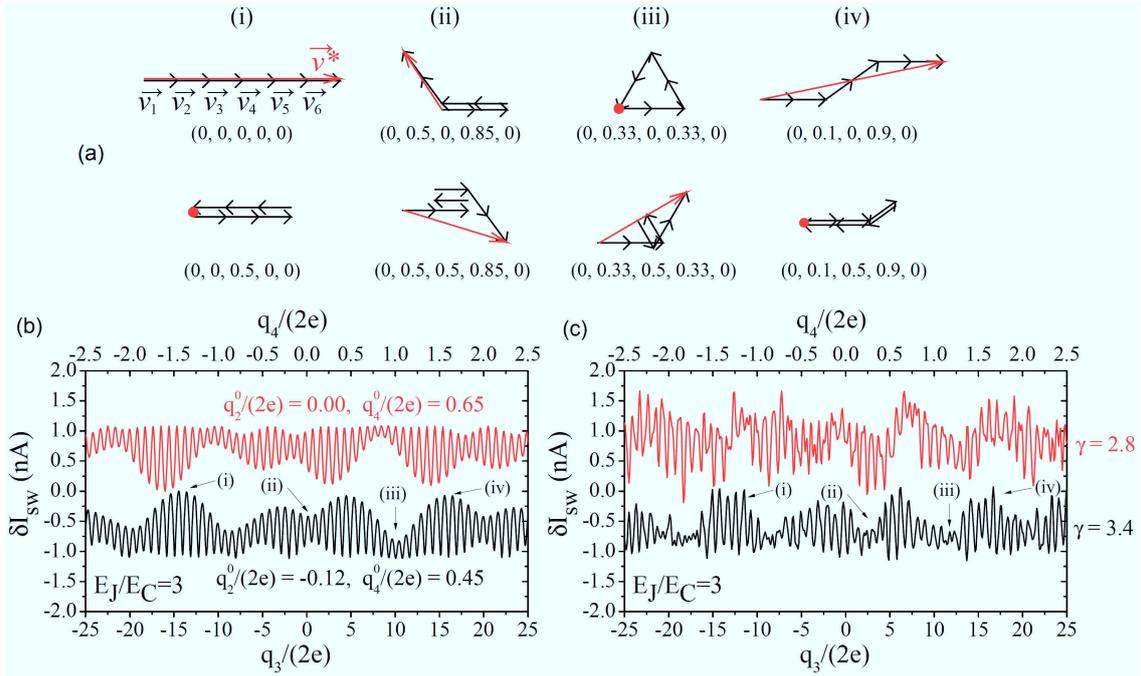

Figure 5.11: QPS interferences induced by the polarization charge on the middle and the first two lateral islands $(0, q_2, q_3, q_4, 0)$ of the 6 Josephson junction chain at $E_J/E_C = 3$. (a) Schematic representations of the 6 phase-slip probability amplitudes v_i (in black) and the total QPS amplitude $v*$ (in red) as vectors in the complex plane, for several particularly chosen charge configurations. (b) The calculated switching current change induced by the polarization charges δI_{SW} for a large sweep of the gate voltage V_G, at two different phase-biases. The polarization charge on the central island q_3 is shown on the lower x-axis and the charge on one of the lateral islands q_4 is shown on the higher x-axis. (c) The measured δI_{SW} over a large sweep of V_G at the same phase-biases γ as in (b). The value of γ for each curve is shown on the right side of the figure.

The charge frustration on the middle and on the first two lateral islands introduces geometrical dephasing factors between the QPS on each side of the second, third and forth junctions. In Fig. 5.11a we represent the QPS as vectors in the complex plane, for several particular charge configurations. Simply by looking at Fig. 5.11a we can immediately see that the two extra degrees of freedom from

γ	$q_2^0(2e)$	$q_4^0(2e)$	$C_2^g(aF)$	$C_3^g(aF)$	$C_4^g(aF)$
0.9π	0	0.65	25	410	42
1.1π	-0.12	0.45			

Table 5.2: Fit parameters for the calculated QPS interference patterns presented in Fig. 5.11b. The fited values for the gate capacitances are close to the theoretically estimated values (see appendix B), taking into account the exact geometry of the sample. The value for C_3^g is also confirmed by the FFT of the measured oscillations as a function of temperature (Fig. 5.12).

the lateral islands add considerable complexity to the interference pattern. Thus, we expect the switching current oscillations δI_{SW}, induced by a large gate voltage sweep, to show a complex pattern, composed of a fast oscillation arising from the strong C_3^g coupling and a slower evolving envelope due to the weaker C_2^g and C_4^g couplings. In Fig. 5.11c we show the measured interference patterns at two different phase biases γ of the Josephson junction chain. The two phase biases are chosen close to $\gamma = \pi$ where the response of the chain is maximal. In Fig. 5.11b we present the calculated interference patterns for the same phase bias. For the top curves in Fig. 5.11b and c we polarized the chain at $\gamma \lesssim \pi$ so we expect the switching current to increase when the phase-slips are suppressed. Similarly, for the bottom curves, where $\gamma \gtrsim \pi$, we expect the switching current to decrease when the chain becomes classical. Also, the exact shape of the oscillations envelope strongly depends on the configuration of offset charges. For the two calculated curves we have chosen the offset charges configurations leading to the best fit of the experimental data. The exact values of the fit parameters are shown in table. 5.2.

The positions of the four particular charge configurations detailed in Fig. 5.11a are indicated on the measured and calculated curves. Point (i) corresponds to the same situation detailed in Fig. 5.10a. Its position is shifted on the *x axis* by the offset charges on the islands 2 and 4. The fitted values for the offset charges q_2^0 and q_4^0 are indicated in Fig. 5.11b for each curve. The absolute value of the total QPS amplitude $|v^*|$ oscillates between 0 and Nv, according to the formula (5.23). The resulting switching current δI_{SW} oscillations have the largest amplitude possible. The chain goes from the perfectly coherent phase-slips regime at $q_3 = 0$, where the switching current is minimum (the zero level in Fig. 5.10b and c), to the maximally dephased configuration at $q_3 = 0.5$ when the phase-slips are canceled, the chain is classical and the critical current is enhanced. Point (ii) is interesting as it depicts the situation when $|v^*|$ never goes neither to zero nor to the maximum value of Nv, independent on the value of the charge q_3. In this case, we expect some small amplitude oscillations situated somewhere in the middle of the interval spanned by the maximum and the minimum of the oscillations from the point (i). Working point (iii) shows the situation when the total QPS amplitude is suppressed at $q_3 = 0$ and it never reaches the maximum Nv for any value of q_3. In this case we expect small oscillations of δI_{SW} that reach the maximum supercurrent for the classical chain. In the case depicted for the point (iv) we show that it is not necessary to have the QPS perfectly aligned as in (i) in order to have a significant amplitude of δI_{SW} oscillations. We see that the δI_{SW} oscillations in (iv) are comparable in amplitude

to the ones around point (i).
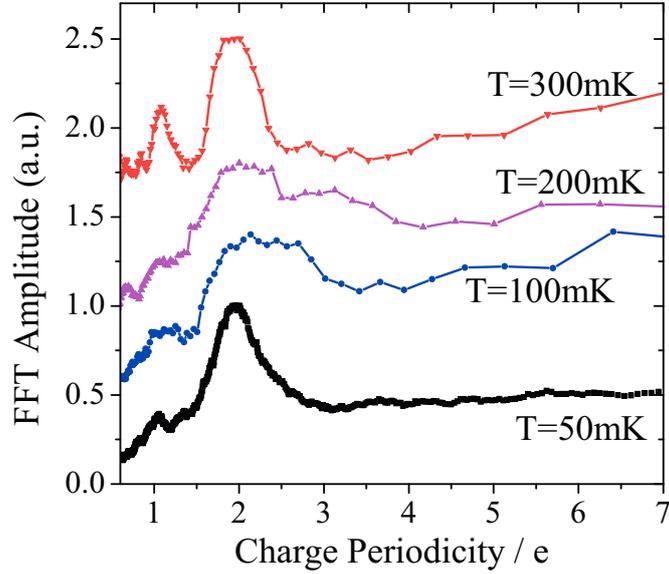
Figure 5.12: Temperature dependence for the periodicity of the switching current *vs.* charge oscillations. We present four plots of fast Fourier transforms (FFT) for the measured switching current oscillations at different temperatures. The carge periodicity represented on the *x-axis* is calculated for $C_3^g = 410\,aF$. At low temperatures the periodicity is $2e$. At temperatures close to $300\,mK$ we observe the emergence of a significant $1e$ periodicity peak. The small peak at $1e$ visible at low temperature is associated with the anharmonicity of the measured switching current oscillations. The curves are offset on the *y-axys* for clarity.

The Aharonov-Casher interference of phase-slips is an intrinsically $2e$ periodic effect, as explained in fig. 5.10. Random $1e$ quasiparticle poisoning of the islands can prove to be a significant experimental problem [117]. This $1e$ contamination practically reduces the accessible charge space interval from $[0, 2e]$ to $[0, 1e]$. The consequences of the quasiparticle poisoning are the observation of a significantly reduced amplitude of the interference pattern and a periodicity of $1e$ instead of $2e$ for the interference fringes.

The exact value of the gate coupling is very difficult to evaluate numerically with a sufficient accuracy to distinguish $1e$ from $2e$ periodicity (Appendix B). The best proof of $2e$ periodicity at low temperatures is the emergence of $1e$ periodicity at higher temperatures, when we strongly excite quasiparticles. In fig. 5.12 we present the fast Fourier transforms (FFT) for interference patterns measured at different temperatures. We see that at low temperatures ($T = 50\,\mathrm{mK}$) the main peak in the FFT is at $2e$ periodicity. With increasing temperature, at ($T = 300\,\mathrm{mK}$), a quasiparticle peak at periodicity $1e$ emerges.

Another experimental challenge in the measurement of the charge response of the chain was the stability of the random offset charges. In figure 5.13 we show repeated measurement of the same gate voltage V_G interval. We observe a typical
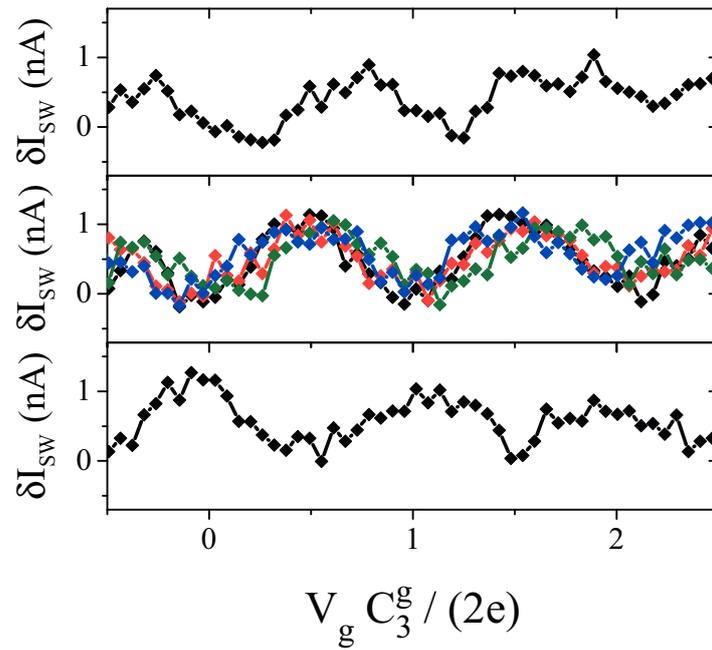
Figure 5.13: Repeated measurements on the same gate voltage interval. The gate coupling is $C_3^g = 410\,aF$. The four curves in the middle graph are grouped together as they correspond to the same offset charge configuration. The curves are measured successively starting from the top plot. The time interval between the measurements is ~ 5 minutes. We see that after the first measurement the offset charge changed. For the next four curves the offset charges remain fixed. Before the last measurement the charges drift again.

offset charge reset time of ~ 5 minutes. Thus, if we measure an interference curve in a total time interval shorter than a few minutes we have good chances to do a measurement with fixed offset charge configuration, as shown for example in fig. 5.11.

In conclusion, the switching current measurements show that the ground state of the 6-SQUIDs chain is sensitive to the configuration of charges on the islands, in quantitative agreement with the MLG model. The sensitivity is limited to an interval of phases γ around π. The shape of the switching current oscillations as a function of the induced charges on the islands can be quantitatively understood as a phase-slip interference pattern. Two phase-slip amplitudes on different junctions can add constructively or destructively, depending on the total charge on the superconducting islands between the junctions. This effect is a direct manifestation of the Aharonov-Casher model for the interference of magnetic moments circling a charged particle.

5.6 Phase-slips in a voltage biased 400 Josephson junction chain

Our experimental work is motivated by recent theoretical results of W. Guichard and F. Hekking (see ref. [51]). They show that in a long chain of Josephson junctions the dynamics of the quasicharge is exactly dual to the standard phase dynamics of a single Josephson junction. The quasicharge-phase duality has already been experimentally observed for a Josephson junction embedded in a high impedance environment [104]. The high impedance environment is essential for the localization of the quasicharge. In ref. [51] it has been shown that the resistive environment can be replaced by a large inductance. As experimentally it is not simple to fabricate a junction in series with a large inductance, we investigate an alternative route. A chain of Josephson junctions, each of them having a large E_J/E_C-ratio, also constitutes a phase-slip element. The central idea is that the phase-slip itself occurs on only one of the junctions of the chain; the phases on the other junctions perform small adjustments in the Josephson potential, thereby providing the necessary inductance. Further on, as we have shown in the previous sections, in the absence of offset charges, the total phase-slip amplitude v^* is N times the phase-slip amplitude for one junction: $v^* = Nv$. The longer the chain is, the larger its inductance and the total phase-slip amplitude. The chain realises a zero current state, that is interesting to study.

We have measured a chain of $N = 400$ junctions. Given the large number of junctions, within the MLG model of QPS, we expect a very strong phase-slip amplitude and consequently a suppression of superconductivity. Experimentally, we expect to measure an insulating state for the chain biased at voltages inferior to the so called critical voltage: $V_C = N \frac{\pi \Delta}{e}$ [51]. We will use the phase biasing scheme presented in Fig. 5.3c, in order to try to directly measure the critical voltage.

The chain is biased at a voltage V and we measure the electrical current I. The electrical scheme of the setup is presented in Fig. 5.14. The sample is thermally connected to the cold plate of the dilution refrigerator at a temperature of $\sim 50\,\text{mK}$.
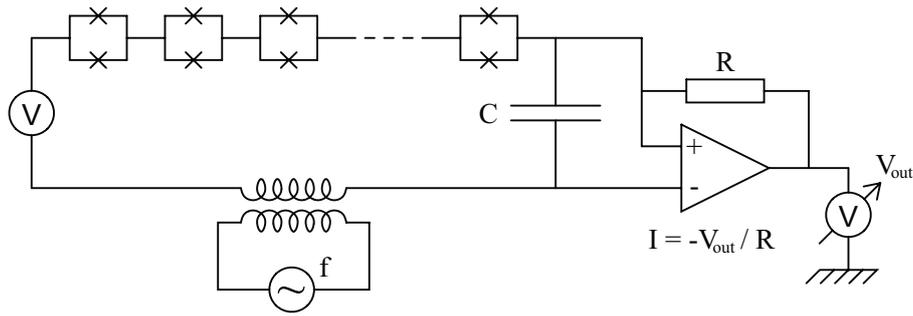
Figure 5.14: Electrical scheme of the voltage biased Josephson chain.

The current amplifier and the voltage source are at room temperature, isolated from the sample by low band filters at the entrance of the cryostat. In order to reduce the electromagnetic noise, special care has been taken to avoid ground loops and to shield the sample from any radiation source. The junctions are fabricated in the form of SQUIDs in order to enable tunable Josephson coupling E_J. At zero flux ϕ inside the SQUID loops $E_J = 3.3\,\mathrm{K}$ and $E_J/E_C = 20$. From the MLG model, we expect a critical voltage $V_C \sim 100\,\mu\mathrm{eV}$.

The results of the IV measurements for the 400 junctions chain are shown in Fig. 5.15. Surprisingly, we do not observe any insulating region. At low voltage we observe a low dissipation current branch that peaks around $20\,\mathrm{nA}$. Moreover, we observe a sequence of periodic current peaks with the voltage periodicity close to the value of the Aluminum superconducting gap. A similar periodic current peaks structure has been reported for Josephson junction chains by D. Haviland in ref. [119]. We do not have a quantitative understanding of these structures. We think that they are signatures of the voltage bias dropping on the weakest junction in the chain, rather than distributing on the entire chain. Within this model, at small voltage bias the phase-slips are distributed on the entire chain and the current-voltage characteristic is linear. With increasing voltage, at a critical value $V \simeq 50\,\mu\mathrm{V}$, the phase-slips localize on the weakest junction in the chain and block the conduction, so the current in the IV characteristic drops. When the voltage reaches the value of the gap, the junction switches to the dissipative state, so the conduction increases again and phase slips redistribute on the entire chain. With increasing voltage, this process has the periodicity of the superconducting gap $\Delta \simeq 420\,\mu\mathrm{V}$.

We observe a linear IV characteristic in the vicinity of zero bias (see Fig. 5.15b). At a voltage around $V = \pm 50\,\mu\mathrm{V}$ the system switches to a lower current state. When we sweep the voltage in the opposite direction, going towards zero voltage, we observe that the switching to the linear regime does not occur at the same value, so we measure a hysteresis. The linear part in the IV curve is associated with the tunneling of Cooper pairs through the junctions and dissipation in the environment of the sample. This dependence was predicted theoretically [120] and measured [121] in a superconducting transistor. At this point we do not have a quantitative understanding of the measured IV curves.

In the following we will propose a simple explanation for the absence of the
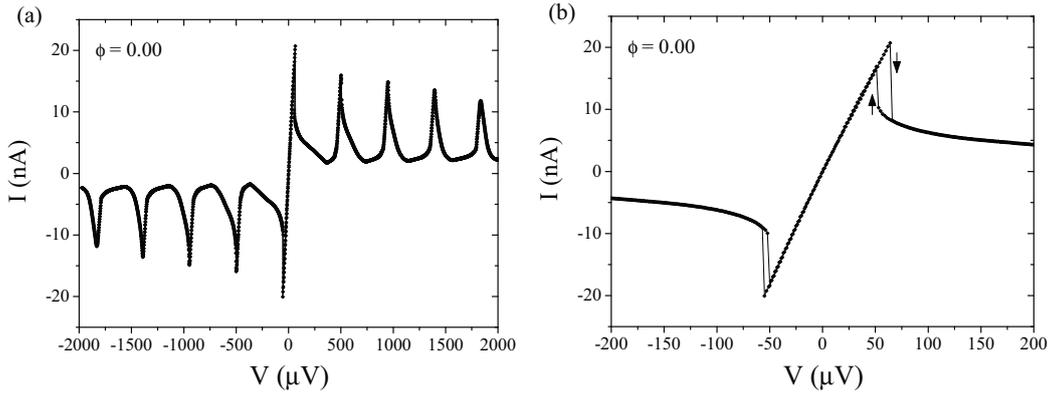
Figure 5.15: (a) Typical measured current *vs* voltage curve. (b) Zoom in the low voltage region.

insulator region predicted by the MLG model. In the MLG model we have neglected the self capacitance of the islands C_0. We had very good reasons to do so as the junction capacitances C are much larger than the stray coupling of the islands: $C \gg C_0$. But if the number of junctions N in the chain is large, the island couplings C_0 which add in parallel their contributions can no longer be ignored. In the next section we discuss these classical electromagnetic effects present in long Josephson chains. Previously neglected in the MLG model, they can play a dominant role for long Josephson chains.

5.7 Standing electromagnetic waves in a 400 Josephson junction chain

In this chapter, we will discuss a simple harmonic model [122] that quantifies the effect of the self capacitances C_0 on the ground state of the chain. As we will see in the following, we can define some characteristic length scale N^* for the chain, called the screening length. For $N < N^*$ the MLG model is valid and we can continue to neglect the existence of C_0. However, for $N > N^*$ the phase-slip amplitude will not be independent on C_0.

Before we continue with the description of the model, we would like to point out the following fact. The self capacitances of the islands C_0 are always non zero. An island, that is a small piece of some material, will always have a capacitive coupling with respect to infinity, even in vacuum and far from any electrodes. Of course, by engineering the island shape and its environment, we can minimize this coupling. But it will never be zero and thus, there will always be a maximum length N^* above which the effect of C_0 must be taken into account.

In the limit $E_J/E_C \gg 1$ and $N \gg 1$, we can assume the phase difference between the neighboring islands is small and we can expand the Josephson relation for the junctions in the lowest order:

$$i_j = i_0 \sin \left(\varphi_j - \varphi_{j-1} \right) \simeq i_0 \left(\varphi_j - \varphi_{j-1} \right) \tag{5.25}$$

Here i_j is the current flowing through the $j-th$ junction, i_0 is the critical current of one junction and φ_j is the superconducting phase of the island j. Within this approximation, we can replace the Josephson elements in the chain with linear inductances. The simplest model that approximates the chain of Josephson junctions with non zero capacitances to the ground C_0 is an array of harmonic oscillators, as shown in fig. 5.16.
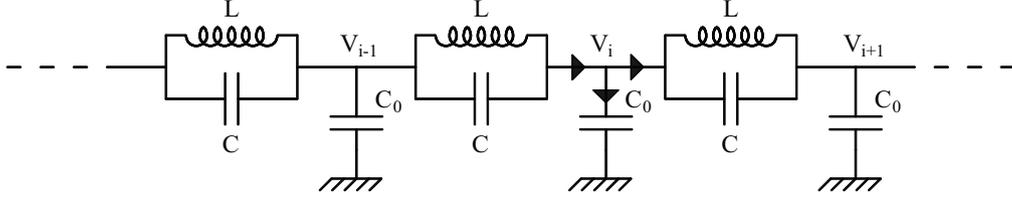

Figure 5.16: Harmonic model for the Josephson junction array with non-zero capacitive coupling to the ground. The arrows represent our notations for the electrical currents entering and leaving the island i.

In fig. 5.16 we have denoted by V_j the electrostatic potential of the $j-th$ island. The inductance L is the Josephson inductance of one junction in the harmonic limit: $L = \hbar/(2e\,i_0)$. The Kirchhoff circuit laws for each elementary cell of the chain are the following:

$$(V_j - V_{j-1})\,Y = (V_{j+1} - V_j)\,Y - i\omega C_0 V_j \quad and \quad Y = \frac{1 - LC\omega^2}{i\omega L} \qquad (5.26)$$

Here Y is the admittance of an LC block at frequency ω. Equation (5.26) has solutions of the type:

$$V_j \sim e^{ikj} \qquad (5.27)$$

which are propagating waves with k being the wave vector: $k = 2\pi n/N$. If we replace (5.27) in (5.26), we get:

$$\omega = \omega_0 \sqrt{\frac{1 - \cos k}{1 - \cos k + \frac{1}{2}\frac{C_0}{C}}} \qquad (5.28)$$

Where $\omega_0 = 1/\sqrt{LC}$ is the plasma frequency of one junction in the chain.

In order to get a clear physical image of the implications of eq. (5.28), let us consider two limits:

(a) $C_0 \gg C$:

In this limit C_0/C is very large, it is the dominant term in eq. (5.28), which can be linearized in k:

$$\omega = k\,\frac{1}{\sqrt{LC_0}} \qquad (5.29)$$

Eq. (5.29) describes propagating waves in the chain with an effective "light velocity" $c_{eff} = \frac{a}{\sqrt{LC_0}}$, where a is the lattice constant.

(b) $C \gg C_0$:

In this limit $C_0 \to 0$ so eq. (5.28) simply reads:

$$\omega = \omega_0 \tag{5.30}$$

which describes a harmonic oscillator with frequency equal to the plasma frequency of one junction: $\omega_0 = \frac{1}{\sqrt{LC}}$. In other words, the voltage drop over each junction is oscillating with frequency ω_0.
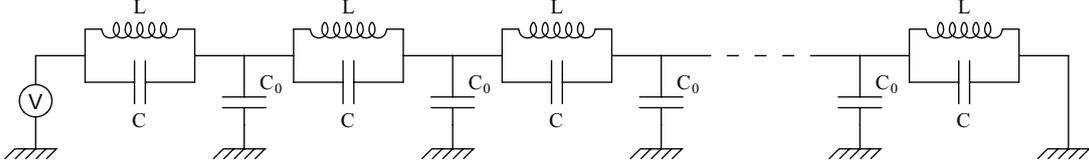

Figure 5.17: Schematic image of the harmonic chain with fixed boundary conditions.

Let us now fix the voltage boundary conditions, as depicted in fig. (5.17):

$$V_0 = V \quad ; \qquad V_N = 0 \tag{5.31}$$

We search for solutions of the type:

$$V_j = A \cos kj + B \sin kj \tag{5.32}$$

the resulting modes are the following:

$$V_j = V \left(\cos kj - \sin kj \frac{\cos kN}{\sin kN} \right) \tag{5.33}$$

In order to deduce the total admittance, we write the Kirchhoff law for the chain seen as one element. The current through the first LC element is equal to the current passing through the entire chain:

$$(V_0 - V_1)\, Y = V\, Y_{ch} \tag{5.34}$$

where Y_{ch} is the admittance of the chain. Replacing eq. (5.33) in (5.34) we get the expression for the chain admittance:

$$Y_{ch} = \frac{1 - \left(\frac{\omega}{\omega_0}\right)^2}{-i\omega L} \left[\frac{\sin k\,N - \sin k\,(N-1)}{\sin k\,N} \right] \tag{5.35}$$

Notice that the admittance of the chain Y_{ch} diverges for $K\,N = m\,\pi$, where m is an integer number. The condition $K = \frac{m\pi}{N}$ corresponds to the resonant modes that produce standing electromagnetic waves inside the chain. The frequencies of the resonant modes Ω_k for which the admittance diverges, are given by the following expression:

$$\Omega_k = \omega_0 \sqrt{\frac{1 - \cos\left(\frac{\pi}{N}k\right)}{1 - \cos\left(\frac{\pi}{N}k\right) + \frac{1}{2}\frac{C_0}{C}}} \quad , \qquad k \in \left[-\frac{N}{2}, \frac{N}{2} \right] \tag{5.36}$$
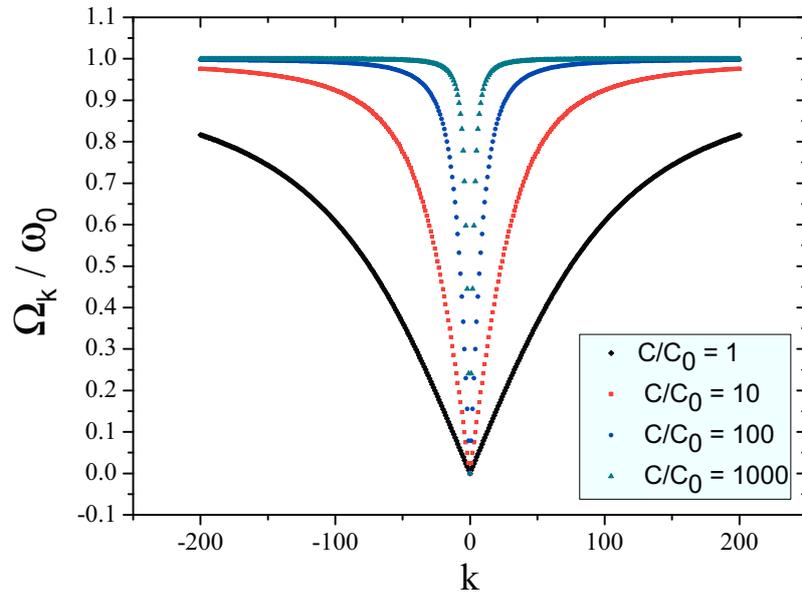
Figure 5.18: Plot of the dispersion relations (5.36) for chains of 400 junctions with different C/C_0 ratios. Frequencies are plotted in units of the plasma frequency of one junction ω_0.
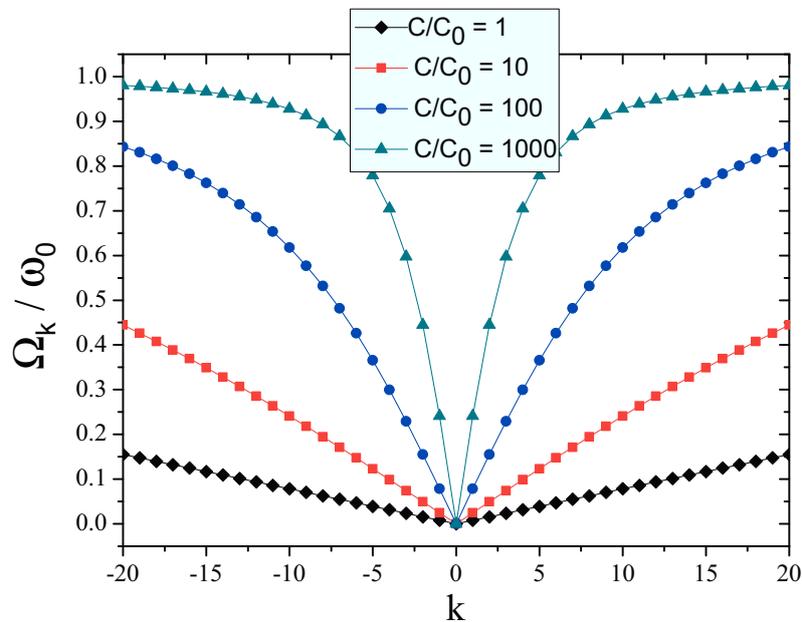

Figure 5.19: Dispersion relation for chains of 400 junctions, in the region of small wave vectors k. The lines are guides for the eye.

In fig. 5.18, we have plotted the calculated modes Ω_k for a 400 junctions chain and for different C/C_0 ratios. Notice how for large C/C_0 ratios, the majority of the modes are situated at values near the plasma frequency. For small C/C_0 the characteristic frequency of all modes is significantly lowered.

The low frequency resonant modes Ω_k, act as an effective dissipative environement for QPS dynamics and therefore suppress the quantum phase-slip amplitude for the chain. We think this is the main reason why the 400 junctions chain does not show the expected insulating region (see Fig. 5.15b). This is why, in practice we would like to avoid the low lying modes which appear at low values of k. In fig. 5.19 we present a detailed view of the region around $k = 0$. In the limit of small k, the dispersion relation (5.36) can be linearized and it reads: $\Omega_{k-small} = \omega_0 \sqrt{C/C_0} \left(\pi/N\right) k$. If we want to avoid the low energy modes, we need to satisfy the condition: $\Omega_{k=1} \simeq \omega_0$. In conclusion, the maximum length of a Josephson chain that has no low lying modes is $N \simeq \pi \sqrt{\frac{C}{C_0}}$. We notice how the ground coupling C_0 introduces a natural screening length for the chain with a characteristic length $\sim \sqrt{\frac{C}{C_0}}$.

In the following I will present the experiment that we have designed to measure the low lying modes in a chain of 400 Josephson junctions. Each junction is made in the form of a superconducting quantum interference device (SQUID) in order to enable tunable inductance, by applying a magnetic flux Φ_S through the SQUIDs. An e-beam image of two SQUIDs and the corresponding equivalent circuits for one SQUID are presented in fig. 5.20. The inductances associated with the superconducting wires connecting the SQUIDs $L_W^{ch} \simeq 40\,\text{pH}$ and forming the SQUID loop $L_W^{SQ} \simeq 60\,\text{pH}$, presented in fig. 5.20b, are much smaller than the Josephson inductance $L_J = 1.2\,\text{nH}$. In a first order approximation we can neglect L_W^{ch} and L_W^{SQ}. The resulting circuit is presented in fig. 5.20c. Notice that the equivalent circuit for a SQUID in the Josephson junction chain, as depicted in fig. 5.20c, is the same as the elementary cell in the harmonic model represented in fig. 5.16.

Junction chains with similar structure have been fabricated and measured by K. Lehnert et al. [106,107] in the attempt to engineer a so called "metamaterial"; a compact highly tunable microwave resonator. They characterised this quarter-wave Josephson resonator by microwave reflection measurements.

Using an inductive coupling (see Fig. 5.14), we can excite the harmonic modes of the chain by applying microwaves. The microwave lines are attenuated at the cryostat entrance, at the $1K$ level and at the $50\,\text{mK}$ stage. For a detailed view of the electrical scheme see fig. 2.9 in chapter 2 on fabrication and the experimental setup.

Typical measured current voltage curves for the Josephson chain at zero frustration $\phi = 0$ are presented in fig. 5.21. In order to do spectroscopy measurements we fix a certain working point on the IV curve and we sweep the microwave frequency f. We have performed spectroscopies for different working points on the IV curve shown in fig. 5.21. We only see resonances associated with the Josephson junction chain for working points inside the linear region of the IV curve.

The shape of the resonance peaks depends on the position of the working point in the linear region of the IV. Inside the hysteretic region the peaks show
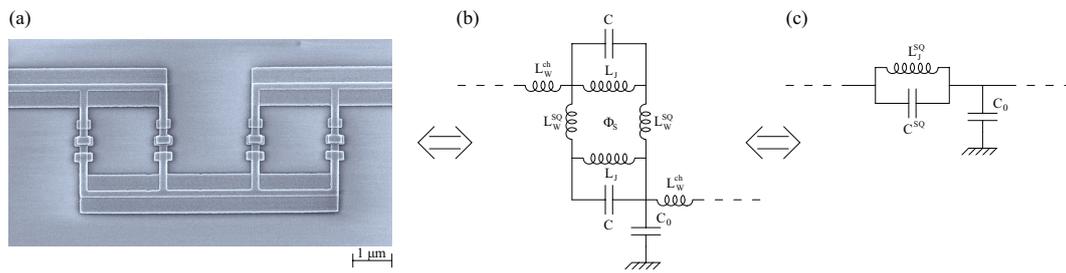
Figure 5.20: Elementary cell of the Josephson chain. (a) e-Beam image of two SQUIDs in the chain. (b) Equivalent circuit for one SQUID in the linear limit. The inductances of the superconducting wires are also shown. (c) Simplified circuit where we neglect the wire inductances and we only consider the dominant contribution from the SQUID inductance L_J^{SQ}.
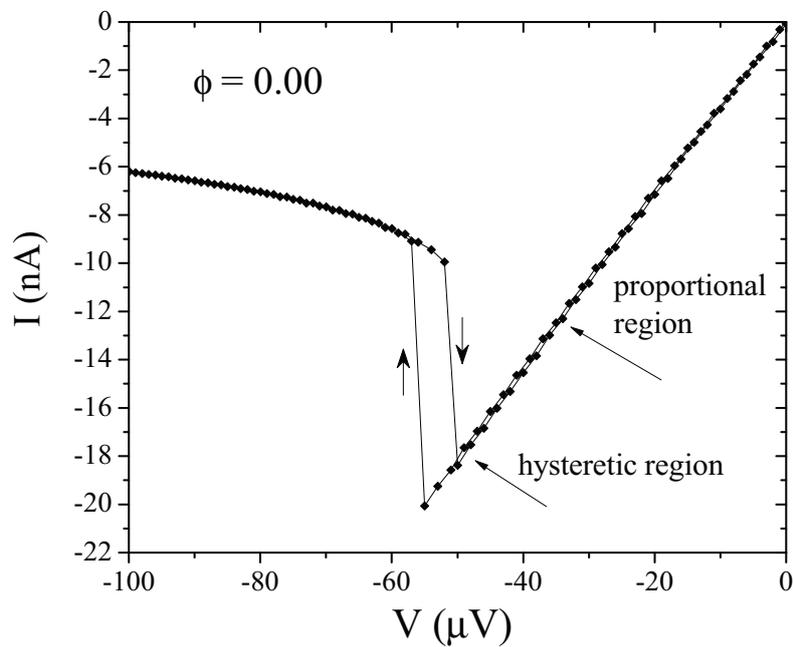

Figure 5.21: Biasing points on the IV curve for spectroscopy measurements of the 400 Josephson junction chain.
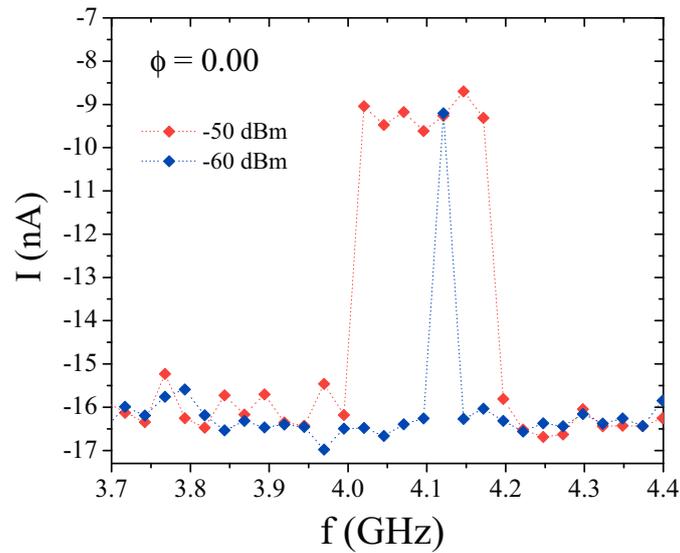
Figure 5.22: Spectroscopy peak for the bias point in the hysteretic region. The power of the microwave radiation is indicated for each curve in units of dBm. The dotted lines are guides for the eye.
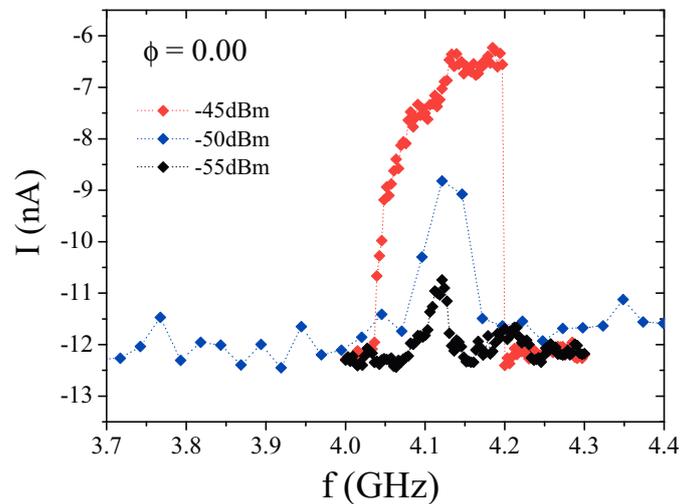
Figure 5.23: Spectroscopy peak for the bias point in the so called "proportional region" (see fig. 5.21), where the peaks heights and widths are increasing with the microwave power. The power of the microwave radiation is indicated for each curve in units of dBm. The dotted lines are guides for the eye.

a switching behavior between two bistable states, as shown in fig. 5.22. When increasing the power of the radiation, the peaks only gain in width without changing their height. If the working point is chosen outside the hysteretic region, closer to the zero voltage bias, the position of the peaks does not change, but the peaks shape is closer to a Lorentzian and both height and width increase with the microwave power, as indicated in fig. 5.23.

In figure 5.24 we present the measured current for a voltage bias in the proportional region as a function of microwave frequency. The three curves correspond to different flux frustrations ϕ in the SQUIDs. On the left side of the spectrum, at low frequencies, we observe two resonance peaks, of width $\backsim 50\,\mathrm{MHz}$, that have different positions at different frustrations. In the middle of the spectrum we observe a series of large peaks that do not change position as a function of frustration and which are associated with geometric resonances in the microwave environment close to the sample. On the right side of the spectrum we observe a continuum where the current I in the chain is suppressed. We associate this regime to the sequence of overlapping resonance peaks that arises from the flat part of the dispersion relation (5.36) at large wave vectors k.
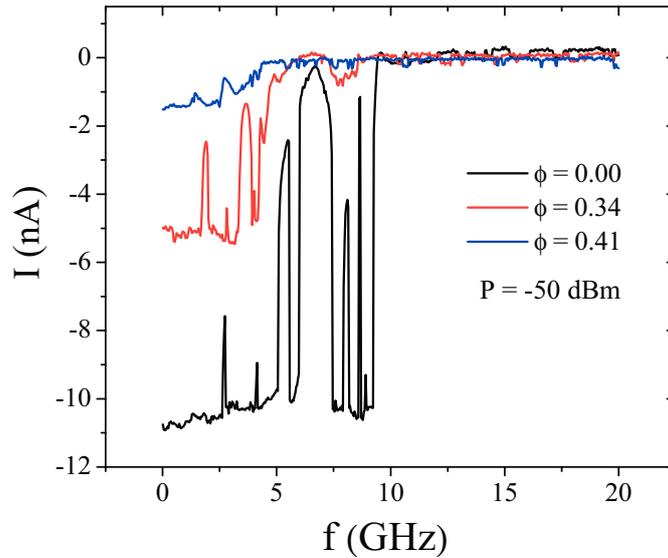
Figure 5.24: Full range spectroscopies of the 400 junctions chain, for three different frustrations ϕ. The chain was voltage biased at $V = -30\mu V$. Notice that the first three peaks change position with frustration.

The positions of the first two peaks should correspond to two of the low lying modes of the 400 junctions chain. The dispersion relation (5.36) depends on several physical parameters of the chain: the length N, the plasma frequency ω_0 of one junction in the chain, the capacitance of one junction C and the coupling to the ground C_0. All of these parameters, except C_0, are well controlled by the geometry and the fabrication of the sample. We can estimate C_0 from analytical formulas or by performing finite element numerical simulations. However, these methods only
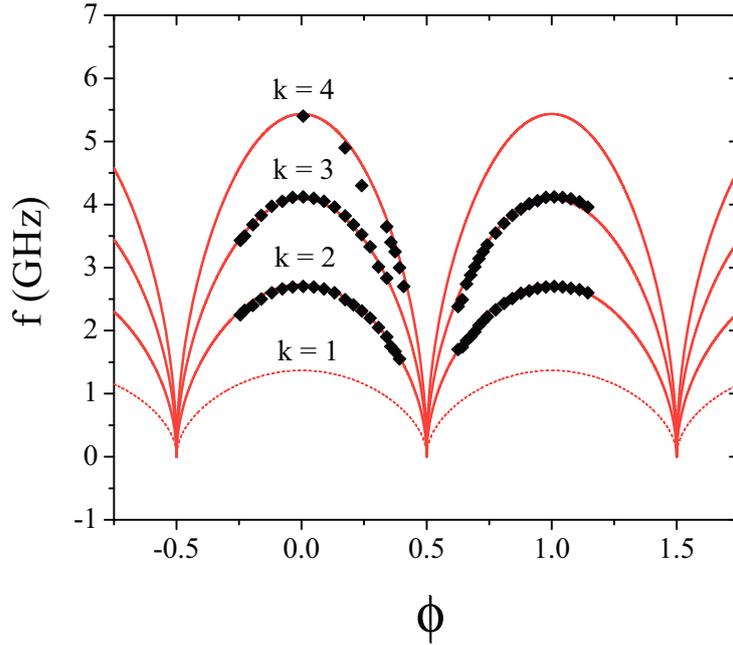
Figure 5.25: Frequency of the measured resonance peaks for the 400 Josephson junction chain (black diamonds). The red lines show the theoretical positions of the peaks given by eq. (5.36). The value of the corresponding wave vector k is indicated for each curve.

give the order of magnitude of the coupling to the ground, and it is quite difficult to obtain an exact estimation of C_0.

We have measured in detail the position of the first three resonance peaks as a function of the frustration ϕ. In figure 5.25 the black diamonds represent the measured peaks positions as a function of ϕ. At frustrations close to 0.5 the critical current of the SQUIDs is suppressed, the Josephson inductance increases and thus the resonant frequency drops. We expect the following dependence of the Josephson inductance as a function of the frustration:

$$L_J(\phi) = L_J(0) \cos(\pi\phi) \qquad (5.37)$$

The red lines represent theoretical calculations using eq. (5.36), (5.37) and the nominal values for the chain parameters $L_J(0) = 1.2\,\text{nH}$ and $C = 2.6\,\text{fF}$. The only fit parameter was $C_0 = 170 \pm 10\,\text{aF}$. This value is close to the analytically estimated value for C_0 (see Appendix B for details). Notice the good agreement between the measured and the calculated positions of the peaks for $k = 2$, 3 and 4. However, no experimental peak is observed corresponding to the first mode $k = 1$. One explanation could be that the chain's IV characteristic is insensitive to the change of the wave vector k from $k = 0$ to 1. Indeed we observe very different peak heights for $k = 2$, 3 or 4, which suggests that the sensitivity of the IV curve to the change of the wave vector k is strongly dependent on the actual value of k.

We would also like to point out the accuracy of the C_0 value resulting from the fit. We mentioned earlier that it is difficult to obtain a theoretical estimation

of C_0 with an accuracy better than a factor of 2. As shown in Fig. 5.25, using the harmonic resonant response of the chain we can fit the value of C_0 with a high accuracy of $\pm 5\,\%$. This accurate measurement of C_0 is important for the technological development of new chain designs with minimal island self capacitance.

In conclusion, in the last two sections we discussed the effect of the self capacitances C_0 on the QPS amplitude. We have experimentally observed the suppression of the QPS due to the couplings C_0 which provide a dissipation mechanism for the phase-slips. We have also constructed a harmonic model for the propagation of electromagnetic waves in the Josephson junction chain. We have measured the standing electromagnetic wave modes coresponding to $k = 2$, 3 and 4. These standing waves result from the fixed voltage boundary conditions over the chain. The fit of the resonant peak positions provides an exact method for the measurement of the self capacitance C_0 of the chain islands. For chains shorter than $\pi\sqrt{\frac{C}{C_0}}$ the plasma modes of the chain are practically at the same frequency as the plasma frequency of one junction.

Chapter 6

Measurement of MQT escape from an arbitrary shaped potential

We showed in chapter 3 that a Josephson junction can be successfully used as a current detector. The switching dynamics of the read-out junctions we have used in our experiments is governed by MQT (see Fig. 3.6). If the shape of the washboard potential deviates strongly from the tilted sinusoidal washboard, the standard MQT theory does not give a sufficiently good approximation for the escape rate Γ. In this chapter we report detailed experimental characterizations of MQT escape from the local minimum of a metastable potential which has a shape different from the standard tilted sinusoidal. The measured sample is the same as the one presented in chapter 5, the 6-SQUIDs chain. In the following chapter we focus our attention on the *details* of the MQT escape dynamics, rather than on the mesurement of the current-phase relation of the chain. In chapter 3.3 we briefly presented the theoretical methods developed in the group of Frank Hekking for the calculation of the MQT in the case of an arbitrary shaped metastable potential (see also Ref. [82]). This model, which takes into account the exact shape of the potential, gives numerical solutions for the MQT escape rate. Recently the model was confirmed by switching current measurements from the camelback shaped potential of a dc SQUID [123]. In this chapter we will also discuss an approximation of the exact model of chapter 3.3. This approximation is based on replacing the real potential, with an effective one which has a rectangular shape and for which we can calculate analytical formulas describing the MQT. We will present a detailed comparison between the experimental data, the results of the calculations using the exact model and the rectangular approximation. In the last sections of the chapter we discuss the thermal activated (TA) switching and the influence of the retrapping current I_R on the sensitivity of the detector.

6.1 Description of the metastable potential for a read-out junction in parallel with a JJ chain

We discuss in the following the switching to the dissipative state of the JJ chain connected in parallel to the read-out junction (Fig. 6.1). As mentioned in chapter
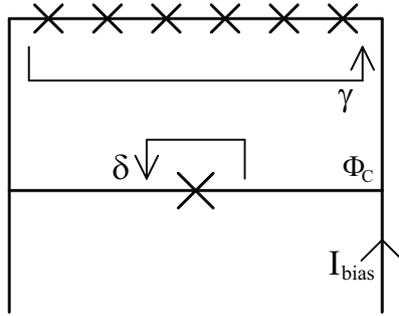
Figure 6.1: Simplified electrical scheme of the superconducting circuit: a chain of junctions in parallel with the read-out junction.

3.3, eq. 3.9, the energy-phase relation of the circuit $U_{tot}\left(\delta, \Phi_C\right)$ is a sum of the following contributions: the read-out junction with Josephson energy E_J^{RO}, the ground state energy $E_g\left(\Phi_C - \delta\right)$ of the chain and the current bias I_{bias}:

$$U_{tot}\left(\delta, \Phi_C\right) = E_J^{RO} \cos \delta + E_g\left(\Phi_C - \delta\right) - \frac{\hbar}{2e} I_{bias}\delta \qquad (6.1)$$

In Fig. 6.2 we plot the energy-phase relations of the current biased read-out junction (a), the junction chain (b) and the resulting total potential $U_{tot}\left(\delta, \Phi_C\right)$. Notice the distorted form of the total potential well (Fig. 6.2c), compared to the one of the read-out junction (Fig. 6.2a). These distortions have a significant influence on the escape rate and they are not accounted for in the standard MQT theory, which is only valid for energy-phase relations of the type presented in Fig. 6.2a [80, 81].

In order to get an intuitive physical image of the factors which come into play in the complex MQT process, we define a set of characteristic parameters for the shape of the total washboard potential U_{tot}. We define the barrier height H as the difference between the local maximum and minimum, the width W of the well, measured at an energy level $1/2 \cdot \hbar\omega_0$ from the minimum, and the length L of the barrier, at the same level of $1/2 \cdot \hbar\omega_0$ (Fig. 6.3). ω_0 is the plasma frequency of the read-out junction, so $1/2 \cdot \hbar\omega_0$ is the energy level of the ground state.

In Fig. 6.4 we present the calculated dependence of the height H of the barrier, the width W of the well and the length L of the barrier for the complete washboard potential U_{tot}, as a function of the phase Φ_C and the applied current I_{bias}. As expected, all three parameters decrease with the applied current. The barrier height H shows a regular periodic dependence with the phase bias Φ_C. When H increases, the escape probability decreases. The parameters W and L are also periodic with Φ_C, but they exhibit an additional peak structure around $\Phi_C = \pi$. When W increases, the plasma frequency, which is the characteristic attempt frequency for the tunneling, also decreases, so we expect a decrease in the tunnel amplitude. Also, when the length L of the barrier increases, we expect an exponential decrease of the escape probability. In conclusion, whenever one of the parameters H, W or L increases, the MQT rate decreases and we measure an increase of the switching current I_{SW}. We will later show that we measure experimentally a switching current which is periodic in Φ_C and which shows positive switching peaks in the vicinity of $\Phi_C = \pi$. We will argue that these switching current peaks are signatures of the
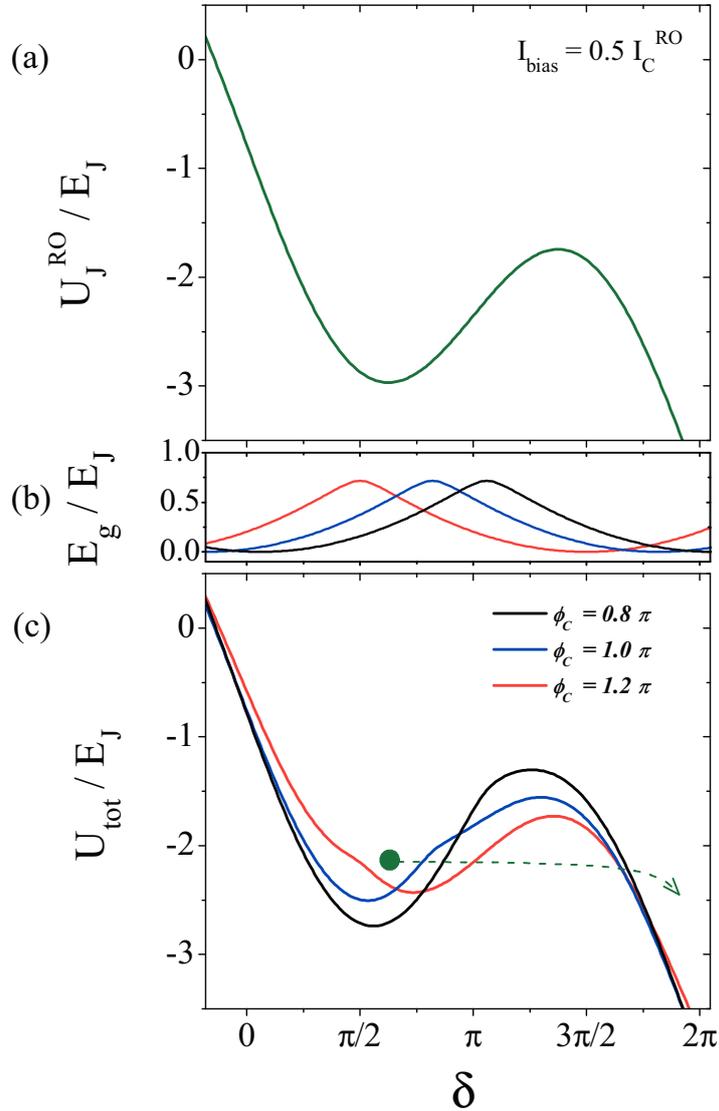
Figure 6.2: Energy phase relations for the current biased read-out junction (a), the Josephson junction chain in the ground state (b) and $U_{tot}(\delta)$ (c). $U_{tot}(\delta)$ is simply the sum of the curves of (a) and (b). The different curves correspond to different phase biases Φ_C, labeled in the inset of (c). The MQT switching to the dissipative state of the superconducting circuit schematized in Fig. 6.1 occurs from a local minimum of the metastable potential represented in (c). The $y-axis$ values are represented in units of E_J, where E_J is the Josephson energy of one junction in the chain. For presentation purposes, in order to highlight the chain contribution to the switching potential, we considered a ratio E_J/E_J^{RO} twice as large compared to the one of the measured sample.
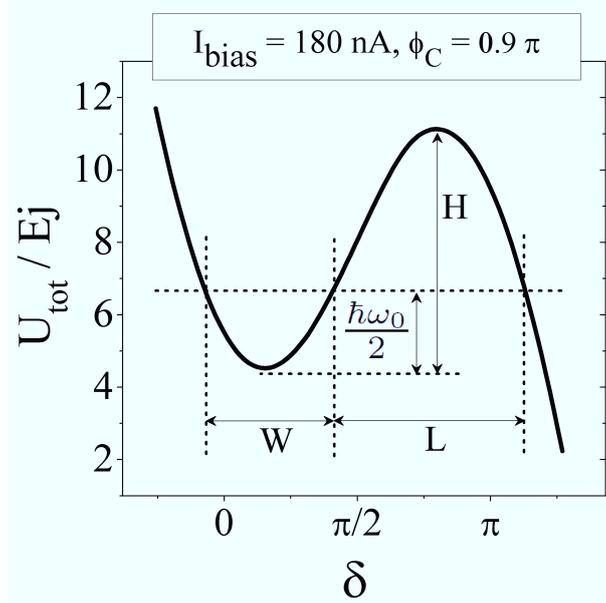
Figure 6.3: Definition of the characteristic parameters for the washboard potential.
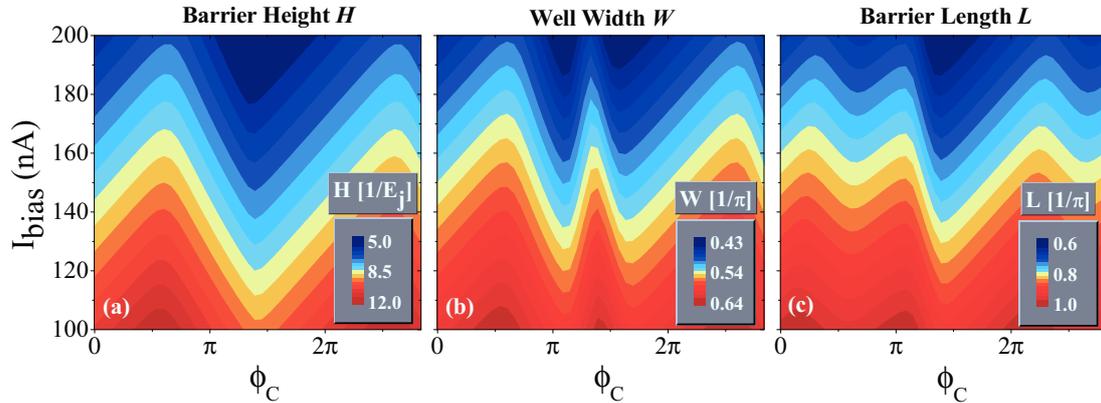
Figure 6.4: Color plots presenting the dependence of the barrier H, the well width W and the barrier length L, as a function of the phase bias Φ_C and the current bias I_{bias}. The height H of the barrier is represented in units of E_J, while W and L are measured in units of π, as indicated in the color scale. Notice the pronounced peak of the the width W for phases $\Phi_C \gtrsim \pi$, as well as the peak in the dependence the barrier length L for a phase bias $\Phi_C \simeq \pi$.

irregularities in W and L, which are visible in Fig 6.4.

6.2 The effective rectangular washboard potential approximation
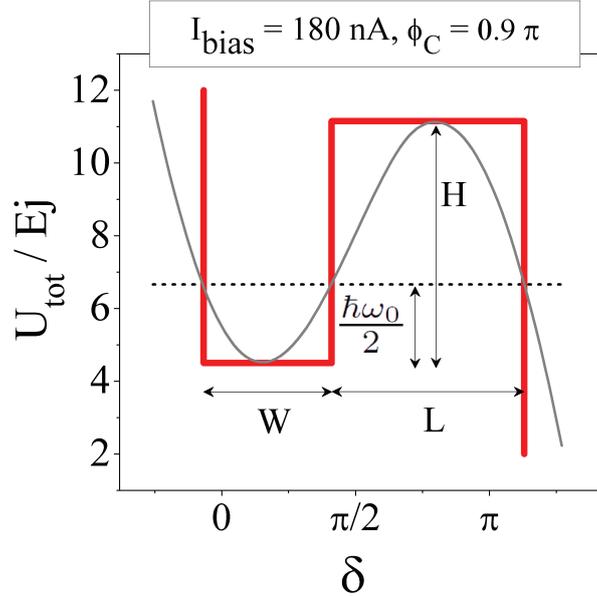
Figure 6.5: The effective rectangular shaped potential (in red line) which has the same height H, well width W and barrier length L as the real potential (in gray line).

We now briefly discuss an effective model for the calculation of the MQT escape from a local minimum of U_{tot}. We replace the real potential with a rectangular shaped potential with the same characteristic parameters H, W and L we already studied in the previous section, as represented by the red plot in Fig. 6.5. The interest of constructing this effective rectangular potential approximation is that we can derive simple analytical formulas for the MQT (see eq. 6.3), which give an intuitive understanding of the relevant physical parameters governing the tunneling process.

The ground state energy E_0 in the local minimum of the rectangular potential is given by [124]:

$$E_0 = \frac{\hbar^2}{2m}\left(\frac{\pi}{W}\right)^2 = 4E_C^{RO}\left(\frac{\pi}{W}\right)^2 \tag{6.2}$$

where $m = \hbar^2/\left(8E_C^{RO}\right)$ is the mass of the phase quasiparticle in the $RCSJ$ model (see chapter 3.1) and $E_C^{RO} = e^2/(2C)$ is the charging energy of the read-out junction. In the weak tunneling limit, the MQT escape rate Γ_{eff} is the following [124]:

$$\Gamma_{eff} = v_{try} \cdot \frac{16\,E_0\,(H - E_0)}{H^2} \cdot \exp\left[-L\sqrt{\frac{H - E_0}{E_C^{RO}}}\right] \tag{6.3}$$

Where v_{try} is the escape attempt frequency, given by:

$$v_{try} = \frac{2E_0}{h} \qquad (6.4)$$

The total switching probability is given by the decay equation and it reads:

$$P_{SW-eff} = 1 - \exp\left[-\Gamma_{eff} \triangle t\right] \qquad (6.5)$$

The analytical formulas of the effective rectangular potential model described above constitute an approximation of the complete numerical solutions for the escape rate obtained using the instanton model (eq. 3.10).

6.3   Measurement of the MQT switching

We present detailed measurements of the switching probability (in Fig. 6.6b) and the results of the P_{SW} calculations using the effective rectangular potential model (in Fig. 6.6a) and the instanton model of chapter 3.3 applied to the exact shape of U_{tot} (in Fig. 6.6c). Both theoretical models give a fairly good description for the amplitude and for the overall shape of the switching current oscillations as a function of the phase Φ_C. Notice the switching current peaks measured in the vicinity of $\Phi_C = \pi$ in Fig. 6.6b. Notice also that using the detailed instanton calculations (plotted in Fig. 6.6c) we retrieve a pronounced current peak at the same position in the current-phase characteristic.

If we now look at the width w of the switching histograms plotted in Fig. 6.6d, e and f, we observe that it is not constant as a function of the phase. This effect is expected since w depends on the exact characteristics of the washboard local minimum, which changes shape with Φ_C (as shown in Fig. 6.4). We would like to notice that both theoretical models give a good qualitative description for the phase dependence of w. Moreover, the theoretical results given by the instanton model are within an interval of only $15 - 20\%$ from the measured values.

From the results presented in Fig. 6.6 we conclude that the instanton calculations give a reliable quantitative description of the MQT switching to the dissipative regime, for a phase quasiparticle trapped in an arbitrary shaped metastable potential. Also, the effective rectangular potential approximation, introduced in section 6.2, gives a fairly accurate qualitative understanding. This fact is explained by the following qualitative argument. From the instanton calculation of the MQT (eq. 3.10 and eq. 3.12), we see that the escape rate Γ deppends mainly on the area under the potential barrier. The effective rectangular washboard approximates fairly well this area of the real U_{tot} barrier. Morover, within the model of the rectangular washboard, the parameters H, W and L are independent and they map the real shape of the potential U_{tot}. This is not the case for the standard MQT theory, which assumes a fixed relation between H, W and L.
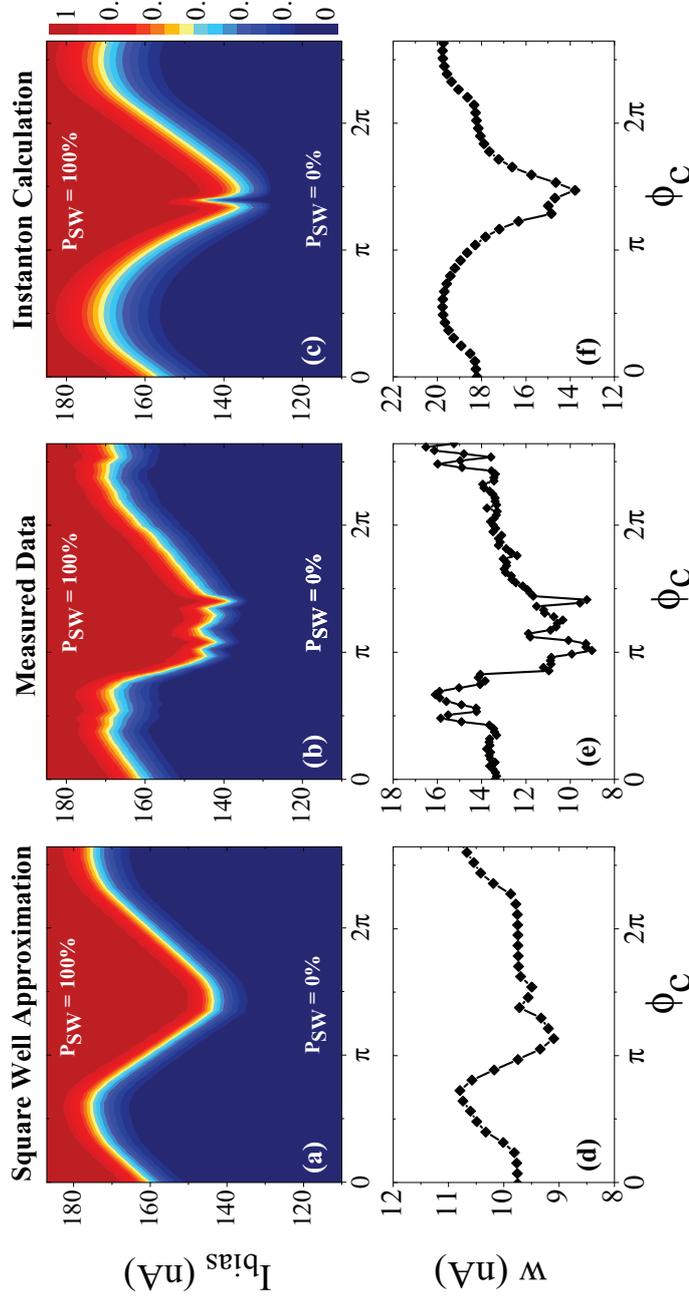
Figure 6.6: Results of the measured and calculated MQT switching probabilities P_{SW} for the superconducting circuit consisting of a chain of six Josephson junctions with $E_J/E_C = 3$, in parallel with a larger read-out junction (see Fig. 6.1). The measured probabilities are presented in (b) and the corresponding histogram widths w are plotted in (e). w is defined as the difference between the electrical currents at $P_{SW} = 80\%$ and $P_{SW} = 20\%$. For comparison, the results of the calculations using the effective rectangular well approximation are shown in (a) and (d) and the results of the instanton calculations are plotted in (c) and (f).

103

6.4   Measurement of the TA switching

We continue the characterization of the escape to the dissipative regime from the metastable potential U_{tot}, with measurements at higher temperatures. In Fig. 6.7 we show the evolution of the histogram width w with temperature. Below $T = 150$ mK, we observe a saturation of the w values, for all phase biases, as we expect from MQT switching. When we increase the temperature above 150 mK, the histogram width decreases, as the escape is mediated by thermal activation (TA). In case of underdamped junctions, w typically increases with temperature. However, it has been recently shown that in the case of junctions with quality factors Q close to 1, in the TA regime, w decreases with temperature [93].

The reason for this counter intuitive decrease of the histogram width is the following. If $Q \gtrsim 1$, there will be a significant chance that after the initial escape of the phase particle from the metastable potential, it will not continue to roll down the washboard, and produce a measurable voltage signal, but it will get retrapped in the next local minimum. In Fig. 6.8 we represent the re-trapping process for an
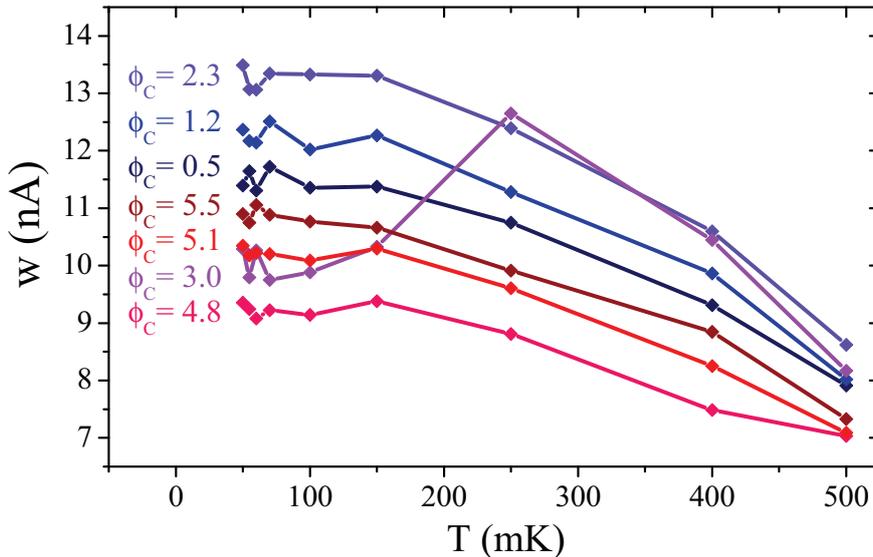

Figure 6.7: Temperature dependence of the measured switching histograms width w, at different phase biases Φ_C. The corresponding phase bias for each curve is color coded and labeled on the left side of the figure. The lines are guides for the eye.

underdamped junction with a quality factor close to unity. For the read-out junction that we have used, the measured quality factor is $Q \simeq 4$. The succession of escape and re-trapping events does not produce a voltage sufficiently large to be detected and counted as a switching to the dissipative state. This phase evolution is called underdamped phase diffusion (UPD), in analogy with the classical phase diffusion which occurs in overdamped junctions. The re-trapping process becomes important when the critical current and the retrapping current are close to each other, with decreasing I_{bias} (Fig. 6.9). We now understand why at higher temperatures, where the TA decreases the switching current, the UPD plays an increasingly important role, significantly reducing the width of the histograms (as shown in Fig. 6.9).
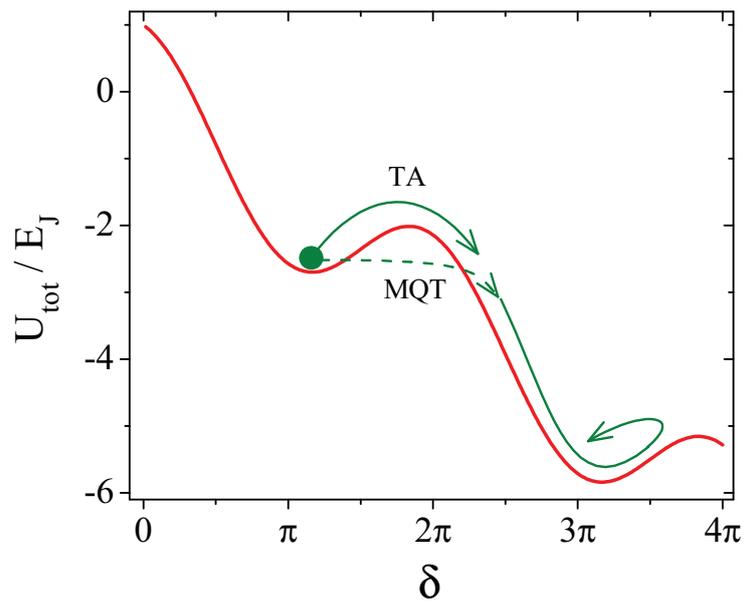
Figure 6.8: Graphic representation of the re-trapping process in the underdamped phase diffusion (UPD) regime.
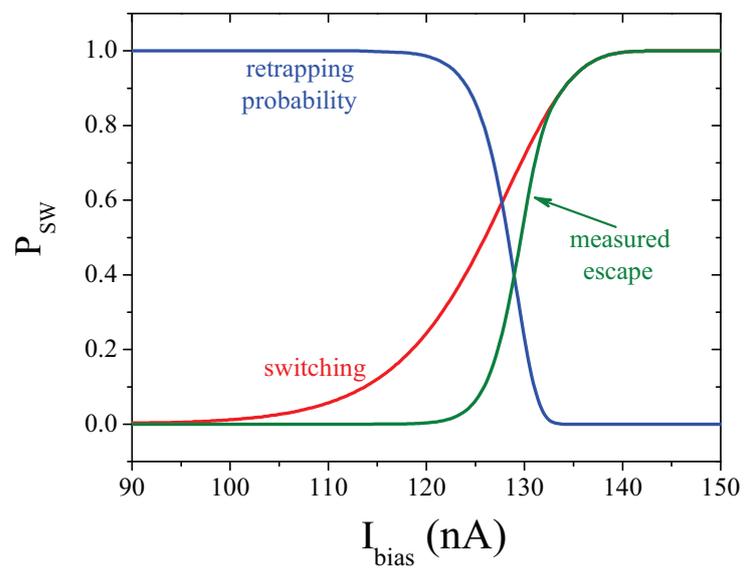

Figure 6.9: Influence of the phase-particle retrapping on the measurement of the switching current. The retrapping probability (blue line) playes the dominant role at low bias currents and it suppresses the switching (green line) to the dissipative regime after the escape (red line) from the local minimum of the metastable potential.

In Fig. 6.8, the curve corresponding to $\Phi_C = 0.95\,\pi$ is an exception to the general monotonic decrease of w with temperature. The measured w at phase biases close to π has a non monotonic dependence with temperature. The histogram width increases until $T = 250\,\text{mK}$, before dropping with temperature, as we would expect from the UPD model described above. In the vicinity of $\Phi_C = \pi$, we have shown in Fig. 6.4 that the width W of the local potential well and the length L of the barrier for the metastable potential U_{tot}, are very sensitive to small changes in the shape of the energy-phase relation of the Josephson junction chain. The temperature changes the shape of the metastable potential U_{tot}. In the vicinity of $\Phi_C = \pi$, the corresponding change in the escape probability competes with the one induced by the UPD.

6.5   Influence of the current pulse duration on the MQT switching

We continue the experimental study of the MQT escape with measurements of the current-phase relations for different durations Δt of the I_{bias} current pulse. The measurements are taken at $50\,\text{mK}$, in the MQT switching regime, for three values of the current step duration: $\Delta t = 10\,\mu\text{s}$, $50\,\mu\text{s}$ and $100\,\mu\text{s}$ (see Fig. 6.11b, d and f). The rise time for the pulses is always $\sim 10\,\mu\text{s}$ and it is fixed by the cutoff of the low pass filters connected to the current bias lines.
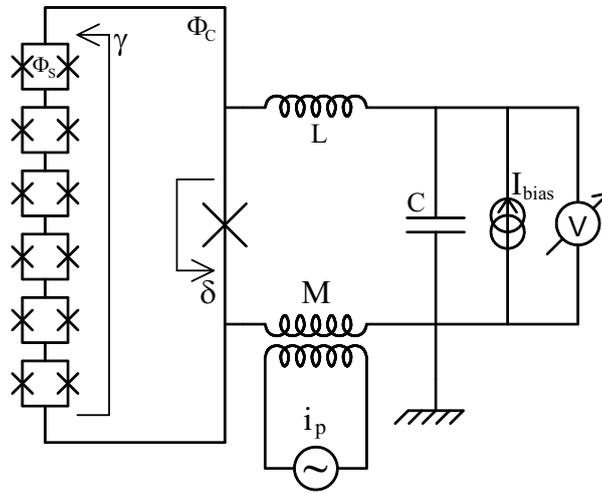
Figure 6.10: Electrical scheme of the 6 Josephson junction chain in parallel with the read-out junction. The junctions are made in form of SQUIDs. The current bias line is mutually coupled by the inductance M to a fast current pulse generator i_p. It is used to perform fast switching measurements, by inducing nanosecond current pulses in the bias line.

We present measurements performed on the same 6 SQUIDs chain sample discussed in chapter 5. The complete electrical scheme of the circuit is shown in Fig. 6.10. In Fig. 6.11 we show the measured switching current values as a function

of the flux frustration Φ_S/Φ_0 in the SQUID loops of the junction chain. As we have discussed in detail in section 5.3, with increasing flux Φ_S we expect the amplitude of the switching current-phase oscillations to decrease, because the Josephson energy of the junctions is suppressed and the QPS amplitude grows. The theoretically calculated envelope for the switching current oscillations is represented by the black empty diamonds in Fig. 6.11. We have used the instanton model to calculate the MQT escape from the total potential U_{tot}. We would like to point out that we have plugged into the calculations the measured shape of the applied current pulses I_{bias}, shown in the right panels of Fig. 6.11. The measured switching at low current bias is limited by the re-trapping current I_R, below which the read-out junction is in the UPD regime, as discussed in the previous section. The fitted value for the re-trapping current is $I_R = 125$ nA. Notice that for long current pulses (Fig. 6.11e and f), the switching current decreases to a value close the re-trapping value I_R and we observe a saturation in the lower part of the switching current oscillations.
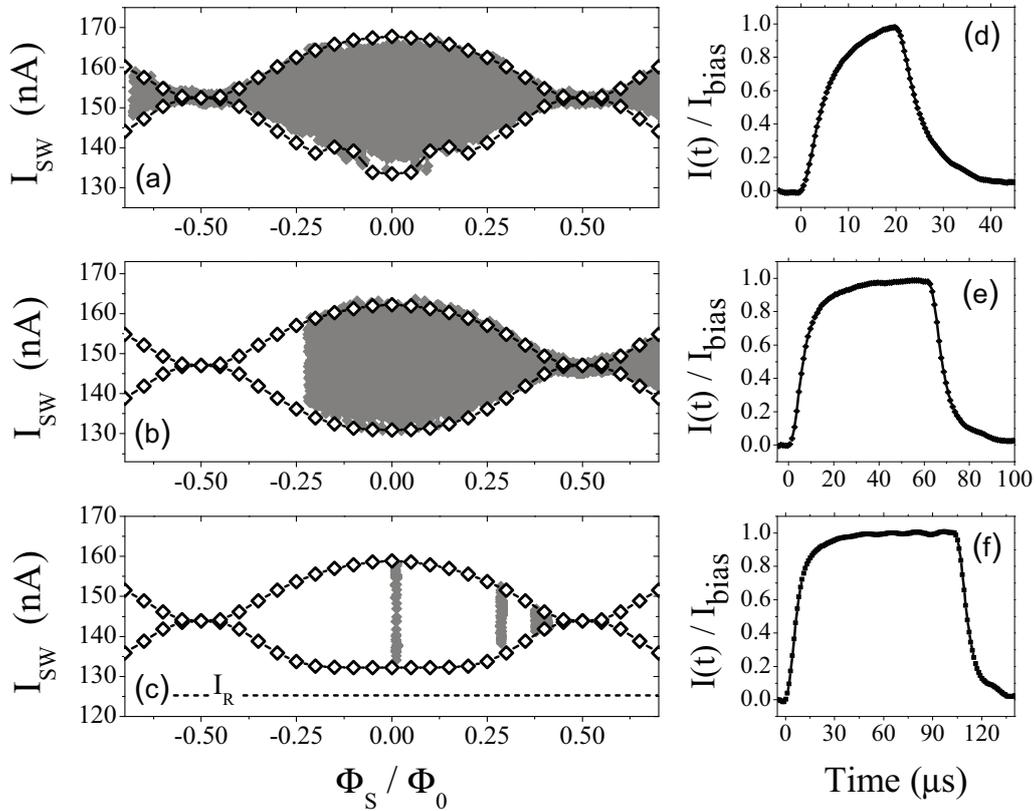
Figure 6.11: (a),(b),(c): Measurement of the envelope of the switching current oscillations, for three different current pulse durations (gray points). I_R marks the value of the retrapping current. The measured current pulse shapes are respectively plotted on the right: (d), (e) and (f). Empty diamonds: Calculated envelope of the switching current as a function of Φ_S/Φ_0.

From the shape of the current pulses presented in Fig. 6.11 we can see that if the pulse is short compared to the 10 μs rise time, its shape is quite complex and it cannot be simply approximated by a rectangular pulse. However, if the pulse is

too long, the switching current oscillations enter the UPD region and the lower part of the oscillations saturates. We can conclude that the optimal current bias pulses for the measured read-out junction are in the range $\Delta t \simeq 20 \to 50\,\mu s$.
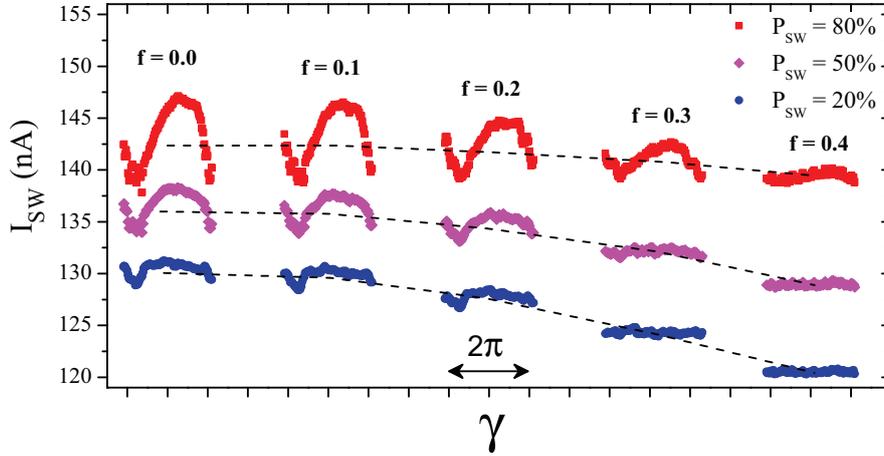
Figure 6.12: Measured switching current *vs* phase, corresponding to three escape probability levels: $P_{SW} = 20\%$ in blue, $P_{SW} = 50\%$ in magenta and $P_{SW} = 80\%$ in red. We present measured curves for different SQUID frustrations $f = \Phi_S/\Phi_0$, from $f = 0$ up to $f = 0.4$, as indicated by the labels in the figure. The dashed lines are guides for the eye, following the median line as a function of f.

In the last part of this section we present switching current measurements performed using nanosecond current pulses. The pulses are induced via the mutual coupling M (see Fig. 6.10). The duration of the pulses is $dt = 4\,ns$ and the current intensity is fixed: $i_s = 100\,nA$. We apply the pulses using the same procedure which is explained in detail in section 4.5. The fast pulses i_s are superposed on the slower I_{bias} steps, which have a typical duration of $50\,\mu s$. When using the nanopulse, the measured switching current I_{SW} is smaller compared to the one measured with standard micro seconds long pulses.

In Fig. 6.12 we present the measured I_{bias} currents, in the presence of the i_s pulses, for three values of the switching probability: $P_{SW} = 20\,\%$, $50\,\%$ and $80\,\%$. First we notice that the amplitude ΔI_{SW} of the $50\,\%$ switching current oscillations as a function of Φ_C is at maximum $5\,nA$ peak-to-peak, which is much smaller than the previously measured amplitudes of $\sim 35\,nA$. Also, the I_{SW} oscillations are twice as large for the escape probability of $80\,\%$ and almost completely suppressed for the escape probability of $20\,\%$. The median line of the $80\,\%$ level oscillations is almost constant, while the median line of the $20\,\%$ switching probability oscillations is modulated by the frustration f, with an amplitude much larger than the amplitude of the Φ_C oscillations. This large modulation of the median line level is very similar to the one measured for the classical 8 rhombi chain and presented in Fig. 4.2.1.

In the following, we argue that the observations presented above can be qualitatively explained by the UPD model. Let us notice that due to the nanosecond current pulse, the switching is induced for relatively small bias currents, very close to the value of the re-trapping current $I_R \simeq 125\,nA$. Due to the re-trapping, the

detection is less and less sensitive to the escape from the local metastable potential, but more and more sensitive to the re-trapping current level. The re-trapping only depends on the integral of the friction force along one quasi-period of the tilted washboard potential. Thus, the re-trapping level is independent on local changes of the potential shape, tuned by the phase bias Φ_C over the chain. The smaller I_{bias} is, the smaller the Φ_C oscillations of the switching current are. In other words, close to the retrapping current, the read-out junction loses its sensitivity to the changes in the JJ chain state and the signal to noise ratio of the current detector is degraded. Indeed, close to $I_{bias} = 130 \, \text{nA}$ we observe that the current-phase relation of the chain is practically lost in the noise.

However, the integral of the viscous force depends on the speed of the phase-particle sliding down the tilted washboard. This speed is modulated by the amplitude of the energy-phase relation of the chain, which is dependent on the SQUIDs frustration $f = \Phi_S/\Phi_0$. Thus, the re-trapping level decreases with f and we measure lower switching currents at high frustration, as shown in Fig. 6.12.

In conclusion, in this chapter we have presented a detailed experimental characterisation of the MQT and TA switching to the dissipative state, for a phase particle trapped in a metastable potential which does not have the usual tilted sinusoidal shape. We compared our measurements with two theoretical models. The first model is a numerical calculation of the MQT, using the instantons technique (discussed in section 3.3), for the real shape of the metastable potential U_{tot}. The second model is an effective rectangular potential approximation, which gives analitycal results for the MQT escape rate. The agreement of the measured data with the theoretical calculation is satisfactory for both models. The results of the instanton calculation for the switching probability are in quantitative agreement with the measurements. We have also shown that the phase dynamics of the read-out junction is gouverned by UPD at temperatures $T > 250 \, \text{mK}$ and current biases $I_{bias} \lesssim 130 \, \text{nA}$. The UPD degrades the sensitivity of the read-out junction. For an optimal signal to noise ratio, the UPD region should be avoided.

Chapter 7

Conclusions and Perspectives

In this thesis we presented detailed measurements of quantum phase-slips in Josephson junction chains. The measured phase-slips are the result of fluctuations induced by the finite charging energy of each junction. Our experimental results can be fitted in very good agreement by considering a simple tight-binding model for QPS [52]. We have shown that under phase-bias, a chain of Josephson junctions or rhombi can behave in a collective way very similar to a single macroscopic quantum object. These results open the way for possible use of quantum phase-slips for the design of novel Josephson junction circuits, such as topologically protected rhombi qubits or current-to-frequency conversion devices.

In chapter 5 we presented measurements of QPS in a phase biased 6 Josephson junction chain, inserted in a superconducting loop. A QPS corresponds to the tunneling a flux quantaum into or out of the loop. The QPS tunneling rate is controlled by the ratio E_J/E_C. By constructing each junction of the chain in the form of a SQUID, we could continuously tune in situ the QPS rate. We also measured charge induced interference of QPS, which is a manifestation of the more general Aharonov-Casher interference of magnetic moments circling a non zero electric charge. For this measurement we induced polarization charges on the islands of the chain via a nearby gate electrode and we measured the resulting interference patterns. All these results were found to be in good agreement with theoretical expectations from the basic MLG tight-binding theory [52], which is valid in the regime of weak quantum phase-slips $E_J \geq E_C$.

We have also measured the current-voltage characteristics of a long chain of 400 junctions in which we observed the suppression of QPS due to the self capacitance C_0 of the chain islands. We measured the first three modes of standing electromagnetic waves in this chain, at frequencies between 2 and 5 GHz.

In my opinion, the next step would be the measurement and the quantitative understanding of the strong phase-slip regime in longer chains with similar E_J/E_C ratio and smaller C_0. We expect a complete suppression of the supercurrent in such devices, so the measurement should be performed in a voltage bias scheme. Once this regime is well controlled, we can address the problem of phase locking between an applied microwave signal and the quasiclassical charge dynamics in the chain, for the possible implementation of a frequency-to-current conversion device.

In chapter 4 we presented measurements of the ground state of classical

and quantum Josephson rhombi circuits. In a linear chain of 8 rhombi and in a 2D rhombi network with $E_J \gg E_C$, we measured the crossover from $2e$ Cooper pair electrical transport to $4e$ transport by correlated pairs of Cooper pairs. We also measured the suppression of the supercurrent due to QPS in a chain of 8 rhombi in the quantum regime $E_J \geq E_C$. In a rhombus, the QPS tunneling evolves in a 2D potential, whereas in the case of a single Josephson junction, the phase tunnels from the 1D sinusoidal potential of the junction. We have shown that a slightly adapted model, derived from the initial MLG theory for junction chains, fits the measured current-phase relation for the chain of 8 rhombi. We have also tried to measure the excited states of a 2D rhombi network, which was designed to realize a topologically protected qubit. Due to the microwave coupling scheme, we could only excite local modes of the network instead of the collective 2D qubit modes. I believe that for an optimized coupling between the rhombi qubit and the applied microwaves, it should be possible to excite the qubit, measure its coherence time and test the topological protection idea.

In order to measure the current-phase relation of the Josephson junction and rhombus chains, we employed a measurement technique originally developed for qubit circuits [26]. In this thesis we pushed the read-out technique to its limits, by measuring very low currents using a quantum read-out Josephson junction. The switching to the voltage state of the read-out junction occurs via macroscopic quantum tunneling. In chapter 6 we presented detailed measurements of the MQT probability. We have also shown that we can quantitatively understand these results by two theoretical models. The first model, which gives the best results, is a numerical calculation for the MQT from an arbitrary potential, developed in the group of Frank Hekking. The second model is an effective rectangular potential approximation.

Finally, the fabrication reproducibility and the time stability of the junctions is essential for any device. At the beginning of my thesis we optimized the fabrication process in order to obtain highly stable junctions. We also measured the variance of the tunnel resistance in large sets of junctions fabricated in identical conditions. We found that the typical standard deviation of our junctions is $\pm 4\,\%$. This value is sufficiently small for the observation of collective behavior in JJ chains.

Bibliography

[1] G. E. Moore, "Cramming more components onto integrated circuits," *Electronics*, vol. 38, 1965.

[2] O. H. Kamerlingh, "The superconductivity of mercury," *Comm. Phys. Lab. Univ. Leiden*, pp. 122–124, 1911.

[3] A. Einstein, "Quantum theory of mono-atomic ideal gas. second paper." *Sitzungsberichte Der Preussichen Akademie Der Wissenschaften Physikalisch-mathematische Klasse*, pp. 3–14, 1925.

[4] L. N. Cooper, "Bound electron pairs in a degenerate fermi gas," *Physical Review*, vol. 104, no. 4, pp. 1189–1190, 1956.

[5] J. Bardeen, L. N. Cooper, and J. R. Schrieffer, "Theory of superconductivity," *Physical Review*, vol. 108, no. 5, pp. 1175–1204, 1957.

[6] B. D. Josephson, "Possible new effects in superconductive tunnelling," *Physics Letters*, vol. 1, no. 7, pp. 251 – 253, 1962.

[7] R. C. Jaklevic, A. H. Silver, J. Lambe, and J. E. Mercereau, "Quantum interference effects in josephson tunneling," *Physical Review Letters*, vol. 12, no. 7, pp. 159–&, 1964.

[8] R. C. Jaklevic, J. E. Mercereau, J. J. Lambe, and A. H. Silver, "Quantum interference from static vector potential in field-free region," *Physical Review Letters*, vol. 12, no. 11, pp. 274–&, 1964.

[9] J. Clarke and A. I. Braginski, *The SQUID Handbook: Fundamentals and Technology of SQUIDs and SQUID Systems*, 1st ed. Wiley-VCH, August 2004.

[10] M. H. Devoret, J. M. Martinis, and J. Clarke, "Measurements of macroscopic quantum tunneling out of the zero-voltage state of a current-biased josephson junction," *Physical Review Letters*, vol. 55, no. 18, pp. 1908–1911, 1985.

[11] I. Chiorescu, Y. Nakamura, C. J. P. M. Harmans, and J. E. Mooij, "Coherent quantum dynamics of a superconducting flux qubit," *Science*, vol. 299, no. 5614, pp. 1869–1871, 2003.

[12] A. D. O'Connell, M. Hofheinz, M. Ansmann, R. C. Bialczak, M. Lenander, E. Lucero, M. Neeley, D. Sank, H. Wang, M. Weides, J. Wenner, J. M. Martinis, and A. N. Cleland, "Quantum ground state and single-phonon control of a mechanical resonator," *Nature*, vol. 464, no. 7289, pp. 697–703, 2010.

[13] M. Ansmann, H. Wang, R. C. Bialczak, M. Hofheinz, E. Lucero, M. Neeley, A. D. O'Connell, D. Sank, M. Weides, J. Wenner, A. N. Cleland, and J. M. Martinis, "Violation of bell's inequality in josephson phase qubits," *Nature*, vol. 461, no. 7263, pp. 504–506, 2009.

[14] I. Chiorescu, P. Bertet, K. Semba, Y. Nakamura, C. J. P. M. Harmans, and J. E. Mooij, "Coherent dynamics of a flux qubit coupled to a harmonic oscillator," *Nature*, vol. 431, no. 7005, pp. 159–162, Sep. 2004.

[15] A. Wallraff, D. I. Schuster, A. Blais, L. Frunzio, R. S. Huang, J. Majer, S. Kumar, S. M. Girvin, and R. J. Schoelkopf, "Strong coupling of a single photon to a superconducting qubit using circuit quantum electrodynamics," *Nature*, vol. 431, no. 7005, pp. 162–167, 2004.

[16] A. Fay, E. Hoskinson, F. Lecocq, L. P. Levy, F. W. J. Hekking, W. Guichard, and O. Buisson, "Strong tunable coupling between a superconducting charge and phase qubit," *Physical Review Letters*, vol. 100, no. 18, 2008.

[17] L. DiCarlo, M. D. Reed, L. Sun, B. R. Johnson, J. M. Chow, J. M. Gambetta, L. Frunzio, S. M. Girvin, M. H. Devoret, and R. J. Schoelkopf, "Preparation and measurement of three-qubit entanglement in a superconducting circuit," *Nature*, vol. 467, no. 7315, pp. 574–578, 2010.

[18] M. Neeley, R. C. Bialczak, M. Lenander, E. Lucero, M. Mariantoni, A. D. O'Connell, D. Sank, H. Wang, M. Weides, J. Wenner, Y. Yin, T. Yamamoto, A. N. Cleland, and J. M. Martinis, "Generation of three-qubit entangled states using superconducting phase qubits," *Nature*, vol. 467, no. 7315, pp. 570–573, 2010.

[19] W. J. Elion, M. Matters, U. Geigenmuller, and J. E. Mooij, "Direct demonstration of heisenbergs uncertainty principle in a superconductor," *Nature*, vol. 371, no. 6498, pp. 594–595, Oct. 1994.

[20] F. Sharifi, A. V. Herzog, and R. C. Dynes, "Crossover from 2-dimension to one-dimension in in-situ grown wires of pb," *Physical Review Letters*, vol. 71, no. 3, pp. 428–431, Jul. 1993.

[21] A. Bezryadin, C. N. Lau, and M. Tinkham, "Quantum suppression of superconductivity in ultrathin nanowires," *Nature*, vol. 404, no. 6781, pp. 971–974, 2000.

[22] C. N. Lau, N. Markovic, M. Bockrath, A. Bezryadin, and M. Tinkham, "Quantum phase slips in superconducting nanowires," *Physical Review Letters*, vol. 87, no. 21, 2001.

[23] M. A. Nielsen and I. L. Chuang, *Quantum Computation and Quantum Information*, 1st ed.   Cambridge University Press, October 2000.

[24] E. Knill, "Physics quantum computing," *Nature*, vol. 463, no. 7280, pp. 441–443, Jan. 2010.

[25] T. D. Ladd, F. Jelezko, R. Laflamme, Y. Nakamura, C. Monroe, and J. L. O'Brien, "Quantum computers," *Nature*, vol. 464, no. 7285, pp. 45–53, Mar. 2010.

[26] D. Vion, A. Aassime, A. Cottet, P. Joyez, H. Pothier, C. Urbina, D. Esteve, and M. H. Devoret, "Manipulating the quantum state of an electrical circuit," *Science*, vol. 296, no. 5569, pp. 886–889, May 2002.

[27] J. M. Martinis, S. Nam, J. Aumentado, and C. Urbina, "Rabi oscillations in a large josephson-junction qubit," *Physical Review Letters*, vol. 89, no. 11, p. 117901, Sep. 2002.

[28] F. Mallet, F. R. Ong, A. Palacios-Laloy, F. Nguyen, P. Bertet, D. Vion, and D. Esteve, "Single-shot qubit readout in circuit quantum electrodynamics," *Nature Physics*, vol. 5, no. 11, pp. 791–795, Nov. 2009.

[29] A. Lupascu, S. Saito, T. Picot, P. C. De Groot, C. J. P. M. Harmans, and J. E. Mooij, "Quantum non-demolition measurement of a superconducting two-level system," *Nature Physics*, vol. 3, pp. 119–123, 2007.

[30] A. Palacios-Laloy, F. Mallet, F. Nguyen, P. Bertet, D. Vion, D. Esteve, and A. N. Korotkov, "Experimental violation of a bell's inequality in time with weak measurement," *Nature Physics*, vol. 6, no. 6, pp. 442–447, 2010.

[31] S. O. Valenzuela, W. D. Oliver, D. M. Berns, K. K. Berggren, L. S. Levitov, and T. P. Orlando, "Microwave-induced cooling of a superconducting qubit," *Science*, vol. 314, no. 5805, pp. 1589–1592, 2006.

[32] L. DiCarlo, J. M. Chow, J. M. Gambetta, L. S. Bishop, B. R. Johnson, D. I. Schuster, J. Majer, A. Blais, L. Frunzio, S. M. Girvin, and R. J. Schoelkopf, "Demonstration of two-qubit algorithms with a superconducting quantum processor," *Nature*, vol. 460, no. 7252, pp. 240–244, 2009.

[33] R. W. Simmonds, K. M. Lang, D. A. Hite, S. Nam, D. P. Pappas, and J. M. Martinis, "Decoherence in josephson phase qubits from junction resonators," *Physical Review Letters*, vol. 93, no. 7, p. 077003, Aug. 2004.

[34] J. Lisenfeld, C. Muller, J. H. Cole, P. Bushev, A. Lukashenko, A. Shnirman, and A. V. Ustinov, "Rabi spectroscopy of a qubit-fluctuator system," *Physical Review B*, vol. 81, no. 10, p. 100511, Mar. 2010.

[35] J. M. Martinis, K. B. Cooper, R. McDermott, M. Steffen, M. Ansmann, K. D. Osborn, K. Cicak, S. Oh, D. P. Pappas, R. W. Simmonds, and C. C. Yu, "Decoherence in josephson qubits from dielectric loss," *Physical Review Letters*, vol. 95, no. 21, 2005.

[36] V. E. Manucharyan, J. Koch, L. I. Glazman, and M. H. Devoret, "Fluxonium: Single cooper-pair circuit free of charge offsets," *Science*, vol. 326, no. 5949, pp. 113–116, Oct. 2009.

[37] L. B. Ioffe and M. V. Feigel'man, "Possible realization of an ideal quantum computer in josephson junction array," *Physical Review B*, vol. 66, no. 22, p. 224503, Dec. 2002.

[38] B. Douçot, M. V. Feigel'man, L. B. Ioffe, and A. S. Ioselevich, "Protected qubits and chern-simons theories in josephson junction arrays," *Physical Review B*, vol. 71, no. 2, p. 024505, Jan. 2005.

[39] B. Douçot and L. B. Ioffe, "Implementation of decoherence-protected logical qubits in medium-size josephson-junction arrays." *Advances In Theoretical Physics*, vol. 1134, pp. 128–139, 2009.

[40] S. Gladchenko, D. Olaya, E. Dupont-Ferrier, B. Douçot, L. B. Ioffe, and M. E. Gershenson, "Superconducting nanocircuits for topologically protected qubits," *Nature Physics*, vol. 5, no. 1, pp. 48–53, Jan. 2009.

[41] L. J. Geerligs, V. F. Anderegg, J. Romijn, and J. E. Mooij, "Single cooper-pair tunneling in small-capacitance junctions," *Physical Review Letters*, vol. 65, no. 3, pp. 377–380, Jul. 1990.

[42] M. H. Devoret, D. Esteve, and C. Urbina, "Single-electron transfer in metallic nanostructures," *Nature*, vol. 360, no. 6404, pp. 547–553, Dec. 1992.

[43] P. Lafarge, P. Joyez, D. Esteve, C. Urbina, and M. H. Devoret, "2-electron quantization of the charge on a superconductor," *Nature*, vol. 365, no. 6445, pp. 422–424, Sep. 1993.

[44] M. W. Keller, J. M. Martinis, N. M. Zimmerman, and A. H. Steinbach, "Accuracy of electron counting using a 7-junction electron pump," *Applied Physics Letters*, vol. 69, pp. 1804–1806, 1996.

[45] J. Bylander, T. Duty, and P. Delsing, "Current measurement by real-time counting of single electrons," *Nature*, vol. 434, no. 7031, pp. 361–364, 2005.

[46] J. R. Pekola, J. J. Vartiainen, M. Mottonen, O. P. Saira, M. Meschke, and D. V. Averin, "Hybrid single-electron transistor as a source of quantized electric current," *Nature Physics*, vol. 4, no. 2, pp. 120–124, Feb. 2008.

[47] V. F. Maisi, Y. A. Pashkin, S. Kafanov, J. S. Tsai, and J. P. Pekola, "Parallel pumping of electrons," *New Journal of Physics*, vol. 11, p. 113057, Nov. 2009.

[48] L. S. Kuzmin and D. B. Haviland, "Observation of the bloch oscillations in an ultrasmall josephson junction," *Physical Review Letters*, vol. 67, no. 20, pp. 2890–2893, Nov. 1991.

[49] K. Andersson, "Coulomb blockade of cooper pair tunneling in one dimensional josephson junction arrays," Ph.D. dissertation, Royal Institute of Technology (KTH), Stockholm, 2002.

[50] J. E. Mooij and Y. V. Nazarov, "Superconducting nanowires as quantum phase-slip junctions," *Nature Physics*, vol. 2, no. 3, pp. 169–172, Mar. 2006.

[51] W. Guichard and F. W. J. Hekking, "Phase-charge duality in josephson junction circuits: Role of inertia and effect of microwave irradiation," *Physical Review B*, vol. 81, no. 6, p. 064508, Feb. 2010.

[52] K. A. Matveev, A. I. Larkin, and L. I. Glazman, "Persistent current in superconducting nanorings," *Physical Review Letters*, vol. 89, no. 9, 2002.

[53] Y. Aharonov and A. Casher, "Topological quantum effects for neutral particles," *Physical Review Letters*, vol. 53, no. 4, pp. 319–321, 1984.

[54] J. R. Friedman and D. V. Averin, "Aharonov-casher-effect suppression of macroscopic tunneling of magnetic flux," *Physical Review Letters*, vol. 88, no. 5, p. 050403, Feb. 2002.

[55] G. J. Dolan, "Offset masks for lift-off photoprocessing," *Applied Physics Letters*, vol. 31, no. 5, pp. 337–339, 1977.

[56] C. C. Chi and J. Clarke, "Enhancement of the energy gap in superconducting aluminum by tunneling extraction of quasiparticles," *Phys. Rev. B*, vol. 20, no. 11, pp. 4465–, Dec. 1979.

[57] J. Aumentado, M. W. Keller, J. M. Martinis, and M. H. Devoret, "Nonequilibrium quasiparticles and 2e periodicity in single-cooper-pair transistors," *Physical Review Letters*, vol. 92, no. 6, p. 066802, Feb. 2004.

[58] "Pôle électronique. Institut Néel Grenoble."

[59] "Plateforme *Nanofab*. CNRS Grenoble."

[60] P. J. Koppinen, L. M. Vaisto, and I. J. Maasilta, "Complete stabilization and improvement of the characteristics of tunnel junctions by thermal annealing," *Applied Physics Letters*, vol. 90, no. 5, p. 053503, Jan. 2007.

[61] J. R. Nesbitt and A. F. Hebard, "Time-dependent glassy behavior of interface states in al-alox-al tunnel junctions," *Physical Review B*, vol. 75, no. 19, p. 195441, May 2007.

[62] T. H. S. Shiota, T. Imamura, "Fabrication of high quality nb/alox-al/nb josephson junctions. iii. annealing stability of alox tunneling barriers," *IEEE Transactions on Applied Superconductivity*, vol. 2, pp. 222–227, 1992.

[63] J. V. Gates, M. A. Washington, and M. Gurvitch, "Critical current uniformity and stability of nb/al-oxide-nb josephson-junctions," *Journal of Applied Physics*, vol. 55, no. 5, pp. 1419–1421, 1984.

[64] J. K. Julin, P. J. Koppinen, and I. J. Maasiltaa, "Reduction of low-frequency 1/f noise in al-alox-al tunnel junctions by thermal annealing," *Applied Physics Letters*, vol. 97, no. 15, p. 152501, Oct. 2010.

[65] B. Rodmacq, A. Manchon, C. Ducruet, S. Auffret, and B. Dieny, "Influence of thermal annealing on the perpendicular magnetic anisotropy of pt/co/alox trilayers," *Phys. Rev. B*, vol. 79, no. 2, pp. 024 423–, Jan. 2009.

[66] M. Gurvitch, M. A. Washington, and H. A. Huggins, "High-quality refractory josephson tunnel-junctions utilizing thin aluminum layers," *Applied Physics Letters*, vol. 42, no. 5, pp. 472–474, 1983.

[67] M. Tinkham, *Introduction to Superconductivity*. Dover Publications, 2004.

[68] V. Ambegaokar and A. Baratoff, "Tunneling between superconductors," *Physical Review Letters*, vol. 10, no. 11, p. 486, 1963.

[69] W. C. Stewart, "Current-voltage characteristics of josephson junctions," *Applied Physics Letters*, vol. 12, no. 8, pp. 277–&, 1968.

[70] D. E. Mccumber, "Effect of ac impedance on dc voltage-current characteristics of superconductor weak-link junctions," *Journal of Applied Physics*, vol. 39, no. 7, pp. 3113–&, 1968.

[71] A. Fay, "Couplage variable entre un qubit de charge et un qubit de phase," Ph.D. dissertation, Universite Joseph Fourier, 2008.

[72] S. Saito, M. Thorwart, H. Tanaka, M. Ueda, H. Nakano, K. Semba, and H. Takayanagi, "Multiphoton transitions in a macroscopic quantum two-state system," *Physical Review Letters*, vol. 93, no. 3, p. 037001, Jul. 2004.

[73] M. L. Della Rocca, M. Chauvin, B. Huard, H. Pothier, D. Esteve, and C. Urbina, "Measurement of the current-phase relation of superconducting atomic contacts," *Physical Review Letters*, vol. 99, no. 12, p. 127005, Sep. 2007.

[74] J. Tobiska and Y. V. Nazarov, "Josephson junctions as threshold detectors for full counting statistics," *Physical Review Letters*, vol. 93, no. 10, p. 106801, Sep. 2004.

[75] J. P. Pekola, "Josephson junction as a detector of poissonian charge injection," *Physical Review Letters*, vol. 93, no. 20, p. 206601, Nov. 2004.

[76] H. Grabert, "Theory of a josephson junction detector of non-gaussian noise," *Physical Review B*, vol. 77, no. 20, p. 205315, May 2008.

[77] H. A. Kramers, "Brownian motion in a field of force and the diffusion model of chemical reactions," *Physica*, vol. 7, pp. 284–304, 1940.

[78] T. A. Fulton and Dunklebe.ln, "Lifetime of zero-voltage state in josephson tunnel-junctions," *Physical Review B*, vol. 9, no. 11, pp. 4760–4768, 1974.

[79] M. Buttiker, E. P. Harris, and R. Landauer, "Thermal-activation in extremely underdamped josephson-junction circuits," *Physical Review B*, vol. 28, no. 3, pp. 1268–1275, 1983.

[80] A. O. Caldeira and A. J. Leggett, "Quantum tunnelling in a dissipative system," *Annals of Physics*, vol. 149, no. 2, pp. 374–456, 1983.

[81] F. Balestro, J. Claudon, J. P. Pekola, and O. Buisson, "Evidence of two-dimensional macroscopic quantum tunneling of a current-biased dc squid," *Physical Review Letters*, vol. 91, no. 15, p. 158301, Oct. 2003.

[82] N. Didier, "L'effet josephson dans les supraconducteurs et les gaz quantiques," Ph.D. dissertation, Universite Joseph Fourier, Grenoble, 2009.

[83] S. Coleman, *The Whys of Subnuclear Physics.* Plenum, 1977, pp. 805–905.

[84] R. Fazio and H. van der Zant, "Quantum phase transitions and vortex dynamics in superconducting networks," *Physics Reports-review Section of Physics Letters*, vol. 355, no. 4, pp. 235–334, Dec. 2001.

[85] B. Douçot and J. Vidal, "Pairing of cooper pairs in a fully frustrated josephson-junction chain," *Physical Review Letters*, vol. 88, no. 22, p. 227005, Jun. 2002.

[86] J. Vidal, R. Mosseri, and B. Douçot, "Aharonov-bohm cages in two-dimensional structures," *Physical Review Letters*, vol. 81, no. 26, pp. 5888–5891, Dec. 1998.

[87] C. C. Abilio, P. Butaud, T. Fournier, B. Pannetier, J. Vidal, S. Tedesco, and B. Dalzotto, "Magnetic field induced localization in a two-dimensional superconducting wire network," *Physical Review Letters*, vol. 83, no. 24, pp. 5102–5105, Dec. 1999.

[88] C. Naud, G. Faini, and D. Mailly, "Aharonov-bohm cages in 2d normal metal networks," *Physical Review Letters*, vol. 86, no. 22, pp. 5104–5107, May 2001.

[89] I. V. Protopopov and M. V. Feigel'man, "Anomalous periodicity of supercurrent in long frustrated josephson-junction rhombi chains," *Physical Review B*, vol. 70, no. 18, p. 184519, Nov. 2004.

[90] I. V. Protopopov and M. V. Feigelman, "Coherent transport in josephson-junction rhombi chain with quenched disorder," *Phys. Rev. B*, vol. 74, no. 6, pp. 064 516–, Aug. 2006.

[91] I. M. Pop, K. Hasselbach, O. Buisson, W. Guichard, B. Pannetier, and I. Protopopov, "Measurement of the current-phase relation in josephson junction rhombi chains," *Physical Review B*, vol. 78, no. 10, 2008.

[92] A. Potts, P. R. Routley, G. J. Parker, J. J. Baumberg, and P. A. J. de Groot, "Novel fabrication methods for submicrometer josephson junction qubits," *Journal of Materials Science-materials In Electronics*, vol. 12, no. 4-6, pp. 289–293, Jun. 2001.

[93] J. M. Kivioja, T. E. Nieminen, J. Claudon, O. Buisson, F. W. J. Hekking, and J. P. Pekola, "Observation of transition from escape dynamics to underdamped phase diffusion in a josephson junction," *Physical Review Letters*, vol. 94, no. 24, 2005.

[94] R. M. Bradley and S. Doniach, "Quantum fluctuations in chains of josephson-junctions," *Physical Review B*, vol. 30, no. 3, pp. 1138–1149, 1984.

[95] L. I. Glazman and A. I. Larkin, "New quantum phase in a one-dimensional josephson array," *Physical Review Letters*, vol. 79, no. 19, pp. 3736–3739, Nov. 1997.

[96] A. M. Finkelstein, "Suppression of superconductivity in homogeneously disordered-systems," *Physica B*, vol. 197, no. 1-4, pp. 636–648, Mar. 1994.

[97] D. B. Haviland, Y. Liu, and A. M. Goldman, "Onset of superconductivity in the two-dimensional limit," *Physical Review Letters*, vol. 62, no. 18, pp. 2180–2183, May 1989.

[98] B. G. ORR, H. M. JAEGER, A. M. GOLDMAN, and C. G. KUPER, "Global phase coherence in two-dimensional antigranulocytes superconductors," *Physical Review Letters*, vol. 56, no. 4, pp. 378–381, Jan. 1986.

[99] K. Andersson and D. B. Haviland, "Escape from a zero-current state in a one-dimensional array of josephson junctions," *Physical Review B*, vol. 67, no. 9, p. 092507, Mar. 2003.

[100] B. Abeles, "Effect of charging energy on superconductivity in granular metal-films," *Physical Review B*, vol. 15, no. 5, pp. 2828–2829, 1977.

[101] E. Chow, P. Delsing, and D. B. Haviland, "Length-scale dependence of the superconductor-to-insulator quantum phase transition in one dimension," *Physical Review Letters*, vol. 81, no. 1, pp. 204–207, Jul. 1998.

[102] Y. Takahide, H. Miyazaki, and Y. Ootuka, "Superconductor-insulator crossover in josephson junction arrays due to reduction from two to one dimension," *Physical Review B*, vol. 73, no. 22, p. 224503, Jun. 2006.

[103] M. Hisao, "Quantum fluctuations and dissipative phase transition in josephson chains," Master's thesis, Univ. Tsukuba, 2002.

[104] S. Corlevi, W. Guichard, F. W. J. Hekking, and D. B. Haviland, "Phase-charge duality of a josephson junction in a fluctuating electromagnetic environment," *Physical Review Letters*, vol. 97, no. 9, p. 096802, Sep. 2006.

[105] J. Koch, V. Manucharyan, M. H. Devoret, and L. I. Glazman, "Charging effects in the inductively shunted josephson junction," *Physical Review Letters*, vol. 103, no. 21, p. 217004, Nov. 2009.

[106] M. A. Castellanos-Beltran, K. D. Irwin, G. C. Hilton, L. R. Vale, and K. W. Lehnert, "Amplification and squeezing of quantum noise with a tunable josephson metamaterial," *Nature Physics*, vol. 4, no. 12, pp. 928–931, Dec. 2008.

[107] M. A. Castellanos-Beltrana and K. W. Lehnert, "Widely tunable parametric amplifier based on a superconducting quantum interference device array resonator," *Applied Physics Letters*, vol. 91, no. 8, p. 083509, Aug. 2007.

[108] I. M. Pop, I. Protopopov, F. Lecocq, Z. Peng, B. Pannetier, O. Buisson, and W. Guichard, "Measurement of the effect of quantum phase slips in a josephson junction chain," *Nature Physics*, vol. 6, no. 8, pp. 589–592, 2010.

[109] M. H. Devoret, *Quantum Fluctutations in Electrical Circuits, Ch. 10.* Les Houches Session LXIII, Elsevier, 1995.

[110] K. K. Likharev and A. B. Zorin, "Theory of the bloch-wave oscillations in small josephson-junctions," *Journal of Low Temperature Physics*, vol. 59, no. 3-4, pp. 347–382, 1985.

[111] D. V. Averin, A. B. Zorin, and K. K. Likharev, "Bloch oscillations in small-size josephson-junctions," *Zhurnal Eksperimentalnoi I Teoreticheskoi Fiziki*, vol. 88, no. 2, pp. 692–703, 1985.

[112] Y. Aharonov and D. Bohm, "Significance of electromagnetic potentials in the quantum theory," *Physical Review*, vol. 115, no. 3, pp. 485–491, 1959.

[113] R. A. Webb, S. Washburn, C. P. Umbach, and R. B. Laibowitz, "Observation of h/e aharonov-bohm oscillations in normal-metal rings," *Physical Review Letters*, vol. 54, no. 25, pp. 2696–2699, 1985.

[114] A. Cimmino, G. I. Opat, A. G. Klein, H. Kaiser, S. A. Werner, M. Arif, and R. Clothier, "Observation of the topological aharonov-casher phase-shift by neutron interferometry," *Physical Review Letters*, vol. 63, no. 4, pp. 380–383, Jul. 1989.

[115] K. Sangster, E. A. Hinds, S. M. Barnett, and E. Riis, "Measurement of the aharonov-casher phase in an atomic system," *Physical Review Letters*, vol. 71, no. 22, pp. 3641–3644, Nov. 1993.

[116] M. Konig, A. Tschetschetkin, E. M. Hankiewicz, J. Sinova, V. Hock, V. Daumer, M. Schafer, C. R. Becker, H. Buhmann, and L. W. Molenkamp, "Direct observation of the aharonov-casher phase," *Physical Review Letters*, vol. 96, no. 7, p. 076804, Feb. 2006.

[117] W. J. Elion, J. J. Wachters, L. L. Sohn, and J. E. Mooij, "Observation of the aharonov-casher effect for vortices in josephson-junction arrays," *Physical Review Letters*, vol. 71, no. 14, pp. 2311–2314, Oct. 1993.

[118] D. A. Ivanov, L. B. Ioffe, V. B. Geshkenbein, and G. Blatter, "Interference effects in isolated josephson junction arrays with geometric symmetries," *Physical Review B*, vol. 65, no. 2, p. 024509, Jan. 2002.

[119] D. B. Haviland, K. Andersson, and P. Agren, "Superconducting and insulating behavior in one-dimensional josephson junction arrays," *Journal of Low Temperature Physics*, vol. 118, no. 5-6, pp. 733–749, Mar. 2000.

[120] M. T. Tuominen, J. M. Hergenrother, T. S. Tighe, and M. Tinkham, "Experimental-evidence for parity-based 2e periodicity in a superconducting

single-electron tunneling transistor," *Physical Review Letters*, vol. 69, no. 13, pp. 1997–2000, Sep. 1992.

[121] K. K. Likharev and A. B. Zorin, "Simultaneous bloch and josephson oscillations, and resistance quantizations in small superconducting double junctions," *Japanese Journal of Applied Physics Part 1-regular Papers Short Notes & Review Papers*, vol. 26, pp. 1407–1408, 1987.

[122] G. Rastelli and F. W. J. Hekking, "Harmonic modes in long josephson junction chains," private communications.

[123] E. Hoskinson, F. Lecocq, N. Didier, A. Fay, F. W. J. Hekking, W. Guichard, O. Buisson, R. Dolata, B. Mackrodt, and A. B. Zorin, "Quantum dynamics in a camelback potential of a dc squid," *Physical Review Letters*, vol. 102, no. 9, 2009.

[124] B. Cohen-Tannoudji, C. Diu and F. Laloe, *Quantum Mechanics.* Hermann and John Wiley & Sons. Inc., 1977.

[125] K. Pearson, "The problem of the random walk," *Nature*, vol. 72, pp. 294–294, 1905.

[126] K. C. Gupta, R. Garg, and I. J. Bahl, *Microstrip Lines and Slotlines.* ARTECH HOUSE, INC., 1979.

APPENDICES

Appendix A

Variance of the tunnel resistance for random distributed conduction channels

The electrical transport through the oxide barrier of the junction is not uniform. The current mainly passes through a few conduction channels randomly distributed on the surface of the junction. We denote by M the average number of conduction channels in the junction. In Fig. A.1 we show a schematic representation of the surface of an $Al/AlO_x/Al$ junction, with randomly distributed conduction channels, as indicated by the red dots. The tunnel resistance R of the junction is:
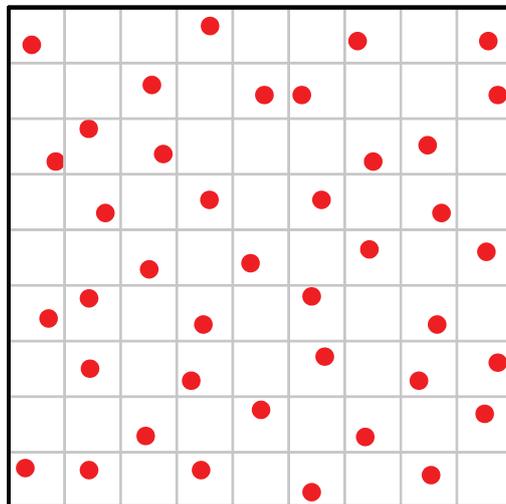

Figure A.1: Schematic representation of the surface of a tunnel junction with randomly distributed conduction channels (red dots).

$$R = \frac{1}{M \cdot c_0} \qquad \text{(A.1)}$$

Where c_0 is the average conductance of one channel. By deriving eq. (A.1) with respect to M, we find a direct link between the random variations of resistance δR

from one junction to another and the variations δM of the number of conduction channels:

$$\delta R = \frac{1}{M^2 c_0} \delta M \quad \Longrightarrow \quad \frac{\delta R}{R} = \frac{\delta M}{M} \tag{A.2}$$

In order to calculate the average value of δM, we will map our randomly distributed conduction channels model on the well known random walk problem [125]. Let us divide the surface of the junction in N identical cells, as indicated by the grid in Fig. A.1. If $N = 2 \cdot M$, we have either 1 or 0 conduction channels inside the majority of the cells. We will neglect the less probable case where 2 conduction channels occupy one cell.

We are interested in the deviation δM of the number of conduction channels from the average value M. Starting from the first cell, we count δM in the following way. At cell number k, if the cell contains a conduction channel then $\delta M_k = \delta M_{k-1} + 0.5$ and if the cell is empty then $\delta M_k = \delta M_{k-1} - 0.5$. We can easily check that if the junction contains exactly the average number of conduction channels, half of the cells will be filled and half empty, so at the end of the count, $\delta M_N = 0$. So δM_k corresponds to the total distance after the $k-th$ step of a random walk with steps equal to ± 0.5. The square of δM_k is:

$$\delta M_k^2 = \begin{cases} \delta M_{k-1}^2 + 2 \cdot \delta M_{k-1} + 0.25 & \text{for a filled cell} \\ & \text{or} \\ \delta M_{k-1}^2 - 2 \cdot \delta M_{k-1} + 0.25 & \text{for an empty cell} \end{cases} \tag{A.3}$$

From eq. (A.3) we can calculate the recursion relation for the mean squared deviation:

$$\left\langle \delta M_k^2 \right\rangle = \left\langle \delta M_{k-1}^2 \right\rangle + 0.25 \tag{A.4}$$

Thus, after N steps, we get the usual random walk scaling for the root mean square (RMS) deviation: $\sqrt{\left\langle \delta M^2 \right\rangle} = 0.5 \cdot \sqrt{N}$. Considering eq. (A.2), the resulting RMS deviation for the tunnel resistance is:

$$\frac{\sqrt{\left\langle \delta R^2 \right\rangle}}{R} = \frac{\sqrt{N}}{2} \cdot \frac{2}{N} = \frac{1}{\sqrt{N}} \tag{A.5}$$

The average number of conduction channels M is fixed by the surface S of the junction and the density of conduction channels ρ:

$$M = \rho \cdot S \tag{A.6}$$

Since $N = 2 \cdot M$, eq. (A.5) can be rewritten as a function of ρ and S:

$$\sigma^2 = \frac{1}{2\rho} \cdot \frac{1}{S} \tag{A.7}$$

where $\sigma^2 = \frac{\left\langle \delta R^2 \right\rangle}{R^2}$ is the variance of the tunnel barrier resistance.

Appendix B

Evaluating the self capacitance C_0 of an island in the junction chain

The main part of C_0 is given by the coupling of the superconducting island to the large ($100 \times 200 \mu m^2$) bonding plot, situated at a distance of $\sim 500 \mu m$ on the wafer (for example see Fig. 2.8). We approximate this coupling to be the capacitance between two parallel wires of length l and width w at a distance of $d \simeq 500 \mu m$, in the particular electromagnetic environment of the sample. The parameters l and w are the length and the width of the island. The third dimension of the island, the thickness of the metal layer, is much smaller and it is neglected in the following calculations. The value of the capacitive coupling C_0 is given by [126]:

$$C_0 = \frac{\epsilon_0 \left(\epsilon_r + 1\right)}{2} \cdot l \cdot \frac{E\left[\sqrt{1 - k^2}\right]}{E\left[k\right]} \quad \text{and} \quad k = \frac{d}{d + 2w} \tag{B.1}$$

Here ϵ_r is the relative dielectric constant of the environment and $E\left[k\right]$ is the so called *complete elliptic integral of the first kind*, which reads:

$$E\left[k\right] = \int_0^{\frac{\pi}{2}} \frac{d\theta}{\sqrt{1 - k^2 sin\theta}} \tag{B.2}$$

The typical parameters of an island in the 400 junctions chain discussed in section 5.7 are: $l = 10 \mu m$, $w = 1 \mu m$ and $\epsilon_r = 12$ (Si substrate). Using the formulas B.1 and B.2, we obtain $C_0 \simeq 200 aF$.

If we add a gate electrode in the vicinity of an island in the chain, as discussed in section 5.5, the capacitive coupling C_G will contain two contributions. The first one, C'_g is the coupling of the island to the bonding plot of the gate electrode, as explained in the previous paragraph. The second contribution, C''_g depends on the exact shape of the island and the gate. We calculate C''_g by using a commercial, high precision electromagnetic analysis software: *Sonnet*. In Fig. B.1 we present an e-beam image of the gate electrode and the corresponding circuit simulated with *Sonnet*. For the parameters of the 6 SQUID chain sample discussed in section 5.5, we obtain a total coupling to the central island $C_G^3 = C'_g + C''_g \simeq 220 \, aF + 200 \, aF = 420 \, aF$, which is very close to the measured value. The capacitance of the lateral islands, C_G^2 and C_G^4, is mainly given by the coupling to the bonding plot of

the gate electrode: $C'_{g-lat} \simeq 20\,aF$. The coupling of the lateral islands to the nearby gate electrode is screened by the ground wires.
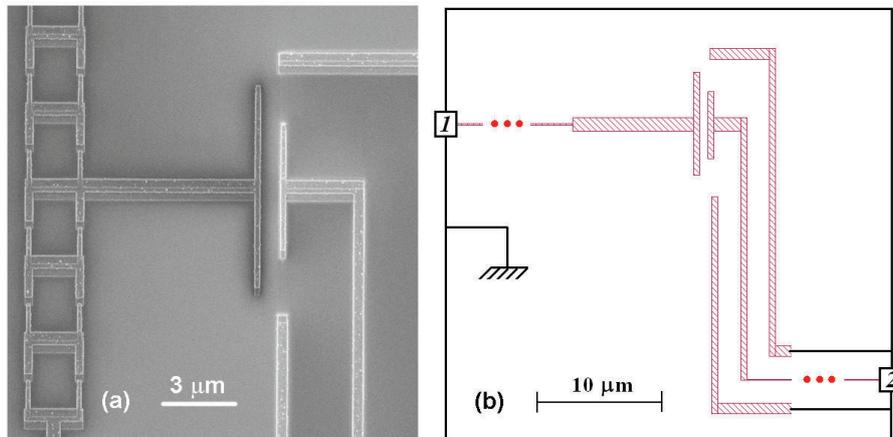

Figure B.1: SEM image of the central gate (a) and the corresponding *Sonnet* circuit (b).